Study on proton and deuteron nuclear data relevant to the development of intense accelerator-based neutron sources

竹下, 隼人

Study on proton and deuteron nuclear data relevant to the development of intense accelerator-based neutron sources

Hayato Takeshita
Department of Advanced Energy Engineering Science
Interdisciplinary Graduate School of Engineering Sciences
Kyushu University

February 2022

Abstract

Neutron applications have been increasingly used in various fields not only limited to scientific research but also in industrial and medical fields. The demand for intense neutron sources is growing steadily. Recently, spallation neutron sources and deuteron accelerator-based neutron sources have attracted attention to their application potentials in various fields. For designing such neutron sources, more accurate and reliable nuclear data are necessary. This thesis aims to measure primarily two types of nuclear data: neutron production by deuteron-induced reactions and nuclide production cross section by GeV-protons. The former data are employed to evaluate the performance of deuteron sources and shielding design in structural materials whereas the latter data are required for assessing radioactivity and shielding design in spallation neutron sources. In addition, this thesis aims to benchmark some reaction models that are used to simulate the behavior of radiation in the accelerator facilities.

The measurement of neutrons produced by deuteron-induced reactions was conducted at the Center for Accelerator and Beam Applied Science, Kyushu University. The double-differential neutron yields for six materials (LiF, C, Si, Ni, Mo, and Ta) by bombarding 6.7-MeV/u deuterons were derived using unfolding the light output distributions measured by an organic liquid scintillation detector. The benchmark analysis of Particle and Heavy Ion Transport code System (PHITS) and DEUteron-induced Reaction Analysis Code System (DEURACS) was performed by comparing the measured neutron spectra with the predicted spectra. The INCL4.6/GEM and JQMD/GEM implemented in PHITS disagreed with most of the measured data. In contrast, DEURACS successfully reproduced the experimental data for the C, Si, Ni, Mo, and Ta targets. Thus, this study concludes that DEURACS is a promising calculation tool in developing basic nuclear data necessary for designing deuteron-based neutron sources.

The nuclide production cross sections of the Mn, Co, Ni, and Zr targets were measured by the conventional activation method at Japan Proton Accelerator Research Complex (J-PARC). Cross sections of 115 reactions were measured, ten of which were measured for the first time. The stable proton beam and well-established beam profile-monitoring system of J-PARC and several precise corrections reduced the experimental uncertainties to typically 5%. The excitation functions were divided into three types depending on the product masses. The cross sections for the light products increased with increasing incident proton energy. The cross sections for the medium-heavy products have a broad maximum at approximately 1 GeV. For the heavy products, the cross section decreased with

increasing incident proton energy. The measured data were compared with predictions of spallation reaction models implemented in PHITS (INCL4.6/GEM, Bertini/GEM, and JAM/GEM), and INCL++/ABLA07 version 6.28 and nuclear data library JENDL/HE-2007. All the reaction models and nuclear data library generally reproduced the dependency of the cross sections on the incident proton energy. To investigate the prediction capabilities of the reaction models and data library, the mean square deviation factor was introduced. The JENDL/HE-2007 exhibited the best reproducibility for the Co and Ni targets and relatively good agreement for the Mn and Zr targets. However, even the JENDL/HE-2007 does not meet the requirement. Thus, further improvement of reaction models is required for the development of spallation neutron sources.

Contents

List of Figures

List of Tables

1 Introduction

1.1 Neutron Applications

The neutrons were discovered by James Chadwick in 1932 [1], [2]. After the invention of the nuclear reactor in 1942, the applications of neutrons have been extended to various fields. Nuclear reactors have not only been used as the sources of energy in developed countries but also for scientific research, industrial uses, and medical treatment, as depicted in Fig. 1.1. Similar to X-ray diffraction, neutron diffraction technique has been applied to perform structural analysis of materials. Because X-rays interact with the electron cloud surrounding the atoms, X-ray diffraction is effective for high-Z materials. On the other hand, neutron diffraction is particularly sensitive to low-Z materials, such as hydrogen and protein. In addition, using the neutron's magnetic moment ($\mu_n = -9.66 \times 10^{-27}$ J/T), neutron diffraction technique can be used for the magnetic imaging of materials.

Further, neutron-induced nuclear reactions are used in various applications. In industries, high-quality semiconductors are manufactured using the neutron transmutation doping technique [3]. In the medical field, medical isotope production [4], [5] and boron neutron capture therapy (BNCT)[6] have been proposed.

In the nuclear energy field, the disposal of high-level radioactive waste is crucial. The transmutation technique has been proposed as a solution, in which long-lived nuclides are converted into stable or short-lived nuclides through nuclear reactions. Transmutation using accelerator-based neutron sources are proposed [7] for the transmutation of fission products. In Japan, the Accelerator-Driven System (ADS) [8] has been proposed for the transmutation of minor actinides. The ADS consists of a proton accelerator and sub-critical reactor(Fig. 1.1). The proton beam is first injected into the spallation neutron target made of lead-bismuth eutectic. The spallation and fission neutrons maintain the critical state of the reactor and perform the transmutation of minor actinides that are loaded as nuclear fuel.

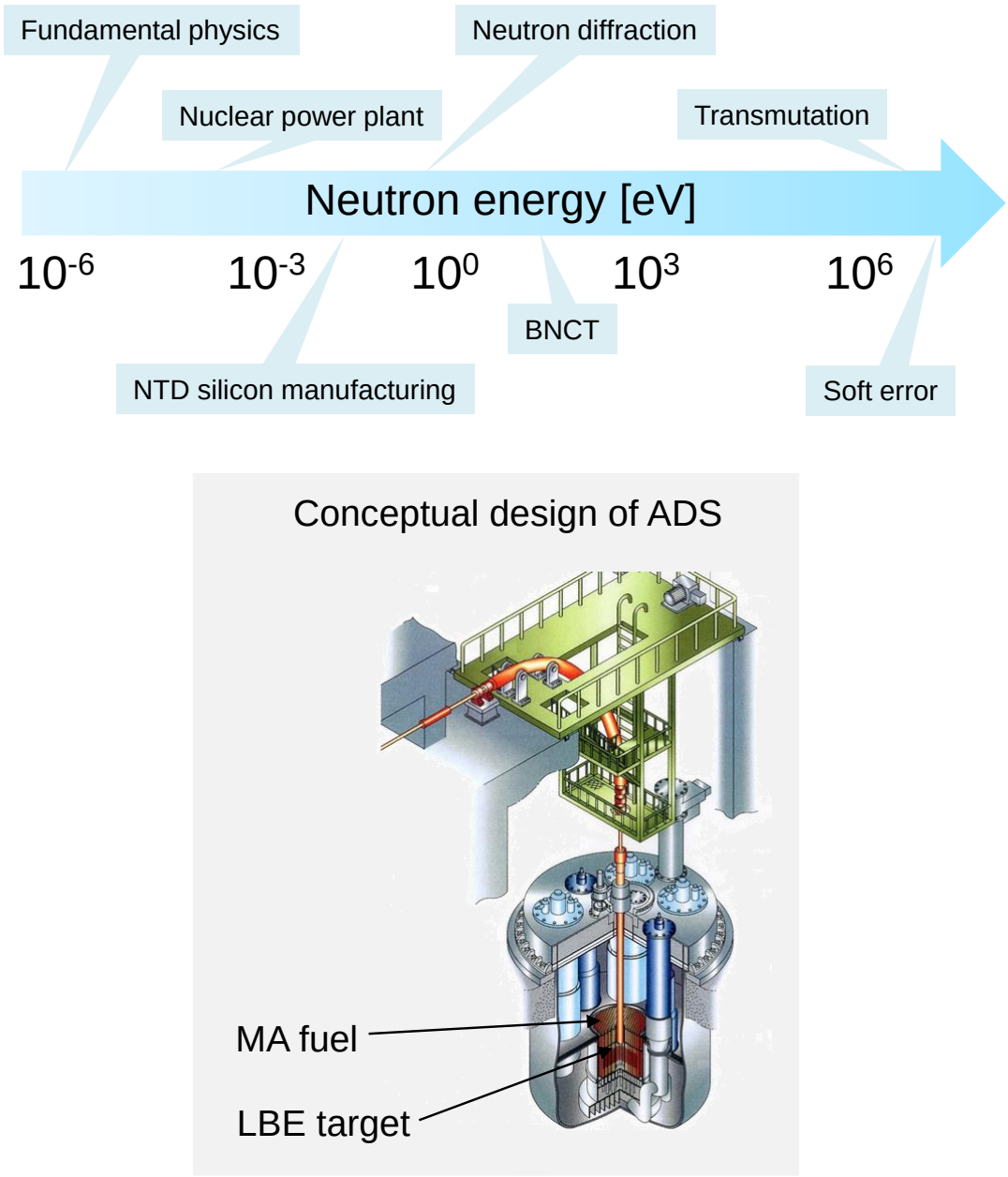

Figure 1.1: Examples of neutron applications.

1.2 Neutron Sources

A neutron is an unstable particle with a life time τ_n of approximately 15 min. Thus, neutrons cannot be stored and must be generated via nuclear reactions. As mentioned in Section 1.1, nuclear reactors have been widely used as neutron sources for a long time. The first research reactor provided a thermal neutron flux of approximately 10^7 neutrons/cm^2/s. As nuclear technology advanced and the use of neutrons in various fields increased, the neutron intensity of nuclear reactors increased and the use of nuclear reactor was expanded to many countries.

However, after the Chernobyl nuclear power plant accident in 1986, the potential dangers of nuclear reactors were recognized globally. In addition, the installation of a nuclear reactor presents disadvantages such as high construction and maintenance costs, and the inherent risks of possessing and using fuel. In Japan, the number of reactors is small, but nowadays, e.g., Japan Research Reactor-3 (JRR-3) [9] and Kyoto University Research Reactor (KUR) [10] are available for research.

In this situation, the use of accelerator-based neutron sources have increased. This thesis focuses on the following two types of accelerator-based neutron sources.

1.2.1 Proton Accelerator-based Neutron Sources

Neutrons are produced in nuclear reactions caused by bombarding high-energy protons on a target material. The incident proton beam must be accelerated up to a few MeV or GeV by accelerators. If a light element (e.g., Li) is used as a target, the neutron spectrum exhibits a sharp peak around the incident energy, as shown in Fig. 1.2. This quasi-monoenergetic neutron source is suitable when certain energy of neutrons is desired. However, neutron intensities are relatively small (approximately 10^{11}–10^{13} neutrons/s [11]). Conversely, an intense neutron beam approximately 10^{17}–10^{18} neutrons/s can be produced by spallation neutron sources where hundreds of MeV or few GeV protons bombard heavy target materials, such as Hg and W. However, the neutron spectra show no characteristic peak and the neutron energy cannot be selected (Fig. 1.2).

There are many proton accelerator-based neutron sources in the world. In particular, quasi-monoenergetic neutron source facilities are relatively compact and installed in research institutes, universities, and hospitals [12]. In contrast, limited numbers of spallation neutron sources are available all over the world, e.g., Japan Proton Accelerator Research Complex (J-PARC) in Japan, Spallation Neutron Source in the USA [13], European Spallation Source in Sweden [14], and China Spallation Neutron Source [15].

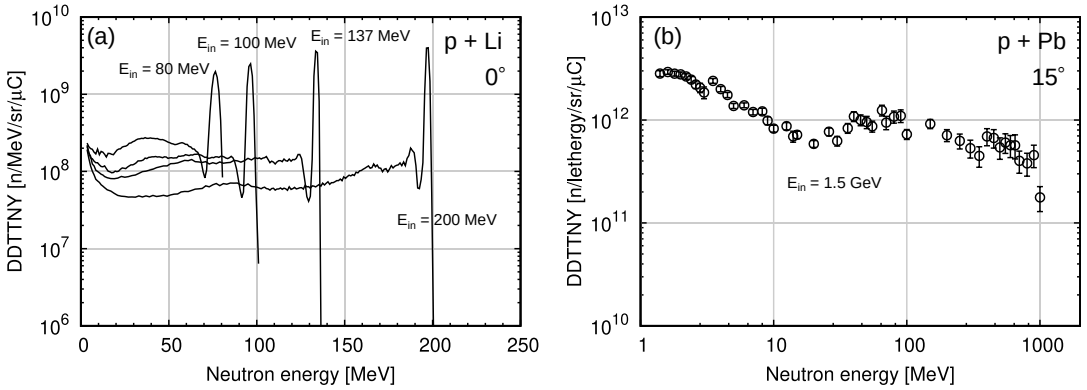

Figure 1.2: Neutron spectra of a (a) quasi-monoenergetic and (b) spallation neutron source. The experimental data are taken from Refs. [16], [17].

1.2.2 Deuteron Accelerator-based Neutron Sources

Recently, deuteron accelerator-based neutron sources have been proposed as intense neutron sources. The (d,xn) reactions on light targets, e.g., Li, Be, and C, are used to generate a neutron beam. Figure 1.3 shows the comparison of the neutron spectra generated by the (d,xn) and (p,xn) reactions for the Be target at an incident energy of 40 MeV [18], [19]. The (d,xn) reaction yields approximately 10 times more neutrons at the characteristic peak than that of the (p,xn) reaction. The (d,xn) spectra show a broad peak around half incident energy, providing the selectivity of neutron energy by adjusting the incident deuteron energy. Additionally, the neutrons are emitted with forward-peaked angular distribution. This poses as an advantage from the point of view of shielding of the facility.

Owing to these characteristics, deuteron accelerator-based neutron sources are expected to widen the application fields. The International Fusion Materials Irradiation Facility (IFMIF) [20] project was launched to simulate the intense ($\sim 10^{14}$ neutrons/cm^2/s) neutron flux generated in fusion reactors for the irradiation testing of materials. In the IFMIF, 40-MeV deuteron beams are to be used to generate approximately 14-MeV neutron beam by the Li(d,xn) reaction. In addition, deuteron accelerator-based neutron sources are under construction or will be constructed, e.g., the Neutron For Science [21] at GANIL and Beijing Isotope-Separation-On-Line neutron-rich beam facility (BISOL) [22]. Recently, medical isotope production [5] and boron neutron capture therapy (BNCT) using a deuteron accelerator have been proposed [6].

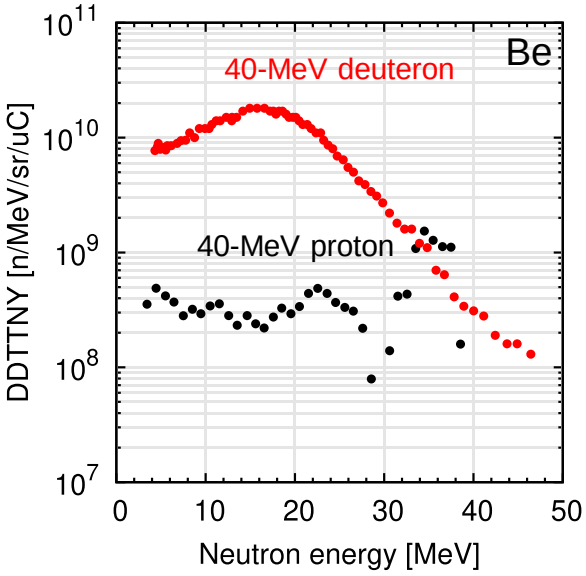

Figure 1.3: Comparison of neutron spectra at an emission angle of 0° generated by bombarding protons and deuterons on the Be target with an incident energy of 40 MeV. The data are taken from Refs. [18], [19].

1.2.3 Other Neutron Sources

The neutrons can also be produced by some other methods. Historically, neutrons, for the first time, were produced by the ^{9}Be(α,n) reaction, where the α-particle was emitted by the natural α-decay of ^{210}Po [2]. The (α,n) reactions combines with a α-decay nuclide and Be are also used as neutron sources, such as ^{242}Cm/Be and ^{241}Am/Be. However, the neutrons can be produced by spontaneous fission of transuranium nuclides. The most common nuclide is ^{252}Cf [23] with a half-life of 2.65 yr. This type of source provides a neutron spectrum with a Maxwellian distribution, i.e., $\phi(E_n) \propto \sqrt{E_n} \exp\left(-E_n/E_0\right)$, where the constant E_0 is 1.3 MeV for ^{252}Cf [23]. These neutron sources do not require an accelerator or any other artificial equipment.

1.3 Status of Nuclear Data

As mentioned in Section 1.2, there are many types of neutron sources available nowadays. The demand for intense neutron sources is expected to increase as the neutron applications expand. This work focuses on the proton and deuteron

accelerator-based neutron sources, particularly, the spallation neutron sources and deuteron neutron sources, which are expected to be used in various applications as the next-generation neutron sources.

The development of accelerator-based neutron sources requires comprehensive understanding of nuclear reactions for determining the specifications, shielding design, etc. In the accelerator facilities' design, particle transport codes, such as Particle and Heavy Ion Transport code System (PHITS) [24] and Geant4 [25], are employed. These codes use nuclear reaction models and/or nuclear data libraries to calculate the amount of radiations and radioactive nuclides generated in nuclear reactions. To improve the accuracy of the simulations, the nuclear data involving the neutron fluxes from target materials and nuclide production cross sections plays a key role. The present status of the nuclear data is outlined below.

1.3.1 Data of Deuteron-Induced Reaction

Design of deuteron accelerator-based neutron sources requires the data of neutrons yielding from not only the target materials (e.g., Li, Be and C) but also from structural materials (e.g. Fe and stainless steel). The list of nuclear data library containing the deuteron-induced reaction is given in Table 1.1. TENDL [26] is the general-purpose library that compiles the calculations based on the TALYS [27] code. It covers incident energies up to 200 MeV and the target nuclides with a life time longer than 1 s. However, as shown in Fig. 1.4, TALYS cannot treat deuteron breakup correctly, and underestimates neutron spectra. The ENDF/B [28] is a nuclear data library provided by the International Atomic Energy Agency (IAEA). It is available only for deuteron energies up to 5 MeV and the five target nuclides (^{2}H, ^{3}H, ^{3}He, ^{6}Li, and ^{7}Li).

Nakayama et al. developed a calculation code system dedicated to the deuteron reactions, called DEUteron-induced Reaction Analysis Code System (DEURACS) [29]. The DEURACS successfully reproduces both the measured double-differential cross sections (DDXs) for various target elements [30], [31] and double-differential thick target neutron yields (DDTTNYs) for Be and C [29]. In 2021, the library JENDL/DEU-2020 [32], which is based on a calculation by DEURACS, was published. JENDL/DEU-2020 implements the data for target nuclides that are potential candidates of neutron converter used in deuteron accelerator-based neutron sources, i.e., ^{6}Li, ^{7}Li, ^{9}Be, ^{12}C, and ^{13}C. However, validation of DEURACS for heavy elements at low-incident energies has not been sufficiently performed.

Table 1.1: Nuclear data libraries containing deuteron reactions.

Library	Deuteron energy [MeV]	Target nuclides
TENDL2019	0–200	Nuclides with $\tau \geq 1$ s
ENDF/B-VIII.0	0–5	^{2}H, ^{3}H, ^{3}He, ^{6}Li, ^{7}Li
JENDL/DEU-2020	0–200	^{6}Li, ^{7}Li, ^{9}Be, ^{12}C, ^{13}C

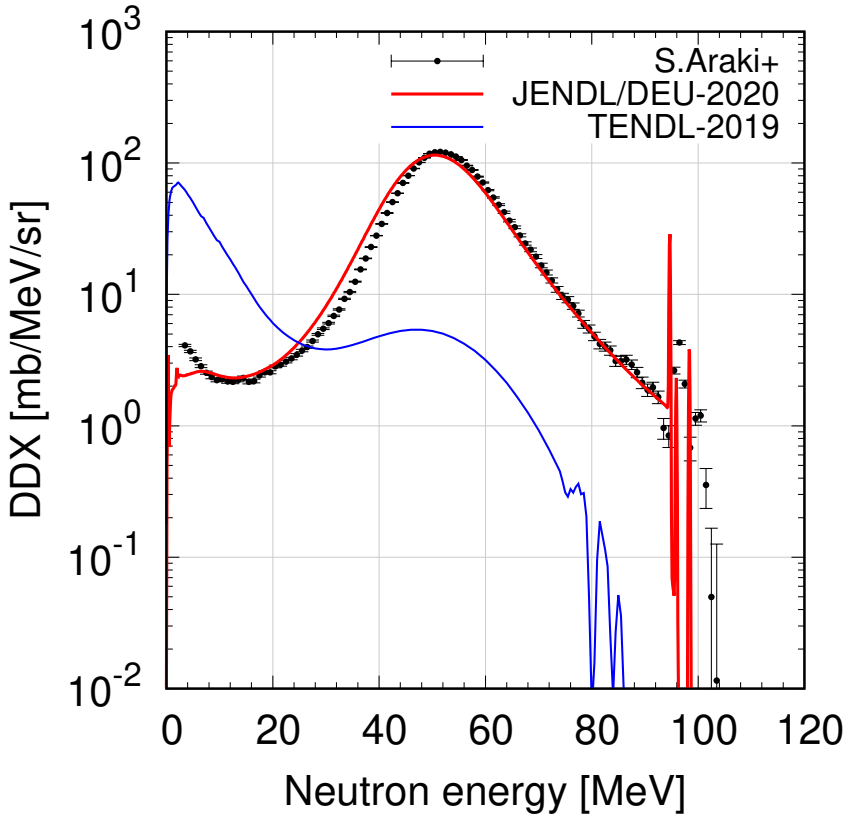

Figure 1.4: Experimental and evaluated double-differential cross sections of the ^{12}C(d,xn) reaction. The experimental data are taken from Ref. [30], and evaluated data are taken from TENDL-2019 [26]. Note that the incident deuteron energy for the experimental data is 102 MeV and evaluated data is 100 MeV.

1.3.2 Nuclide Production Cross Section Data for Spallation Reactions

As for the spallation neutron sources, the DDTTNYs induced by GeV protons from heavy elements are reproduced by spallation reaction models, e.g., INCL model [33] relatively well. However, data on nuclide production cross section,

which is necessary to evaluate the beam loss and the amount of activation of the spallation target itself, are still insufficient.

There are many nuclear data libraries containing nuclide production cross section by high-energy proton-induced reactions, e.g., TENDL-2019, ENDF/B-VIII.0, JENDL-4.0/HE [34], and JENDL/HE-2007 [35]. Most of them cover incident energy up to 200 MeV or less whereas the JENDL/HE-2007 covers up to 3 GeV, which is desired for the development of spallation neutron sources.

In previous studies, nuclide cross sections in the GeV region were systematically measured. In some of these works, a benchmark of spallation reaction models was set. However, the existing models could not reproduce the experimental data with sufficient accuracy, suggesting the necessity of improving the nuclear reaction models. To improve the nuclear reaction model, further experimental data are required.

Towards this, Iwamoto suggested an innovative approach to generate nuclear data based on the Gaussian process regression [36]. This method generates nuclear data using existing experimental data, and the generated data and their uncertainties strongly depend on the accuracy of the experimental data. Therefore, the expansion of accurate experimental data by such a method is needed in nuclear data evaluation.

1.4 Objective

In the development of next-generation intense neutron sources, nuclear data play a fundamental role. To ensure the data reliability and to contribute to the improvement of nuclear reaction models, the objectives of this thesis are as follows:

- To measure DDTTNYs with 6.7 MeV/u deuterons for six target elements (LiF, C, Si, Ni, Mo, and Ta), and to compare them with the 6.7-MeV/u triton data and some theoretical calculations

- To measure the nuclide production cross sections for four target elements (Mn, Co, Ni, and Zr), and to validate spallation reaction models and nuclear data library.

Neutron production data using low-energy deuteron-induced reactions are still scarce particularly for the heavy targets and benchmarking of reaction models has not been performed sufficiently. Thus, such benchmarks are rather important for the development of deuteron accelerator-based neutron sources. The nuclide production cross sections of spallation reactions are required for the assessment

of radioactivity generated in the spallation neutron source. In this work, several efforts were devoted to obtain the accurate cross section data.

This thesis consists of four chapters. In Chapter 2, the experimental procedure and experimental results of the deuteron-induced DDTTNYs are detailed, and validation of the theoretical calculations is performed. In Chapter 3, measurements of nuclide production cross sections are described. Finally, the summary and conclusions are presented in Chapter 4.

2 Thick Target Neutron Yields from LiF, C, Si, Ni, Mo, and Ta Bombarded by 6.7-MeV/u Deuterons

2.1 Introduction

The application of deuteron-based neutrons is expected to be extended in various application fields, as mentioned in Chapter 1. Thus far, the DDXs and DDTTNYs were systematically measured at Kyushu University, as listed in Tables 2.1 and 2.2. Theoretical analyses were performed using calculation codes such as PHITS, TALYS [27], and DEURACS. DEURACS successfully reproduced the experimental data of DDX for a wide range of target atomic number. For the DDTTNY data, however, the validation of DEURACS was performed only for the C target at an incident energy of 4.5 MeV/u, and no validation has been reported for heavy targets, i.e., Cu ($Z = 29$), Nb ($Z = 41$), and Ta ($Z = 73$). These elements are also of interest to validate the shielding design of neutron sources as well as understanding the reaction mechanisms.

On the other hand, Drosg et al. have recently tackled neutron production with triton irradiation, and measured the DDTTNYs for various target materials (H_2O, D_2O, LiF, Si, Ni, Mo, Ta, W, Pt, and Au) using 6.7 MeV/u triton beams [37]. A triton has one more neutron than a deuteron, so tritons are expected to generate more neutrons than deuterons; however, no comparison of DDTTNYs from deuteron and triton incidences has been reported since DDTTNY data of triton incidence is only available because the triton beam production and handling is difficult by its radioactivity. Additionally, theoretical calculations for the (t,xn) spectra are not reported in Ref. [29]. Comparing the (t,xn) and (d,xn) data might offer a better understanding of the nuclear reaction mechanism.

This chapter aims to measure DDTTNYs with 6.7 MeV/u deuterons for LiF, C, Si, Ni, Mo, and Ta targets, then compare the measured data with the previous (t,xn) spectra at the same incident energy per nucleon, and discuss the difference in spectral characteristics and reaction mechanisms. Further, this study aims to validate prediction capabilities of some calculation codes, including DEURACS

Table 2.1: Data of double-differential cross sections of the (d,xn) reactions previously measured at Kyushu University [30], [31].

Incident energy	Target	Measured angle
51 MeV/u	Li	0°, 10°
	Be	0°, 5°, 10°, 15°, 20°, 25°
	C	0°, 5°, 10°, 15°, 20°, 25°
	Al	0°, 5°, 10°, 15°, 20°, 25°
	Cu	0°, 10°
	Nb	0°, 10°
100 MeV/u	Li	0°, 5°, 10°, 15°, 20°, 25°
	Be	0°, 5°, 10°, 15°, 20°, 25°
	C	0°, 5°, 10°, 15°, 20°, 25°
	Al	0°, 5°, 10°, 15°, 20°, 25°
	Cu	0°, 5°, 10°, 15°, 20°, 25°
	Nb	0°, 5°, 10°, 15°, 20°, 25°
	In	0°, 5°, 10°, 15°, 20°, 25°
	Ta	0°, 5°, 10°, 15°, 20°, 25°
	Au	0°, 5°, 10°, 15°, 20°, 25°

Table 2.2: Data of double-differential thick target neutron yields of the (d,xn) reactions previously measured at Kyushu University [38]–[41].

Incident energy	Target	Measured angle
2.5 MeV/u	C	0°, 30°, 60°, 90°, 120°, 140°
	Al	0°, 15°, 30°, 45°, 60°, 75°, 90°, 120°, 140°
	Ti	0°, 15°, 30°, 45°, 60°, 75°, 90°, 120°, 140°
	Cu	0°, 15°, 30°, 45°, 60°, 75°, 90°, 120°, 140°
	Nb	0°, 15°, 30°, 45°, 60°, 75°, 90°, 120°, 140°
4.5 MeV/u	C	0°, 15°, 30°, 45°, 60°, 75°, 90°, 120°, 140°
	Al	0°, 15°, 30°, 45°, 60°, 75°, 90°, 120°, 140°
	Ti	0°, 15°, 30°, 45°, 60°, 75°, 90°, 120°, 140°
	Cu	0°, 15°, 30°, 45°, 60°, 75°, 90°, 120°, 140°
	Nb	0°, 15°, 30°, 45°, 60°, 75°, 90°, 120°, 140°
	Ta	0°, 15°, 30°, 60°, 90°, 120°

for the DDTTNYs over a wide range of atomic numbers, and to benchmark some calculation codes for triton-induced reactions.

2.2 Deuteron-induced Reaction Processes

The deuteron is a weakly bound system consisting of a proton and a neutron with a biding energy of 2.225 MeV. Owing to its weak binding energy, a deuteron can be easily separated into a proton and a neutron when bombarding a nucleus. This process is called deuteron breakup. Deuteron-induced reactions can be divided into following reaction processes including the breakup process, as shown in Fig. 2.1:

- Elastic breakup (EBU)
  The deuteron is separated into a proton and a neutron by the interaction with the target nuclei. Each nucleon is emitted in forward directions with kinematic energy with a peak approximately half the incident deuteron energy without excitation of the residual nuclei.

- Non-elastic breakup (NBU)
  One nucleon of the incident deuteron interacts strongly and combines with the target nuclei in the continuum or discrete states whereas the other proceeds with its original direction. Since the emitted particle does not interact with the target nuclei, its energy distribution also has a peak around half incident deuteron energy. When the residual nucleus transfers into a discrete state, the other nucleon is also emitted with discrete energy.

- Pre-equilibrium process (PE)
  Pre-equilibrium process is an intermediate process between the direct and statistical decay processes. In this process, particles are emitted with relatively high kinematic energy compared with the statistical decay process. Because the equilibrium of compound nucleus has not been attained in this process the angular distribution of the emitted particles is also forward-peaked.

- Statistical decay (SD)
  After the direct and PE processes, or the deuteron absorption, an equilibrium compound nucleus is formed. In the de-excitation of the compound nucleus, some particles including neutrons and γ-rays, are emitted isotropically.

These reaction processes are calculated using different models or methods depending on the calculation codes. The details of the calculation models and methods used in this paper are given in the next section.

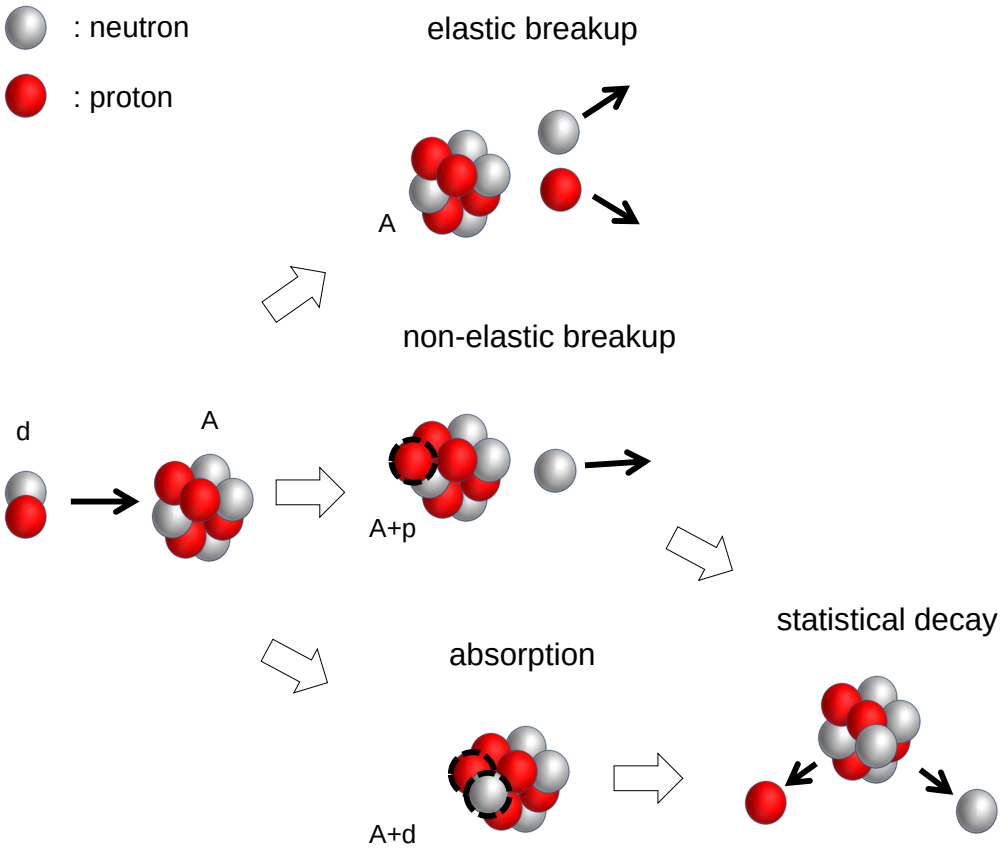

Figure 2.1: Schematic view of deuteron-induced reaction processes

2.3 Reaction Models

2.3.1 DEURACS

DEURACS is an integrated code system dedicated to deuteron-induced reactions, which was developed by Nakayama et al. [29], [42], [43]. DEURACS consists of several calculation codes based on theoretical models to describe the respective reaction processes and has been successfully applied to (d,xp), (d,xn) reactions. DEURACS describes double-differential cross section (DDX) of (d,xn) reaction by incoherent summation of three components:

$$\frac{\mathrm{d}^2\sigma(d,xn)}{\mathrm{d}E\mathrm{d}\Omega} = \frac{\mathrm{d}^2\sigma_{\mathrm{EBU}}}{\mathrm{d}E\mathrm{d}\Omega} + \frac{\mathrm{d}^2\sigma_{\mathrm{NBU}}}{\mathrm{d}E\mathrm{d}\Omega} + \frac{\mathrm{d}^2\sigma_{\mathrm{PE+SD}}}{\mathrm{d}E\mathrm{d}\Omega}, \tag{2.1}$$

where $\mathrm{d}^2\sigma_{\mathrm{EBU}}/\mathrm{d}E\mathrm{d}\Omega$, $\mathrm{d}^2\sigma_{p-\mathrm{STR}}/\mathrm{d}E\mathrm{d}\Omega$, and $\mathrm{d}^2\sigma_{\mathrm{PE+SD}}/\mathrm{d}E\mathrm{d}\Omega$ are DDXs of elastic breakup reaction, non-elastic breakup reaction, and the sum of PE and SD processes, respectively. Each component is calculated as follows:

Elastic breakup

The elastic breakup reaction is calculated with the codes based on the Continuum-Discretized Coupled-Channels method (CDCC) [44]. In CDCC calculations, a deuteron is considered as a pair of a proton (p) and a neutron (n), and scattering on a target (A) can be described by the $A+p+n$ three-body system. The infinite number of breakups is truncated and discretized to a finite number of discrete states with respect to its fragmentation and relative momentum and is introduced to the coupled-channel equations.

According to Iseri et al. [45], the triple differential cross sections of neutron emission for breakup process is expressed as

$$\frac{\mathrm{d}^3\sigma_{\mathrm{EBU}}}{\mathrm{d}\Omega_n^L\mathrm{d}\Omega_p^L\mathrm{d}E_n^L} = \frac{2\pi}{\hbar}\frac{\mu_i}{P_d}|T_{fi}|^2\rho(E_n^L), \tag{2.2}$$

where $\mathrm{d}\Omega_n^L$ and $\mathrm{d}\Omega_p^L$ are the emission directions of neutron and proton, respectively, E_n^L is the neutron emission energy, μ_i is the reduced mass of the initial state, P_d is the momentum of incident deuteron, T_{fi} is the transition matrix, and $\rho(E_n^L)$ is the three-body phase space factor [46]. T_{fi} is given in Ref [45]. The DDX for neutron emission is given by integration Eq.(2.2) over proton emission angle:

$$\frac{\mathrm{d}^2\sigma_{\mathrm{EBU}}}{\mathrm{d}\Omega_n^L\mathrm{d}E_n^L} = \int \mathrm{d}\Omega_p^L \frac{\mathrm{d}^3\sigma_{\mathrm{EBU}}}{\mathrm{d}\Omega_n^L\mathrm{d}\Omega_p^L\mathrm{d}E_n^L}. \tag{2.3}$$

Non-elastic breakup

The Glauber model [47] is used to calculate cross sections for deuteron absorption, total reaction cross section, and DDXs for proton and neutron stripping reactions to continuum state. The Glauber model is a semi-classical model including the eikonal and adiabatic approximations.

The scattering matrix S is expressed as

$$S(b_d) = \exp\left[i\chi_d(b_d)\right], \tag{2.4}$$

where

$$\chi_d(b_d) = -\frac{1}{\hbar\nu}\int_{-\infty}^{+\infty} V_d(\sqrt{b_d^2 + z^2})\mathrm{d}z. \tag{2.5}$$

Here, χ_d is the eikonal phase shift, b_d is the impact factor of incidnet deuteron, ν is the relative velocity between the incident deuteron and target nuclei, and V_d is the deuteron potential.

Pre-equilibrium process

The DDXs for PE and SD processes are calculated with Comprehensive Code for Nuclear-data Evaluation (CCONE) code [48]. In CCONE, PE process is calculated using two-component exciton model [49]. Figure 2.2 describes the evolution of the PE process of proton-induced reaction. The numbers in the diagram denote the excitation states at time t as $Q(p_\pi, h_\pi, p_\nu, h_\nu, t)$ where p_π (p_ν) are the proton (neutron) number and h_π (h_ν) are the proton (neutron) hole number. The temporal development of the system are described a master equation:

$$\begin{aligned}
&\frac{\mathrm{d}Q(p_\pi, h_\pi, p_\nu, h_\nu, t)}{\mathrm{d}t} = \\
&Q(p_\pi+1, h_\pi+1, p_\nu, h_\nu)\lambda_\pi^-(p_\pi+1, h_\pi+1, p_\nu, h_\nu) \\
&+ Q(p_\pi, h_\pi, p_\nu+1, h_\nu+1)\lambda_\nu^-(p_\pi, h_\pi, p_\nu+1, h_\nu+1) \\
&+ Q(p_\pi-1, h_\pi-1, p_\nu, h_\nu)\lambda_\pi^+(p_\pi-1, h_\pi-1, p_\nu, h_\nu) \\
&+ Q(p_\pi, h_\pi, p_\nu-1, h_\nu-1)\lambda_\nu^+(p_\pi, h_\pi, p_\nu-1, h_\nu-1) \\
&+ Q(p_\pi+1, h_\pi+1, p_\nu-1, h_\nu-1)\lambda_{\pi\nu}^0(p_\pi+1, h_\pi+1, p_\nu-1, h_\nu-1) \\
&+ Q(p_\pi-1, h_\pi-1, p_\nu+1, h_\nu+1)\lambda_{\nu\pi}^0(p_\pi-1, h_\pi-1, p_\nu+1, h_\nu+1) \\
&- Q(p_\pi, h_\pi, p_\nu, h_\nu)/\tau(p_\pi, h_\pi, p_\nu, h_\nu),
\end{aligned} \tag{2.6}$$

where λ_π^+ (λ_ν^+) it the internal transition rate for proton (neutron) particle-hole pair creation, $\lambda_{\pi\nu}^0$ ($\lambda_{\nu\pi}^0$) is the rate for the conversion of a proton (neutron) particle-hole pair into a neutron (proton) particle-hole pair, and λ_π^- (λ_ν^-) is the rate for

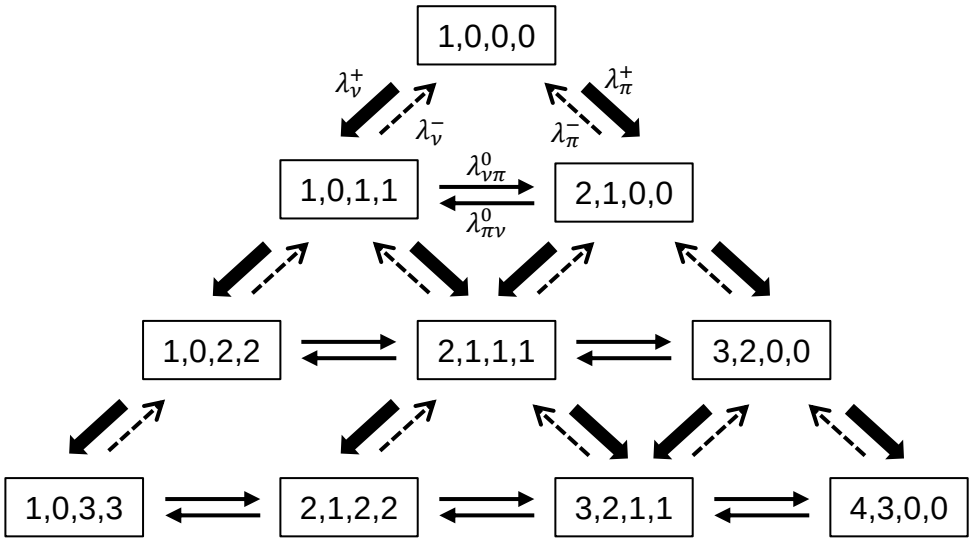

Figure 2.2: Schematic diagram of reaction pathway in a proton-induced reaction. Each state is characterized by a set of numbers corresponding to values of the particles and holes: $p_\pi, h_\pi, p_\nu, h_\nu$.

particle-hole annihilation, and τ is the mean life time of exciton state.

The energy-differential cross section of particle k, $\mathrm{d}\sigma_k^{PE}/\mathrm{d}E_k$ is calculated by

$$\frac{\mathrm{d}\sigma_k^{\mathrm{PE}}}{\mathrm{d}E_k} = \sigma^{\mathrm{CF}} \sum_{p_\pi=p_\pi^0}^{p_\pi^{\max}} \sum_{p_\nu=p_\nu^0}^{p_\nu^{\max}} W_k(p_\pi, h_\pi, p_\nu, h_\nu, E_k) S_{\mathrm{pre}}(p_\pi, h_\pi, p_\nu, h_\nu), \tag{2.7}$$

where σ^{CF} is the composite-nucleus formation cross section, W_k is the emission rate, and S_{pre} is defined by

$$S_{\mathrm{pre}}(p_\pi, h_\pi, p_\nu, h_\nu) = \int_0^{\tau_{\mathrm{eq}}} Q(p_\pi, h_\pi, p_\nu, h_\nu, t)\mathrm{d}t \tag{2.8}$$

.

Statistical decay

SD is described by Hauser-Feshbach formalization[50]. Because three different nuclei can be formed by absorption of a proton or neutron in the incident deuteron itself, the DDX for SD is expressed using three components:

$$\frac{\mathrm{d}^2\sigma_{\mathrm{SD}}}{\mathrm{d}E\mathrm{d}\Omega} = R_d \frac{\mathrm{d}^2\sigma_{(d,xn)}^{\mathrm{CCONE}}}{\mathrm{d}E\mathrm{d}\Omega} + R_p \frac{\mathrm{d}^2\sigma_{(p,xn)}^{\mathrm{CCONE}}}{\mathrm{d}E\mathrm{d}\Omega} + R_n \frac{\mathrm{d}^2\sigma_{(n,xn)}^{\mathrm{CCONE}}}{\mathrm{d}E\mathrm{d}\Omega}, \tag{2.9}$$

where R_d, R_p, and R_n are the formation fractions of individual compound nuclei, and $\mathrm{d}^2\sigma^{\mathrm{CCONE}}_{(d,xn)}/\mathrm{d}E\mathrm{d}\Omega$, $\mathrm{d}^2\sigma^{\mathrm{CCONE}}_{(p,xn)}/\mathrm{d}E\mathrm{d}\Omega$, and $\mathrm{d}^2\sigma^{\mathrm{CCONE}}_{(n,xn)}/\mathrm{d}E\mathrm{d}\Omega$ are the DDXs for (d,xn), (p,xn), and (n,xn) reactions, respectively. Each formation fraction is calculated with the Glauber model.

2.3.2 TALYS

TALYS is a general-purpose reaction model developed by Koning et al. [27]. TALYS uses the exciton [51] and Hauser-Feshbach models to calculate the pre-equilibrium and statistical decay processes. These models are also used in CCONE as mentioned above. To consider the contribution of the deuteron breakup, TALYS employs a simple model by Kalbach [52] as the following.

Breakup Reaction

The peak energy of ejectile generated in the A(a,b)B reaction, ϵ_0, is given by

$$\epsilon_0 = -\frac{A_b}{A_a}\left(\epsilon_a - B_{a,b} - \frac{Z_a Z_A}{9.5}\right) + \frac{Z_b Z_B}{9.5}, \tag{2.10}$$

where $B_{a,b}$ is the binding energy in the projectile (2.225 MeV for deuteron) and A and Z are the mass and atomic numbers, respectively. The energy distribution is assumed by a Gaussian distribution with a width

$$\Gamma = 1.15 + 0.12E_a - \frac{A_A}{140}, \tag{2.11}$$

where A_A is the incident energy in the laboratory frame, and Γ is in the unit of MeV.

The energy-differential cross section of breakup process is given by

$$\frac{\mathrm{d}\sigma^{\mathrm{BU}}_{a,b}}{\mathrm{d}E_b} = \sigma^{\mathrm{BU}}\frac{1}{\Gamma\sqrt{2\pi}}\exp\left(-\frac{(\epsilon_0 - E_b)^2}{\Gamma^2}\right), \tag{2.12}$$

where

$$\sigma^{\mathrm{BU}} = K_{d,b}\frac{(A_A^{1/3} + 0.8)^2}{1 + \exp\left(\frac{13 - E_a}{6}\right)}. \tag{2.13}$$

For the (d,xn) reaction, the normalization factor $K_{d,n} = 18$.

Angular Distribution

The angular distribution of the PE and SD processes can be calculated using physical models. However, the pre-equilibrium theory has some problems to describe angular distribution because the model is based on a compound-like concept instead of a direct one [53]. Thus, the angular distribution of the ejectile is given by Kalbach's empirical formula [54] instead of a physical method as follows:

$$\frac{\mathrm{d}^2\sigma_{a,xb}}{\mathrm{d}E_b\mathrm{d}\Omega} = \frac{1}{4\pi}\left[\frac{\mathrm{d}\sigma^{\mathrm{PE}}}{\mathrm{d}E_b} + \frac{\mathrm{d}\sigma^{\mathrm{comp}}}{\mathrm{d}E_b}\right]\frac{a}{\sinh(a)}[\cosh(a\cos\Theta) + f_{\mathrm{MSD}}(E_b)\sinh(a\cos\Theta)], \tag{2.14}$$

where $\mathrm{d}\sigma^{\mathrm{PE}}/\mathrm{d}E_b$ and $\mathrm{d}\sigma^{\mathrm{comp}}/\mathrm{d}E_b$ are the energy-differential cross sections of breakup and PE processes, respectively and parameter a is given in Ref [52], and the multi-step equilibrium ratio f_{MSD} is given by

$$f_{\mathrm{MSD}}(E_b) = \frac{\mathrm{d}\sigma^{\mathrm{PE}}}{\mathrm{d}E_b}\Big/\left[\frac{\mathrm{d}\sigma^{\mathrm{PE}}}{\mathrm{d}E_b} + \frac{\mathrm{d}\sigma^{\mathrm{comp}}}{\mathrm{d}E_b}\right]. \tag{2.15}$$

2.3.3 PHITS

In PHITS, deuteron-induced reaction is described by a two-step model, e.g., the intra-nuclear cascade process and the subsequent evaporation process. For light-ions such as deuteron and triton, the Liège intra-nuclear cascade (INCL) model [55] and JAERI quantum molecular dynamics (JQMD) [56] models are available as the intra-nuclear cascade process, and GEM [57] is used as the evaporation model.

INCL4.6

INCL model has been developed by the French Alternative Energies and Atomic Energy Commission (CEA) [58]. INCL can treat the proton, neutron, deuteron, light ions (triton, ^{3}He, α), and pion as the incident particle. The target nucleons are randomly given in Woods-Saxon and Fermi sphere distributions in positional and momentum spaces, respectively.

JQMD

The JQMD model was developed by Niita et al. of Japan Atomic Energy Agency. In the JQMD, the wave function of the i-th nucleon is expressed by

$$\phi_i(\boldsymbol{r}) = \frac{1}{(2\pi L)^{3/4}}\exp\left[-\frac{(\boldsymbol{r}-\boldsymbol{R}_i)^2}{4L} + \frac{i}{\hbar}\boldsymbol{r}\cdot\boldsymbol{P}_i\right], \tag{2.16}$$

where $\boldsymbol{R}_i$ and $\boldsymbol{P}_i$ are the central position and momentum vector of the i-th nucleon. The time evolution is calculated by variational principle:

$$\dot{\boldsymbol{R}}_i = \frac{\partial H}{\partial \boldsymbol{P}_i},\ \dot{\boldsymbol{P}}_i = \frac{\partial H}{\partial \boldsymbol{R}_i}, \tag{2.17}$$

where H is the Hamiltonian of the system.

GEM

GEM describes the evaporation process after the intra-nuclear cascade process. In the evaporation process, particles up to ^{28}Mg are emitted in the de-excitation of the residual compound nucleus. The probability P_j emitting particle j with energy between ε and $\varepsilon + \mathrm{d}\varepsilon$ is expressed as

$$P_j(\varepsilon)d\varepsilon = \frac{(2S_j+1)m_j}{\pi^2\hbar^2}\sigma_{\mathrm{inv}}(\varepsilon)\frac{\rho_d(E-Q-\varepsilon)}{\rho_i(E)}\varepsilon\mathrm{d}\varepsilon, \tag{2.18}$$

where S_j is spin, m_j is mass, $\sigma_{\mathrm{inv}}(\varepsilon)$ is the cross section for inverse reaction, E is the excitation energy, $\rho(E)$ is level density, and Q is the Q-value of emission of particle. The subscripts i, j , and d denote parent nucleus, emitted particle, and daughter nucleus, respectively. The cross section for inverse reaction $\sigma_{inv}(\varepsilon)$ is expressed as

$$\sigma_{\mathrm{inv}}(\varepsilon) = \begin{cases} \sigma_g c_n(1+b/\varepsilon) & \text{for neutrons} \\ \sigma_g c_n(1-V/\varepsilon) & \text{for charged particles,} \end{cases} \tag{2.19}$$

where $\sigma_g = \pi R^2$ is the geometric cross section, and V is the Coulomb barrier. According to Ref. [59], the level density is expressed as

$$\rho(E) = \frac{\pi}{12}\frac{e^{2\sqrt{a(E-\delta)}}}{a^{1/4}(E-\delta)^{5/4}} \qquad \text{for } E \geq E_x, \tag{2.20}$$

and

$$\rho(E) = \frac{1}{T}e^{(E-E_0)/T} \qquad \text{for } E < E_x, \tag{2.21}$$

where $a = A_d/8$ [MeV^{-1}] is the level density parameter, and T is the nuclear temperature, $E_x = 2.5 + U_x + \delta$. Here U_x is defined as $U_x = 150/A_d$, and δ is given in Ref. [59]. To connect Eqs. (2.20) and (2.21) smoothly, E_0 is defined as,

$$E_0 = E_x - T(\log T - 0.25\log a - 1.25\log U_x + 2\sqrt{aU_x}). \tag{2.22}$$

The decay width Γ_j is given by integrating Eq.(2.18) respect to emission energy from Coulomb barrier V to maximum excitation energy $(E-Q)$:

$$\Gamma_j = \frac{g_j \sigma_g \alpha}{\rho_i(E)} \int_V^{E-Q} \left(1 + \frac{\beta}{\varepsilon}\right) \rho_d(E - Q - \varepsilon) \varepsilon \mathrm{d}\varepsilon. \tag{2.23}$$

The branching ratio p_j is given by

$$p_j = \frac{\Gamma_j}{\sum_k \Gamma_k}. \tag{2.24}$$

The particles are emitted in all directions uniformly in the center-of-mass system, and directions are determined by random numbers.

$$\rho(E) = \begin{cases} \dfrac{\pi}{12} \dfrac{e^{2\sqrt{a(E-\delta)}}}{a^{1/4}(E-\delta)^{5/4}} & (E \geq E_x) \\ \dfrac{1}{T} e^{(E-E_0)/T} & (E < E_x). \end{cases} \tag{2.25}$$

2.4 Experiment

2.4.1 Experimental Facility

The experiment was performed at the high energy experimental room in the Center for Accelerator and Beam Applied Science, Kyushu University. The layout of the facility is shown in Fig. 2.3. Negative deuteron ions (D^-) are served by the ion source and injected into an 8 MV Tandem Van de Graaf accelerator. In the tandem accelerator, D^- ions are accelerated up to a high voltage terminal where they pass through a thin carbon foil, and stripped electrons then converted into positive ions (D^+). D^+ ions are accelerated once again by the terminal and extracted at the desired energy. The deuteron beam is then transported into the high energy experimental room.

2.4.2 Neutron Detector

The neutron spectra were detected using an EJ-301 liquid organic scintillator [60] that was optically coupled with a photomultiplier tube. Fundamental specifications of the EJ-301 scintillator are shown in Table 2.3. The physical and chemical properties are identical to the NE-213, which has been widely used as a fast neutron detector due to the excellent pulse shape discrimination (PSD) properties.

The scintillation mechanism of the detector is explained using the energy level diagram of organic scintillator molecules as shown in Fig. 2.4. As radiation passes through the scintillator, the valence electrons of molecules are excited and occupy the π-molecular orbitals, which are called spin singlet (S_i) or triplet states (T_i).

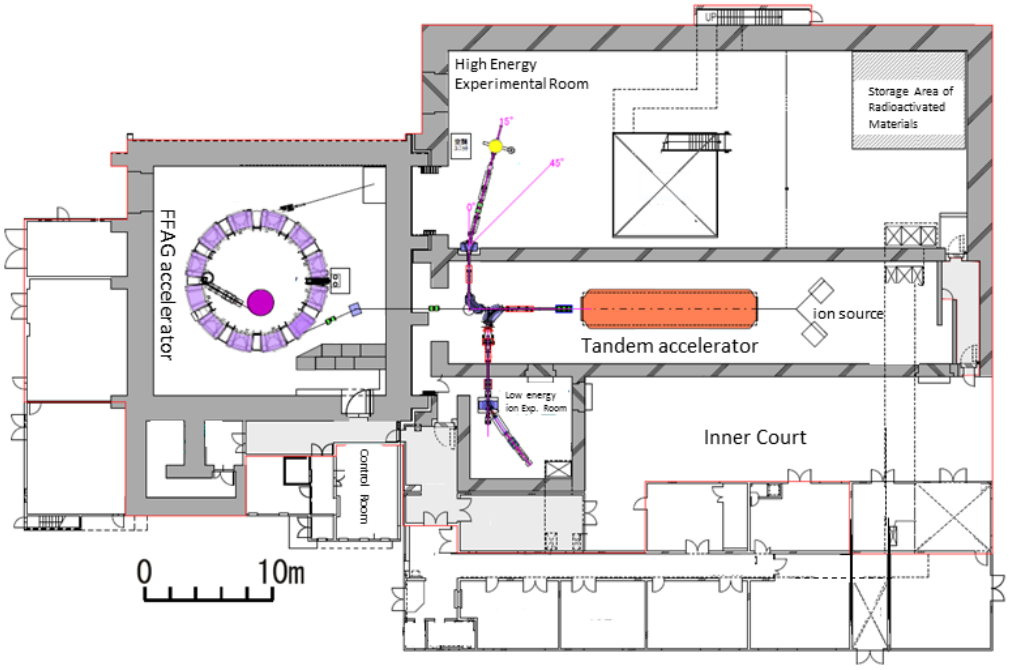

Figure 2.3: Bird's-eye view of the experimental facility.

The singlet states generally decay immediately ($\leq$10 ps) to the S_1 state without emission of radiation (internal degradation) and the S_1 state decays to the ground state (S_0) within a few nanoseconds with emission (fluorescence). For the triplet states, a similar internal degradation occurs, which brings the system to the lowest triplet state (T_0). The T_0 state, however, decays to the S_0 state after delayed time (phosphorescence) because this transition is highly forbidden by multiple selection rules. The excitation of the valence electrons varies depending on the energy loss per unit length of incident particle. In an organic scintillator, a high-energy loss produces a high density of excited molecules, which results in increased intersystem crossings. These reactions hinder the singlet internal degradation, leading to the enhancement of the slow component.

The PSD property arises from the fraction of the slow component of the scintillation. When the fast neutron interacts with the scintillator, it recoils protons while a γ-ray produces electrons. Because a proton loses higher energy per unit length, the pulse generated by a fast neutron has a larger slow component. The PSD technique is detailed in Section 2.4.3.

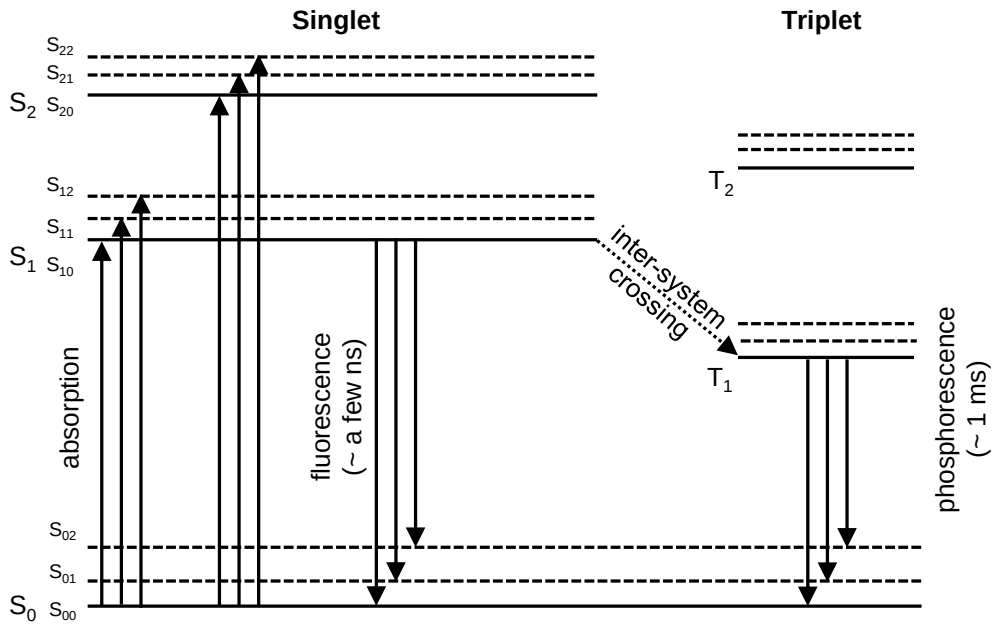

Figure 2.4: Typical energy level diagram of a π-molecule.

Table 2.3: Property of EJ-301 detector taken from Ref. [60].

Components	xylene (C_8H_{10}), naphthalene ($C_{10}H_8$)
Light output	78 % anthracene
Wavelength of maximum emission	425 nm
Decay times of first three components	3.16, 32.3, 270 ns
Mass density	0.874 g/cm^3
Refractive index	1.505
Number of H atoms	4.82×10^{22} [cm^{-3}]
Number of C atoms	3.98×10^{22} [cm^{-3}]
Number of electrons	2.27×10^{23} [cm^{-3}]

2.4.3 Experimental Procedure

The experimental procedure followed the procedure used in previous works at Kyushu University [38], [39], [41]. Figure 2.5 shows the experimental setup of this work. Using an 8 MV Tandem Van de Graaf accelerator, the 6.7-MeV/u deuteron beam was aimed at a compact target chamber. The chamber had an inner diameter of 260-mm with 4-mm-thick walls, and a 2-cm-high window covered with a 125-µm-thick Mylar film to reduce the neutron scattering within the stainless steel walls. The chamber was electrically insulated from the other experimental apparatuses,

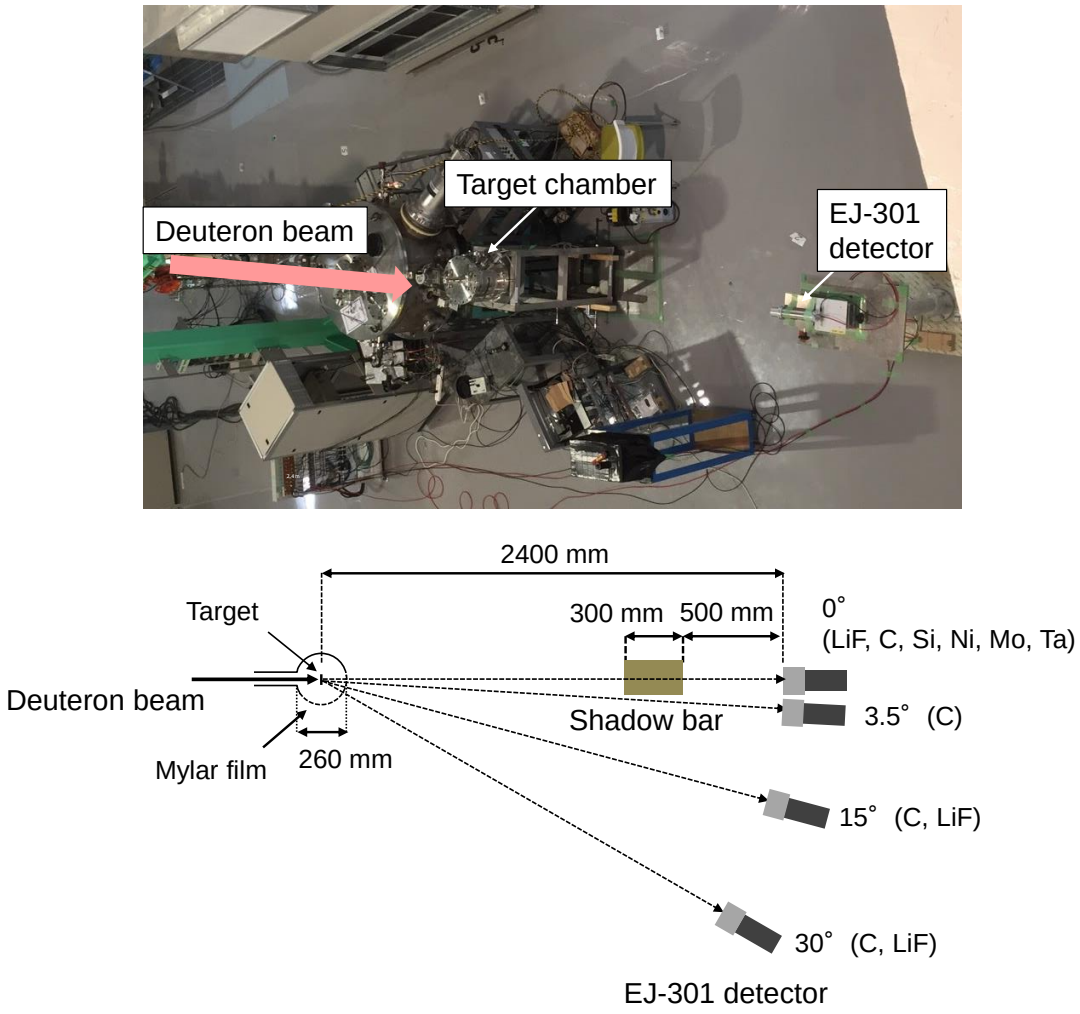

Figure 2.5: Photograph (upper) and schematic (lower) drawing of the experimental setup. The shadow bar in the lower drawing was placed only in the background measurements.

acting as a Faraday cup to receive the deuteron beam current. The average beam current was recorded with an ORTEC 439 digital current integrator (I.C.)

The LiF, C, Si, Ni, Mo, and Ta targets were mounted on an aluminum frame and set in the chamber. The target thicknesses and ranges of the deuteron in the targets are listed in Table 2.4. The targets were sufficiently thick to stop the incident deuterons completely. The deuteron range was calculated using the Stopping and Range of Ions in Matter (SRIM) code [61]. Emitted neutrons were

detected using an EJ-301 liquid organic scintillator (5.08-cm in diameter × 5.08-cm in length) that was optically coupled with a Hamamatsu R7724 photomultiplier and placed 2.4 m from the target. The neutron spectra were measured at emission angles listed in the fourth column.

Figure 2.6 shows a block diagram of the measurement circuit. The signals from the detector were divided in two using a signal divider. If one of the split signals reached a gate generator (G.G.) through a constant-fraction discriminator (CFD), an gate signal for an analog-to-digital converter (ADC) was created. The other split signal was then recorded by the ADC by integrating the electric charges induced by the total slow and slow components of the signal. To prevent the signals from reaching the ADCs while the CAMAC system was busy, a CFD logic pulse initialized a veto signal. The veto signal was terminated by a pulse from an output register, which is generated by CAMAC when the ADC acquires data. The ratio of dead time of the data acquisition system to the measurement time was estimated as the ratio of the number of ungated and gated events, which was less than 20%.

To estimate the contribution of detected neutrons caused by scattering from the floor and surrounding walls of the experimental room, additional background measurements were performed for all the measurement conditions using an iron shadow bar, 150-mm wide × 150-mm high × 300 mm thick. This bar was placed between the targets and the detector, as shown in Fig. 2.5. The contribution of background neutrons was subtracted in the analytical procedure described in Section 2.5.1.

Table 2.4: Target thickness and the range of 6.7 MeV/u deuteron in the target. The range of the deuteron was calculated using SRIM [61].

Target	Thickness [mm]	Deuteron range [mm]	Measured angle
LiF	1.0	0.585	0°, 15°, 30°
C	2.0	0.608	0°, 3.5°, 15°, 30°
Si	1.0	0.725	0°
Ni	0.5	0.241	0°
Mo	0.5	0.256	0°
Ta	0.5	0.213	0°

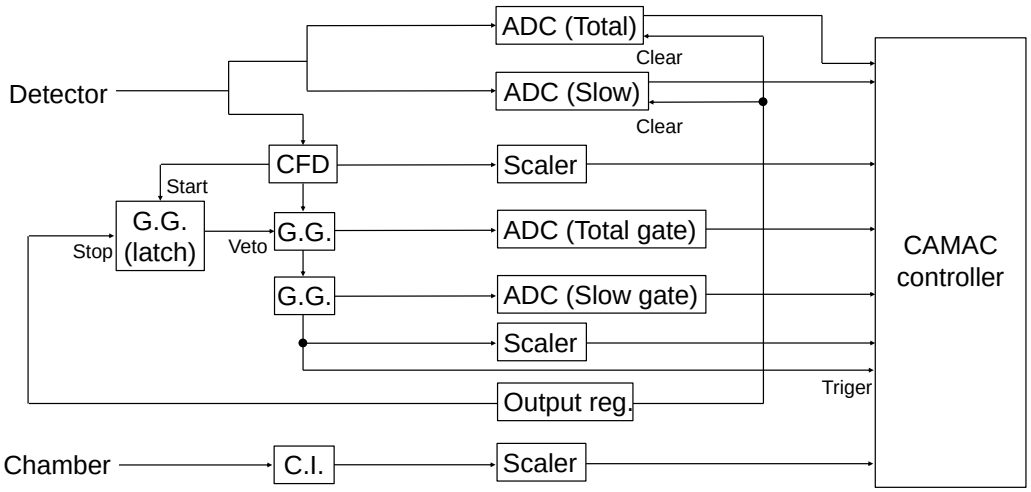

Figure 2.6: Circuit diagram used in the measurements.

2.5 Data Analysis

2.5.1 Particle Identification

A conventional two-gate integration method was used for the particle identification since the detector is sensitive to both γ-rays and neutrons. Figure 2.7 shows the typical pulse shape of the EJ-301 detector caused by detection of γ-rays and neutrons. The slow and total components of the pulse shape were derived by integrating the slow and total components, respectively. As shown in Fig. 2.7, the pulse shape of neutrons have a larger slow component than that of γ-rays. Thus, when the total and slow components of each signal are plotted in the two-dimensional plane, neutron and γ-ray events separate as shown in Fig. 2.8. However, neutron and γ-ray events with low pulse height are not completely distinguished. Neutron events with low pulse height were derived by following procedure: the two-dimensional plot was vertically sliced at $x = x_0$ as shown in Fig. 2.9. The neutron and γ-ray events were fitted by two Gaussian distributions

$$f(x = x_0, y) = \frac{N_n}{\sqrt{2\pi\sigma_n^2}} \exp\left[-\frac{(y-\mu_n)^2}{2\sigma_n^2}\right] + \frac{N_\gamma}{\sqrt{2\pi\sigma_\gamma^2}} \exp\left[-\frac{(y-\mu_\gamma)^2}{2\sigma_\gamma^2}\right], \quad (2.26)$$

where N_n, μ_n, σ_n, N_γ, μ_γ, and σ_γ are fitting parameters. This technique was applied for the pulse height range of $174 \leq x_0 \leq 240$. Neutron events were extracted

down to 0.244 MeV electron-equivalent energy, which allowed the minimum neutron energy of the experimental results to be 2 MeV.

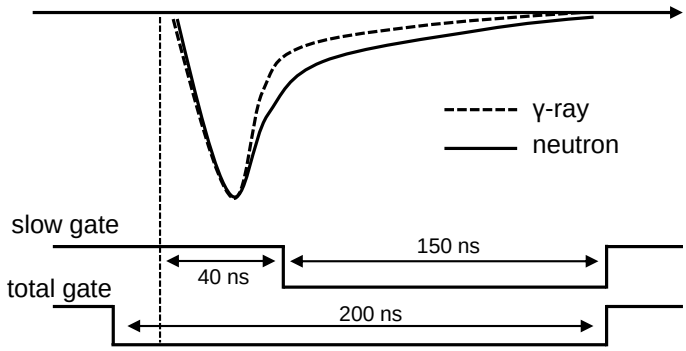

Figure 2.7: Typical pulse shape of EJ-301 detector caused by neutrons and γ-rays. The total and slow components were derived by integrating the pulse shape with the total and slow gates, respectively.

2.5.2 Calibration of Light Output

The light output spectra of neutron events were converted into units of electron-equivalent energies. For this calibration, standard γ-ray sources ^{137}Cs and ^{60}Co were used. Additionally, calibration for the higher light output region was performed by using γ-rays emitted by $^{12}\mathrm{C}(d,p)^{13}\mathrm{C}^{*}$ and $^{12}\mathrm{C}(d,d)^{12}\mathrm{C}^{*}$ reactions and neutrons emitted by $^{7}\mathrm{Li}(d,n)^{8}\mathrm{Be}_{\mathrm{g.s.}}$ and $^{12}\mathrm{C}(d,n)^{13}\mathrm{N}_{\mathrm{g.s.}}$ corresponding to the maximum light output.
Figure 2.10 shows the pulse height distributions obtained for two γ-ray sources ^{137}Cs (662 keV) and ^{60}Co (1173 and 1333 keV). In the pulse height distribution, a Compton edge is clearly observed. According to Ref [62], the position of observed Compton edge is affected by the detector resolution. The relationships between the position of the ideal Compton edge, E_{comp}, and the light output in units of electron-equivalent energy where the number of count equals to the half of maximum, $L_{1/2}$, can be determined by

$$L_{1/2}/E_{\mathrm{comp}} \sim 1.03. \tag{2.27}$$

The electron energy corresponding to Compton edge E_{comp} is expressed by

$$E_{\mathrm{comp}} = \left[\frac{2h\nu}{m_e + 2h\nu}\right] h\nu, \tag{2.28}$$

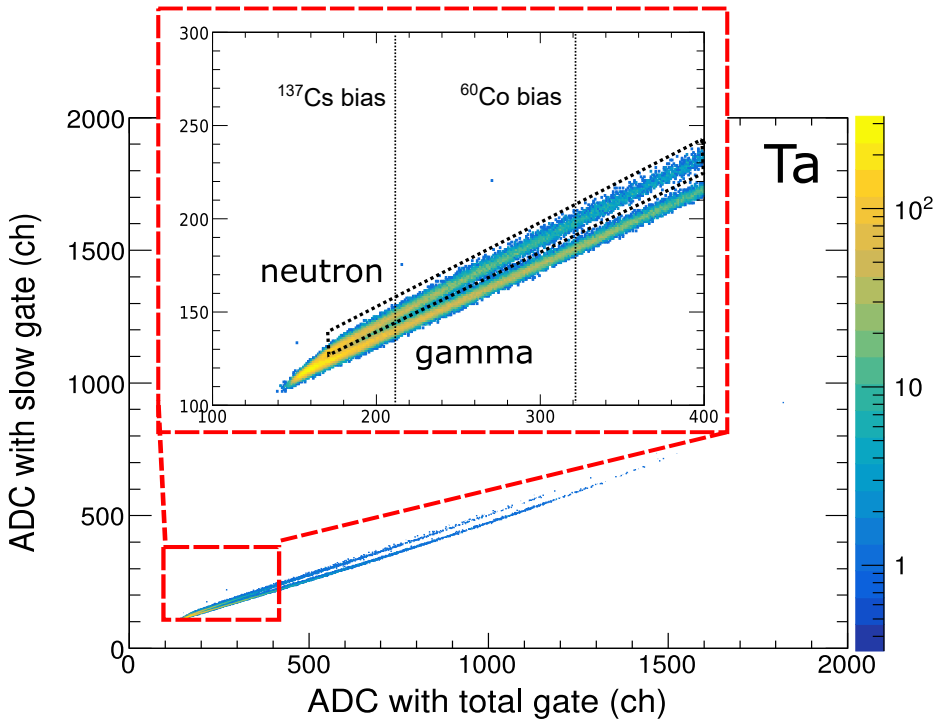

Figure 2.8: Two-dimensional plot of pulse integration with total (x-axis) and slow (y-axis) components for the Ta target. The ^{137}Cs (662 keV) and ^{60}Co (1173 and 1332 keV) biases are also displayed.

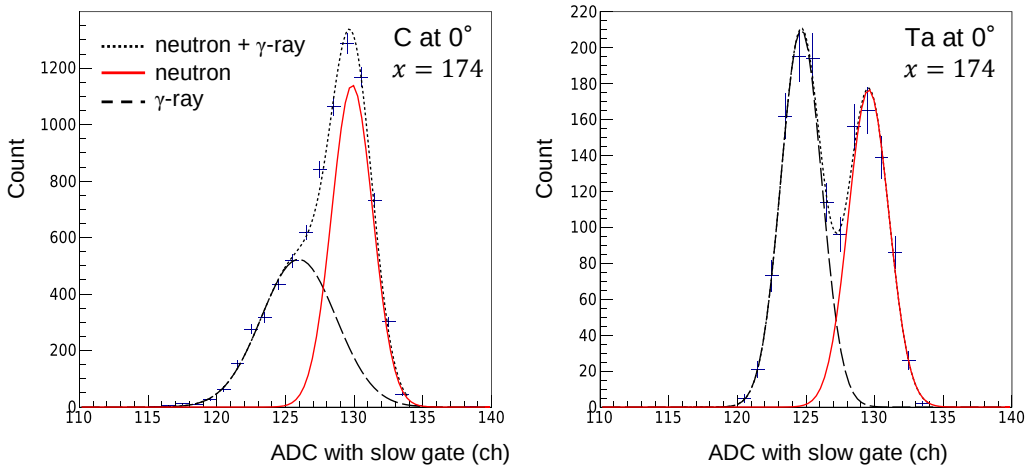

Figure 2.9: Pulse height distribution at $x = 174$ obtained for the C (left) and Ta (right) targets. Neutron and γ-ray events were fitted by two Gaussian functions.

where $h\nu$ is the incident γ-ray energy and $m_e = 0.511$ MeV denotes the rest mass energy of an electron.

For the calibration points of neutrons emitted in the (d,n) reactions, the maximum light output $L_{\max}$ was used. The neutron energy emitted in a scattering angle θ, $E_n(\theta)$, can be calculated by a non-relativistic kinematics formula

$$\sqrt{E_n(\theta)} = \frac{(m_d m_n E_d)^{1/2}\cos\theta}{m_r + m_n} + \left[\frac{m_d m_n E_d \cos^2\theta}{(m_r + m_n)^2} + \frac{m_r\{Q + E_d(1 - m_d/m_r)\}}{m_r + m_n}\right]^{1/2}, \tag{2.29}$$

where m_d, m_n, m_r represent the rest mass energies of deuteron, neutron, and residual nucleus, respectively, E_d is the incident deuteron energy, and Q is the Q-value of the (d,n) reaction. The maximum light output can be reached when the neutron transfers its total kinetic energy to a proton in the EJ-301 scintillator. Thus, the kinematic energy of proton E_p can be approximated by $E_p \sim E_n$. The light output $L_{\max}$ was calculated by the formula [63]

$$L_{\max} = L(E_n(\theta)) = 0.81E_n(\theta) - 2.8\left[1.0 - \exp(-0.2E_n(\theta))\right]. \tag{2.30}$$

Figure 2.11 shows the calibration curve used in this work. Good linearity was confirmed up to 7 MeV, which corresponds to neutron energy of 12 MeV. An example of light output distribution is shown in Fig. 2.12.

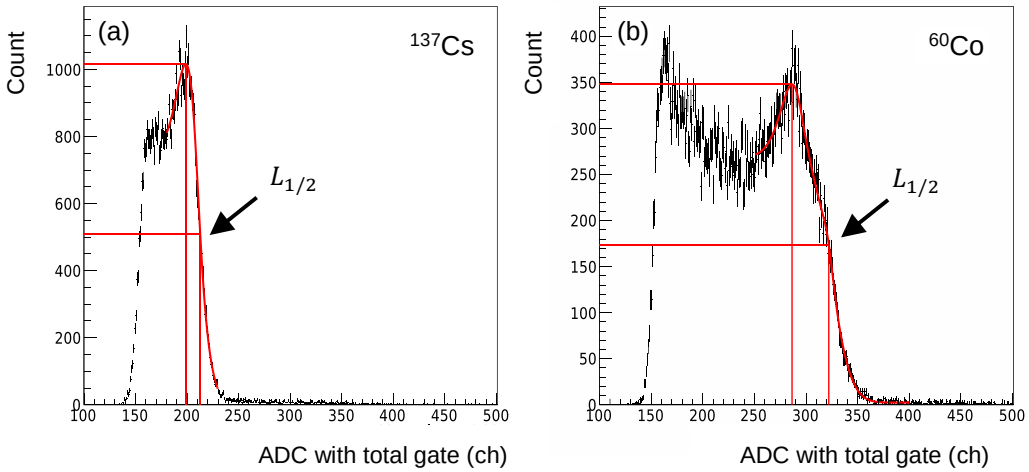

Figure 2.10: Fitting results of pulse height distributions obtained for the γ-ray measurements of ^{137}Cs (662 keV) and ^{60}Co (1173 and 1333 keV).

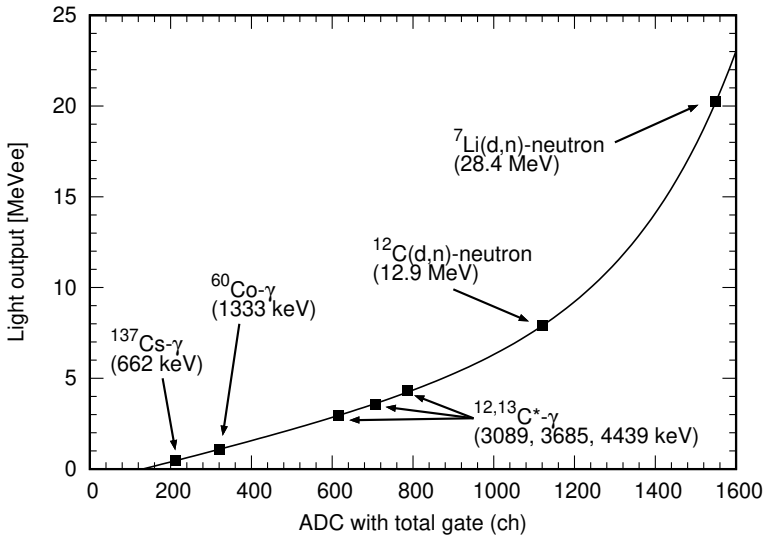

Figure 2.11: Calibration curve and calibration points obtained in this work.

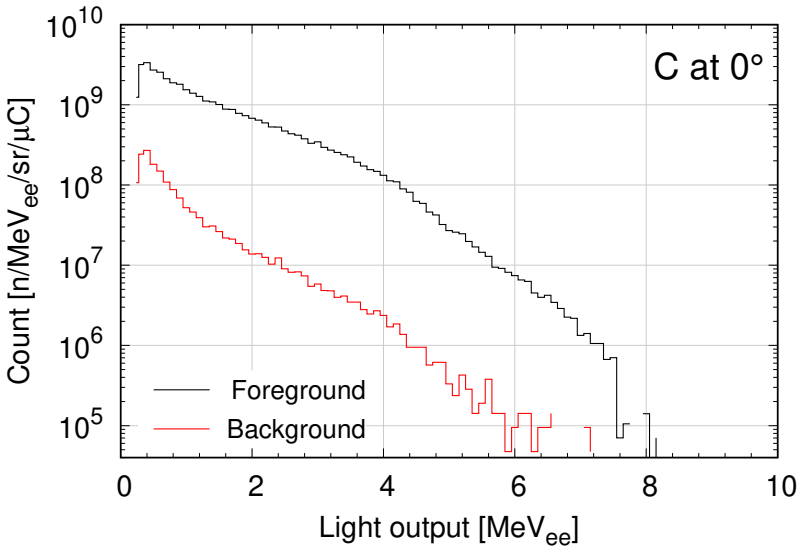

Figure 2.12: Light output distribution obtained for the foreground and background measurements of the C target at an emission angle of 0°.

2.5.3 Unfolding of Light Output Distribution

Neutron energy spectra were derived by an unfolding process of light output distributions using FORIST [64] and RooUnfold [65] codes. Here, a description of the two unfolding codes is given.

FORIST code

The FORIST code is an unfolding code based on the least-squares method. The outline of unfolding with the least-square method is as follows. The measured light output spectra $M(L)$ is expressed as a folding of the desired neutron energy spectra $T(E)$

$$M(L) = \int R(L,E)T(E)\mathrm{d}E, \tag{2.31}$$

where $R(L,E)$ is the response function of the detector. The Eq.(2.31) must be reduced to a matrix unfolding problem, which can be solved numerically:

$$M_i = \sum_{j=1}^{N_S} R_{ij}T_j, \tag{2.32}$$

where M_i $(i = 1, 2, \cdots N_R)$ and T_j $(j = 1, 2, \cdots N_S)$ are the discretized light output spectra and neutron energy spectra, respectively, and R_{ij} is the response matrix. The neutron energy spectra T_j can be uniquely determined if $N_S = N_R$, but this way cases a large error on T_j owing to the propagation of errors on M_i and R_{ij}. To reduce the error, the FORIST code defines the chi-square value as

$$\chi^2 = \sum_{i=1}^{N_R} w_i \left(M_i - \sum_{j=1}^{N_S} R_{ij}T_j \right)^2, \tag{2.33}$$

where w_i is a weight vector, defined as the set of inverse square of statistical uncertainties on M. The minimum chi-square value satisfies $\frac{\partial \chi^2}{\partial T_k} = 0$ for any $k = (1, 2, \cdots N_S)$, yielding

$$\sum_{i=1}^{N_R} w_i R_{ik} \left(M_i - \sum_{j=1}^{N_S} R_{ij}T_j \right) = 0. \tag{2.34}$$

Rearranging and dropping indices gives

$$T = \left(R^\dagger W R\right)^{-1} R^\dagger W M, \tag{2.35}$$

where $R^\dagger$ is the transpose of R matrix. In this calculation, computer round-off errors may result in large oscillations in the solution vector. Thus, the FORIST code reduces the oscillations of the solution vector by constraining the least-squares solution to be near zero.

RooUnfold code

The RooUnfold code was designed to provide a framework for different unfolding algorithms such as iterative Bayes [66], Singular Value Decomposition [67], etc. Because the iterative Bayes method was used in this work, here describes the outline of the unfolding technique.

The unfolded spectrum $\hat{n}(C_i)$ can be derived by the formula

$$\hat{n}(C_i) = \sum_{j=1}^{N_E} M_{ij} n(E_j), \tag{2.36}$$

where $n(E_j)$ is the measured spectrum, unfolding matrix M_{ij} is defined as

$$M_{ij} = \frac{P(E_j|C_i) n_0(C_i)}{\varepsilon_i \sum_{l=1}^{N_C} P(E_j|C_l) n_0(C_l)}. \tag{2.37}$$

The $P(E_j|C_i)$ is the $N_E \times N_C$ response matrix, i.e., the probability for the $n_0(C_i)$ being detected as $n(E_j)$, $\varepsilon_i = \sum_{j=1}^{N_E} P(E_j|C_i)$ is the detection efficiency for $n(C_i)$, and $n_0(C_i)$ is the prior distribution, which is initially defined as flat distribution and updated on subsequent iterations.

Response matrix

The response matrix of the EJ-301 detector used in the unfolding process was obtained by the SCINFUL-QMD code [68], [69]. The SCINFUL-QMD is a Monte Carlo simulation code, which treats the particle transport and nuclear reactions in the scintillator. The simulation begins with the interaction of incident neutron with a H or C atom in the scintillator. Table 2.5 lists the initial reaction channels considered in the SCINFUL-QMD. The light outputs of emitted charged particles, such as p, d, α etc., are calculated from kinematic energies of the particles using an empirical formula [63]. Calculated response matrix used in the unfolding process is shown in Fig. 2.13.

Table 2.5: Initial reaction channels considered in the SCINFUL-QMD code [68].

H(n,n)	C(n,n)	C(n,γ)	C(n,α)	C(n,3α)	C(n,np)
C(n,2n)	C(n,p)	C(n,d)	C(n,t)	C(n,^{3}He)	

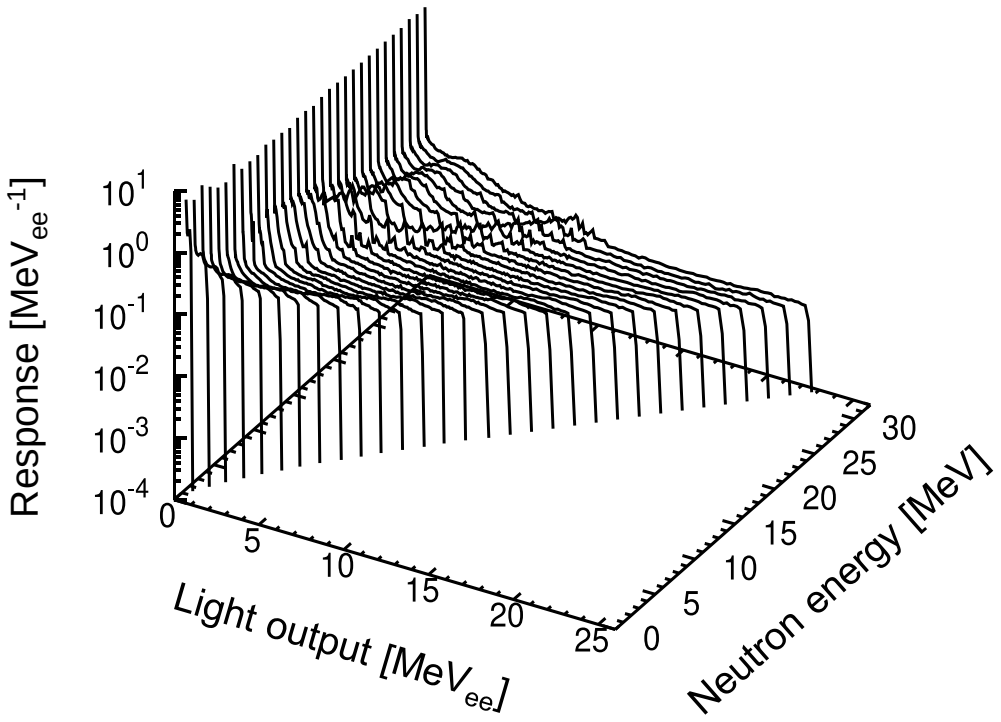

Figure 2.13: Response matrix of the EJ-301 detector calculated with the SCINFUL-QMD code [68], [69].

2.5.4 Uncertainty Analysis

Uncertainties in the experimental data include three major factors: the geometry of the detector, the response functions of the detector, and the scattering of neutrons in a thick target and the air. The first was estimated to be 2% as the uncertainty in the determination of the solid angle of finite-size detector. The second was estimated to be 17% [41], considering the effect of scattering in the aluminum housing of the detector and the difference in the response functions calculated by SCINFUL-QMD and CECIL [70] codes. The third was estimated to be 4%, based on the neutron transport calculation using PHITS [24]. Contributions of the other sources, such as the particle identification, subtraction of background contributions, beam integration, and dead time corrections, were estimated to be less than 1%.

2.6 Results and Discussion

2.6.1 Comparison of Unfolding Codes

The unfolding results generally depend upon factors such as the calculation methods, unfolding codes, and the initial guess spectrum if the initial spectrum is required. To investigate the dependency of the derived neutron spectra on the calculation method, the neutron spectra were derived by two different unfolding methods: the FORIST and iterative Bayes of RooUnfold. As mentioned in Section 2.5.3, these two unfolding methods are mutually independent, and therefore, one can see the dependency by comparing them.

Figure 2.14 compares the neutron spectra from the LiF, C, Si, Ni, Mo, and Ta targets at an emission angle of 0° derived by the FORIST and RooUnfold. Good agreement between the two unfolding code was confirmed for all the targets except for the difference in the high-energy region. This difference is mainly due to the treatment of statistical errors in the unfolding method. The FORIST uses the weight vector defined as the inverse square of statistical errors on measured light output distributions while the RooUnfold does not consider the statistical errors. Since low statistics are obtained in the high-light output events as shown in Fig. 2.12, a significant difference appeared in the high-energy neutron yields.

In the neutron spectra, some characteristic kinks were observed except for the Ta target. Both the unfolding results for the light target elements have some kinks, e.g., 5.5, 15, and 26 MeV for LiF and 5.5, 8.5, and 12 MeV for C etc. As is detailed in Section 2.6.4, these kinks were caused by deuteron breakup or proton-transfer reactions to discrete levels of residual nuclides.

Hereinafter, neutron spectra derived by the FORIST are represented as the results of this work because good agreement of the two unfolding codes was confirmed.

2.6.2 Comparison with Previous Works

Comparison with time-of-flight results

To validate the unfolding results, the derived spectra were compared with preciously reported data. Figure 2.15 shows the neutron spectra form the C target at emission angles of 3.5°, 15°, and 30° in this work compared with previous data [71]. The data of Ref. [71] were measured using conventional time-of-flight (TOF) method in similar conditions: the incident energy was 7.0 MeV/u and emission angles were 3.5°, 16.7°, and 32.3°. Although the measurement conditions were slightly different, there was good agreement except for the difference in the high-energy region. In the TOF spectrum of Ref. [71], three kinks were clearly

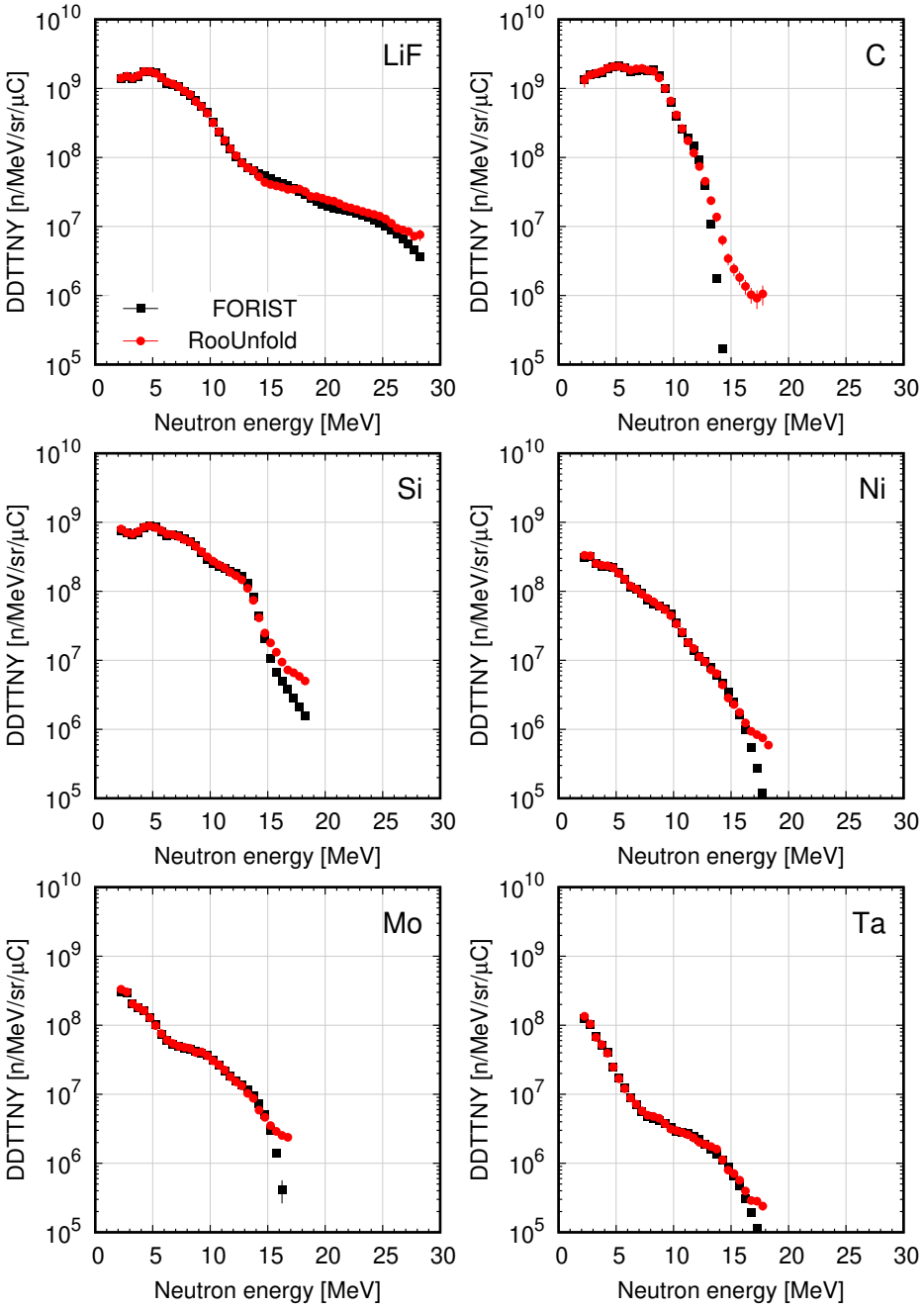

Figure 2.14: Double-differential neutron spectra at an emission angle of 0° derived by FORIST (least-squares method) and RooUnfold codes (iterative Bayesian method).

measured at 10, 11, and 13 MeV. These kinks corresponded to discrete levels of the ^{13}N, with the excitation energies of 3502 and 2365 keV and the ground state, respectively, formed by the ^{12}C(d,n)^{13}N reaction. In the present study's results, however, only smoothed kinks were measured. This is due to the poor energy resolution in the unfolding method compared to the TOF method.

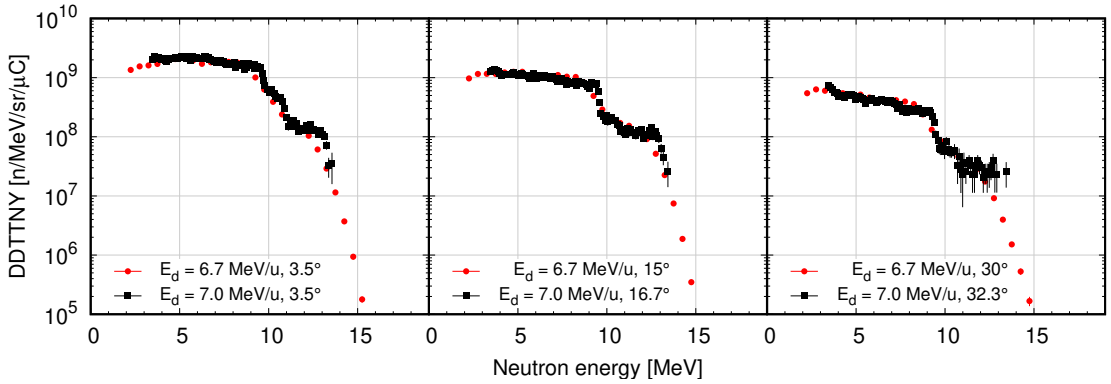

Figure 2.15: Comparison of double-differential neutron spectra from the C target measured in this with the previously measured data [71].

Comparison with data at Kyushu University

Thus far, DDTTNY data of the (d,xn) reactions for the various target materials have been measured using a deuteron energy of <5 MeV/u at Kyushu University [38]–[41], as listed in Table 2.2 of Section 2.1. These data were measured by the unfolding technique, same as in this work. To investigate the dependencies of DDTTNYs on the incident deuteron energy, the neutron yields of this work were compared with previous data.

Figure 2.16 compares the DDTTNY spectra from the C target by bombardment of deuterons with 2.5, 4.5, and 6.7 MeV/u. The neutron yield and maximum emission energy increase as the incident energy increases. The kinks corresponding proton-transfer reactions are clearly seen for the low-incident energies. One plausible reason is that the probability of the residual nuclei transit to the higher excitation states.

Next, the dependence of neutron yields on the incident energy was investigated using the angle-differential neutron yields (ADNYs). The ADNYs were derived by integrating the DDTTNY spectra over a neutron energy range, from 2 MeV to the maximum emission energies. Figure 2.17 shows the ADNYs by bombardment of 2.5-, 4.5-, and 6.7-MeV/u deuterons. The ADNY exponentially decreases as the target atomic number increases, and decreases more steeply as the incident

energy decreases. This is due to the decrease of reaction cross sections caused by the Coulomb barrier of target nuclei.

2.6.3 Comparison with (t, xn) Spectra

Figure 2.18 compares both the (d,xn) and (t,xn) spectra at an incident energy of 6.7 MeV/u. As mentioned above, some characteristic bumps were measured in the (d,nx) spectra, except for the Ta target. The (t,xn) spectra show monotonic decreases with increasing emission energy, and they have no characteristic shape like that observed in the (d,xn) spectra. A likely reason is the difference in neutron separation energy between tritons ($S_n = 6.26$ MeV) and deuterons ($S_n = 2.22$ MeV). Thus, triton dissociation does not occur easily at relatively low-incident energies, and the contribution of triton breakup is expected to be less than that of deuteron breakup.

Next, Figure 2.19 shows the ADNYs of the (d,xn) and (t,xn) reactions regarding the atomic number of the target elements. Additional data for O ($Z = 8$), W ($Z = 74$), Pt ($Z = 78$), and Au ($Z = 79$) were taken from Ref. [37] for the triton incidence. The typical statistical uncertainties of our data are approximately 1.3%, and those in Ref. [37] are less than 1%. For both incidences, ADNYs decreased as the atomic number Z of the target increased. In the low-Z region, deuterons generated more neutrons even though the total kinematic energy of deuteron was smaller than that of triton, and deuteron breakup enhanced the neutron production. In the high-Z region, however, the deuteron ADNYs decreased more steeply. Section 2.6.4 provides a detailed discussion about deuteron incidence.

2.6.4 Comparison with Theoretical Predictions

PHITS

In PHITS, the deuteron- and triton-induced reactions are described by two-step models, i.e., the dynamic and subsequent evaporation processes. Some reaction models are implemented in the PHITS, e.g., INCL version 4.6 (INCL4.6) [33] and JQMD as the dynamical process, and the generalized evaporation model (GEM) [57]. To validate the PHITS predictions, the measured (d,xn) spectra and the (t,xn) spectra of Ref. [37] were compared with the theoretical calculation using PHITS version 3.02. The calculations were performed using INCL4.6 and JQMD as the dynamic process, and GEM as the evaporation model. Hereinafter, these models are referred to as INCL4.6/GEM and JQMD/GEM, respectively. In the calculation, a natural abundance of targets listed in Table 2.6 were considered.

Figure 2.20 compares the (d,xn) spectra in this work with the PHITS calculations. PHITS employed the MWO formula [72] to calculate the deuteron-

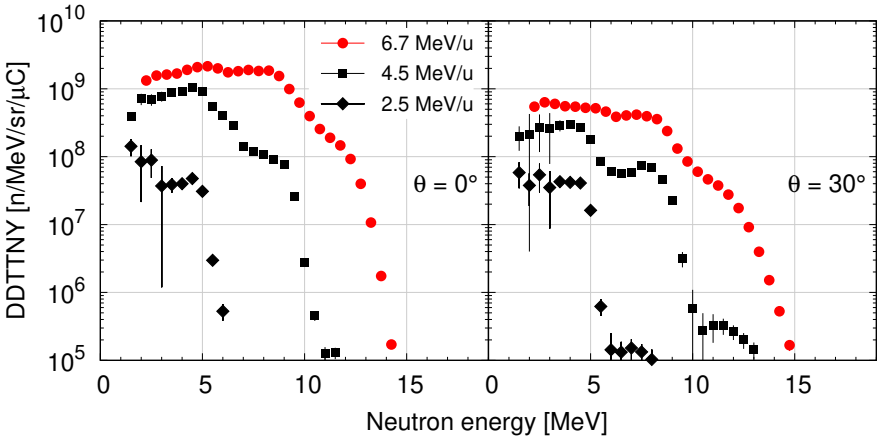

Figure 2.16: Double-differential neutron spectra by bombarding 6.7-MeV/u (red circles), 4.5-MeV/u (black squares), and 2.5-MeV/u (black diamonds) deuterons (a) at an emission angle of 0° and (b) 30°. The 2.5-MeV/u and 4.5-MeV data are taken from Ref. [38]–[41].

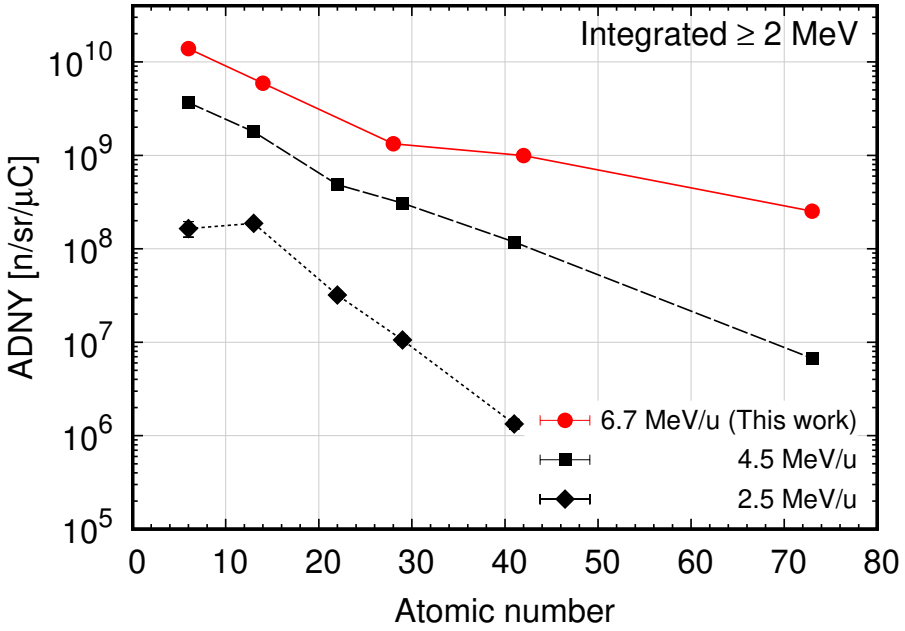

Figure 2.17: Angle-differential neutron yield by bombarding 6.7-MeV/u (red circles), 4.5-MeV/u (black squares), and 2.5-MeV/u (black diamonds) deuterons at an emission angle of 0°. The emitted neutrons with energy ≥2 MeV were integrated. The 2.5-MeV/u and 4.5-MeV data are taken from Ref. [38]–[41]. The lines were drawn to guide the eyes.

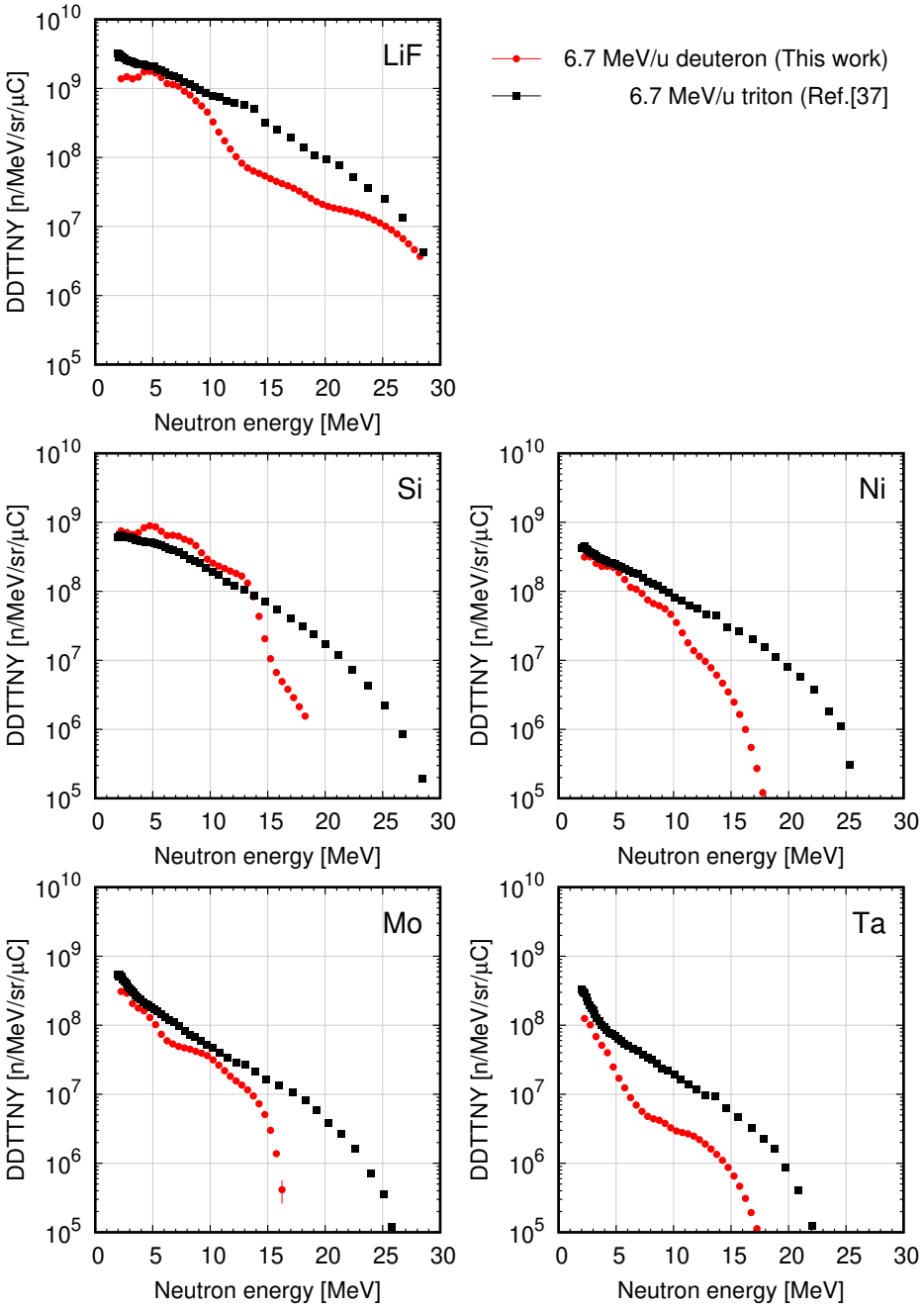

Figure 2.18: Angle-differential neutron spectra by bombarding deuterons (red circle) and tritons (black square) with an incident energy of 6.7 MeV/u at an emission angle of 0°. The triton data is taken from Ref. [37].

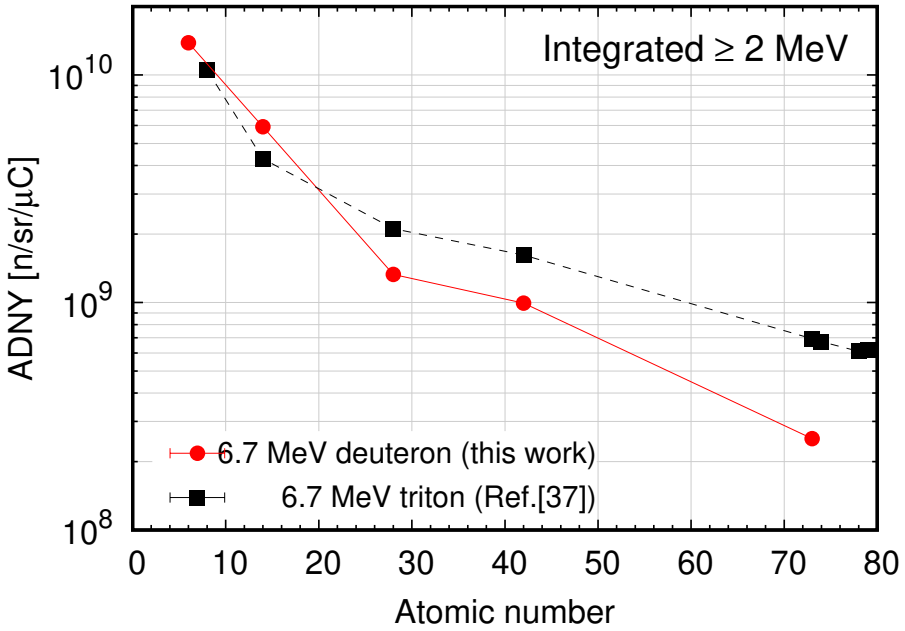

Figure 2.19: Angle-differential neutron yield by bombarding deuterons (red circle) and tritons (black square) with an incident energy of 6.7 MeV/u at an emission angle of 0°. The emitted neutrons with energy ≥2 MeV were integrated. The triton data is taken from Ref. [37]. The solid and dashed lines were drawn to guide the eyes.

induced reaction cross sections. Moreover, the distorted wave Born approximation (DWBA) calculation for the transition to discrete revels of the residual nuclei were performed for the ^{6,7}Li(d,n)^{7,8}Be$_{\mathrm{g.s.}}$ and ^{12,13}C(d,n)^{13,14}N$_{\mathrm{g.s.}}$ reactions.

Both calculations generally reproduced the spectral shapes. The INCL4.6/GEM generally overestimates the magnitudes except for the C target. This is because the INCL4.6 cannot treat the projectile breakup correctly, and therefore, the contribution of the deuteron breakup seems to be overestimated. Conversely, the JQMD underestimates the contribution of the deuteron breakup, and it underestimates the magnitudes of neutron spectra of all the targets except Ta. The JQMD successfully reproduces the neutron spectra for the Ta target because the contribution of deuteron breakup is much smaller than that of other targets.

The step-like structure was seen for the C target around 10 MeV. This structure corresponds to the transition to the ground state of the residual, which was reproduced by the DWBA calculation. The calculation overestimates this component. However, the unfolding method smooths the neutron spectra, as mentioned in Section 2.6.2. Thus, the inconsistency may be caused by the low-energy resolution of

Table 2.6: Natural abundance and Q-value of the (d,n) reaction of target materials.

element	nuclide	natural abundance [%]	Q-value [MeV]
$_{3}$Li	^{6}Li	7.5	3.38
	^{7}Li	92.5	15
$_{6}$C	^{12}C	98.9	-0.28
	^{13}C	1.1	5.33
$_{9}$F	^{19}F	100	10.6
$_{14}$Si	^{28}Si	92.23	0.524
	^{29}Si	4.67	3.37
	^{30}Si	3.1	5.07
$_{28}$Ni	^{58}Ni	68.1	1.19
	^{60}Ni	26.2	2.59
	^{61}Ni	1.14	3.63
	^{62}Ni	3.63	3.89
	^{64}Ni	0.93	5.23
$_{42}$Mo	^{92}Mo	14.8	1.86
	^{94}Mo	9.25	2.67
	^{95}Mo	15.9	3.18
	^{96}Mo	16.7	3.40
	^{97}Mo	9.55	3.95
	^{98}Mo	24.1	4.28
	^{100}Mo	9.63	5.22
$_{73}$Ta	^{181}Ta	99.988	4.88

unfolding rather than the overestimation by calculation.

The ADNYs of calculation results were derived in the same manner as in Section 2.6.2. Figure 2.21 shows the ADNYs for the C and LiF targets as a function of emission angles. The INCL4.6/GEM reproduces the forward-peaked distribution for both targets. The JQMD/GEM provides the flat distribution between emission angles from 0° to 30°. Because the deuteron breakup results in the forward-peaked neutron emission, the INCL4.6/GEM reproduces this tendency. The JQMD is unable to reproduce the deuteron breakup for this low-incident energy reaction, as shown in Fig. 2.20, and therefore, JQMD/GEM makes the flat distribution.

DEURACS

Theoretical calculations were performed using DEURACS [29], [42], [43], in which the (d,xn) reaction is described by some reaction processes: elastic breakup (EBU), non-elastic breakup (NBU), proton-transfer (p-TR), pre-equilibrium (PE), and

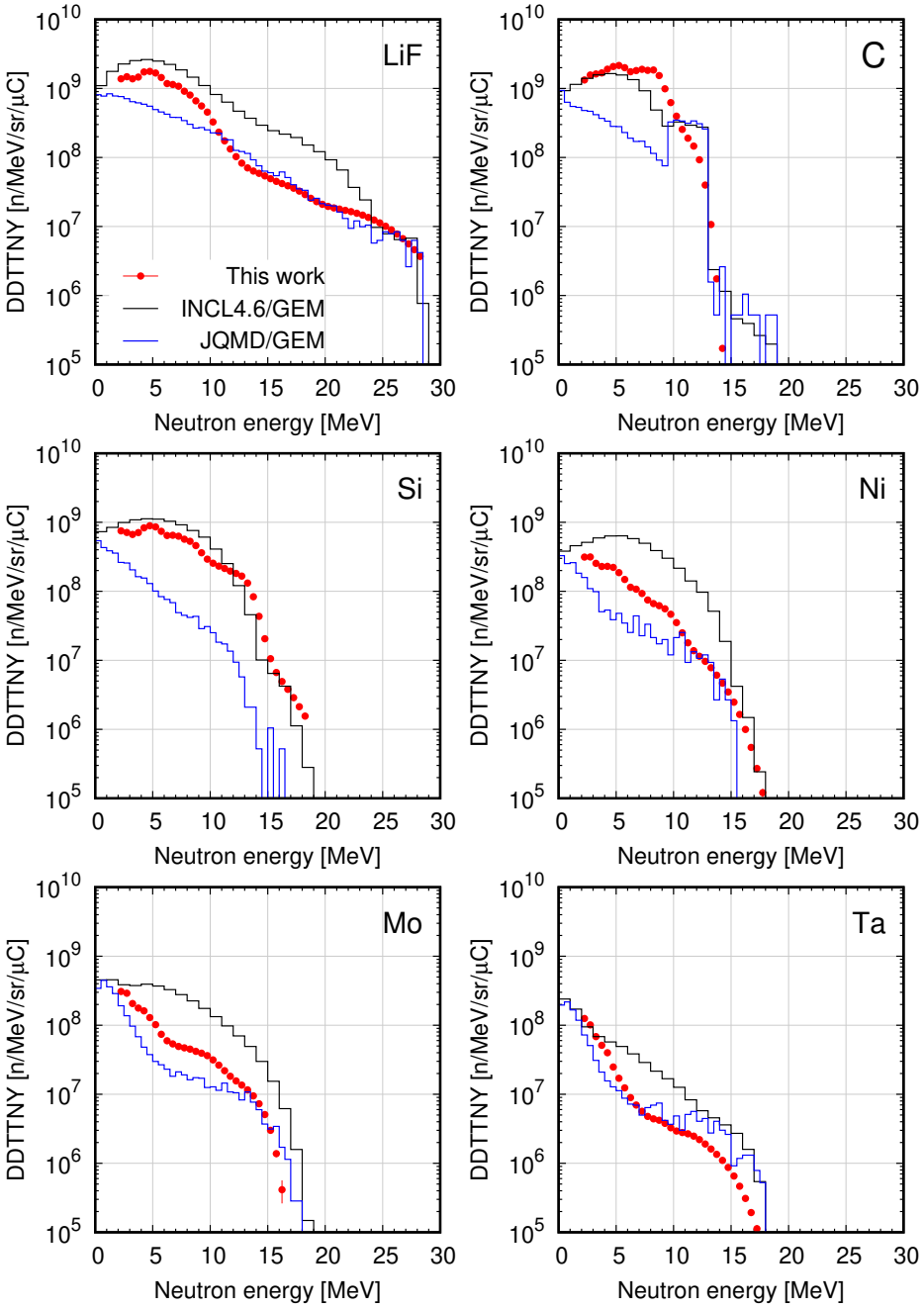

Figure 2.20: Experimental and calculated double-differential neutron spectra by bombarding 6.7-MeV/u deuterons at an emission angle of 0°. The calculation was performed using the INCL4.6/GEM (black) and JQMD/GEM (blue) models.

statistical decay (SD) processes. The EBU component was calculated using the CDCC [44]. The NBU and p-TR are proton stripping reactions to continuum and discrete levels, respectively. The former was calculated using the Glauber model [47], and the latter was calculated using the DWBA code DWUCK4 [73]. The PE and SD components were calculated using the CCONE code [48]. Note that the p-TR component was calculated only for ^{12}C(d,n)^{13}N$_{\mathrm{g.s.}}$ in this work.

DDTTNYs (d^2Y/(dEdΩ)) were calculated from DDXs (d$^2\sigma$/(dEdΩ)) with the following equation:

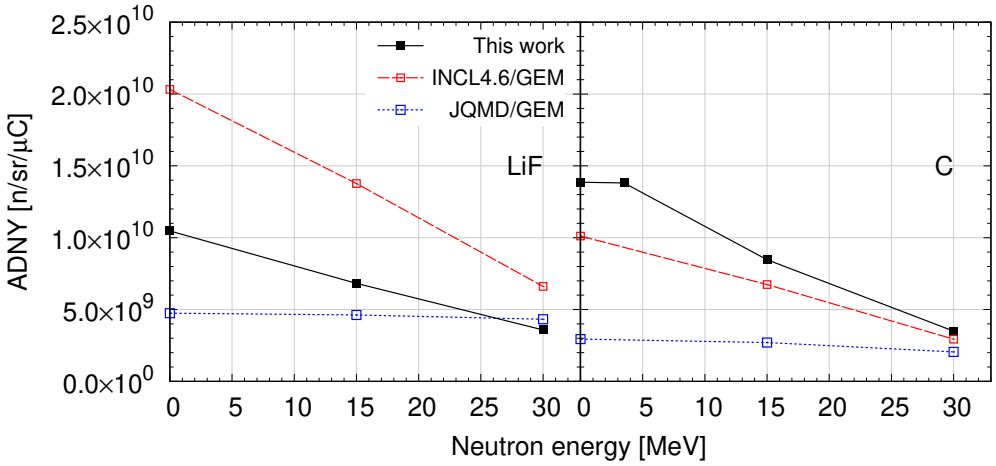

Figure 2.21: Angle-differential neutron spectra from the C target at emission angles of 0°, 15°, and 30°. The lines were drawn to guide the eyes.

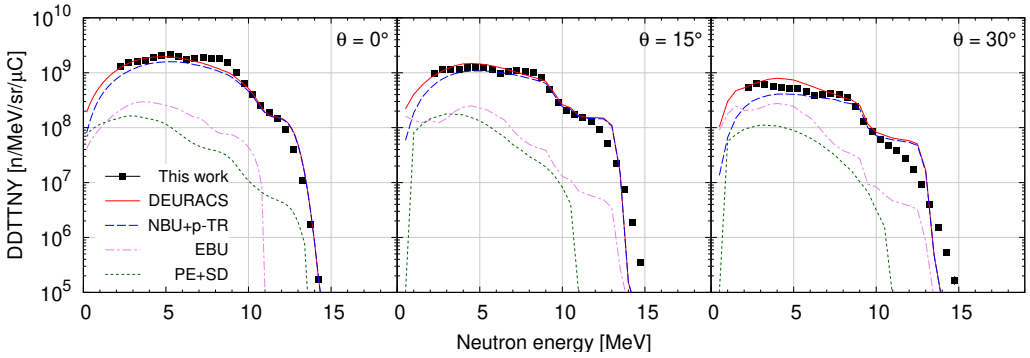

Figure 2.22: Double-differential neutron spectra from the C target at emission angles of 0°, 15°, and 30°. The lines denote each component: NBU+p-TR (blue dashed lines), EBU (violet dash-dotted lines), and PE+SD (green dotted lines). The red solid line denotes the sum of individual components.

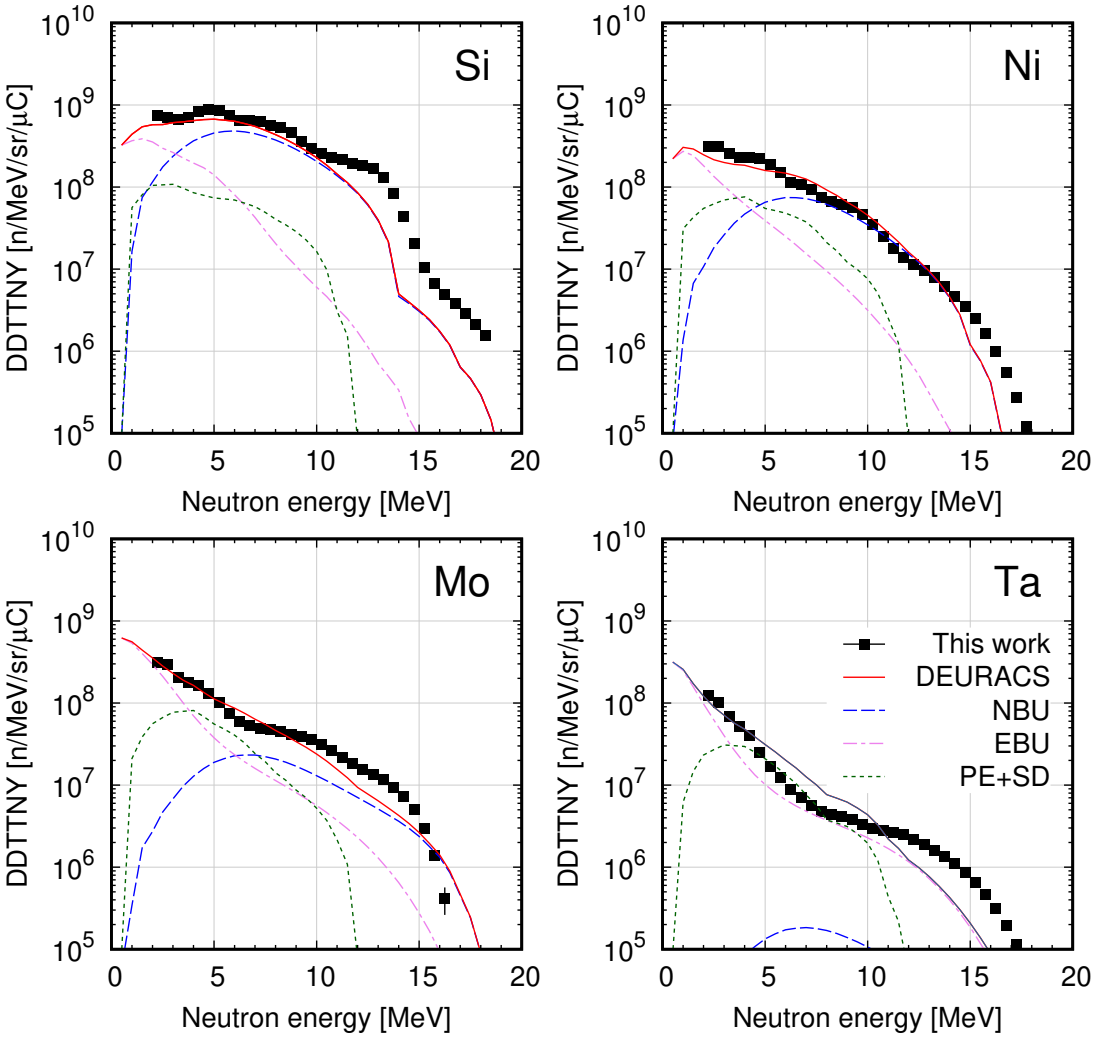

Figure 2.23: Double-differential neutron spectra from the Si, Ni, Mo, and Ta targets at an emission angle of 0°. The lines denote the calculation results by DEURACS, and the red line corresponds to the sum of individual components.

$$\frac{\mathrm{d}^2Y}{\mathrm{d}E\mathrm{d}\Omega}(E_{\mathrm{in}}) = \int_0^{E_{\mathrm{in}}} \mathrm{d}E_{\mathrm{d}} N \frac{\mathrm{d}^2\sigma}{\mathrm{d}E\mathrm{d}\Omega}(E_d) \left[\frac{\mathrm{d}E}{\mathrm{d}x}(E_d)\right]^{-1} D(E_d), \tag{2.38}$$

where E_{in} is the incident deuteron energy, N is the atomic density of the target, E_d is the deuteron energy at the target and $\mathrm{d}E/\mathrm{d}x$ is the deuteron stopping power. The natural abundance of the targets listed in Table 2.6 were considered by sum-

ming the DDTTNYs of each isotope weighted by their natural abundances. The attenuation rate of incident deuteron D is given by

$$D(E_d) = \exp\left[-\int_{E_d}^{E_{\rm in}} \mathrm{d}E' N\sigma_r(E') \left[\frac{\mathrm{d}E}{\mathrm{d}x}(E')\right]^{-1}\right], \tag{2.39}$$

where σ_r is the deuteron total reaction cross section. The DDXs were calculated in increments of 0.5 MeV of incident deuteron energy. Eq.(2.38) ignores neutron scattering in the target material. The probability of the neutron scattering was estimated to be less than 5%, so the effect was deemed negligible.

Figure 2.22 compares the measured and calculated DDTTNYs from the C target at emission angles 0°, 15°, and 30°. The DEURACS calculation assumed that the natural C target consisted of ^{12}C alone. Each component of NBU+p-TR (blue dashed lines), EBU (green dotted lines), PE+SD (violet dashed-dotted lines), and the summation of them (red solid lines) are shown. DEURACS successfully reproduced the measured neutron spectra. Further, the contribution of NBU+p-TR was predominant at forward emission angles $\leq$30° and decreased with increasing emission angle.

There were some discrepancies between the calculated and measured DDTTNYs. First, the shoulder observed at approximately 8.5 MeV at 0° was not reproduced well by DEURACS due to the absence of the DWBA calculation of the ^{12}C(d,n)^{13}N$_{\rm 1st}$ reaction in DEURACS, which is assessed to contribute to the formation of the shoulder. Second, the maximum emission energies were underestimated due to the lack of ^{13}C(d,n)^{14}N$_{\rm g.s.}$ reactions in the calculation. Finally, DEURACS overestimated the shoulder observed at approximately 12 MeV at emission angles of 15° and 30° in the experimental neutron spectra. The smoothing technique in the unfolding procedure could smear the step-like structure.

Figure 2.23 shows the DEURACS predictions for the Si, Ni, Mo, and Ta targets. The natural abundance of each target element was considered in the DEURACS calculation. DEURACS successfully reproduced the neutron spectra for all targets, and the EBU or NBU components seemed responsible for bumps in the spectra. For the Si target, DEURACS underestimated the experimental spectrum greater 11 MeV due to the absence of the DWBA calculation. For the Ta target, the EBU component was overestimated at approximately 7 MeV. This could be caused by the lack of a closed channel in the present CDCC calculation implemented in DEURACS as discussed in [74].

Figure 2.24 shows the ADNYs of each component calculated by DEURACS. DEURACS successfully reproduced ADNYs for a wide range of Z. The NBU component decreased more steeply with increasing Z than the other two components. In the low-energy incidence, the proton-stripping reaction was suppressed because the absorption of a proton in the deuteron was remarkably suppressed by strong

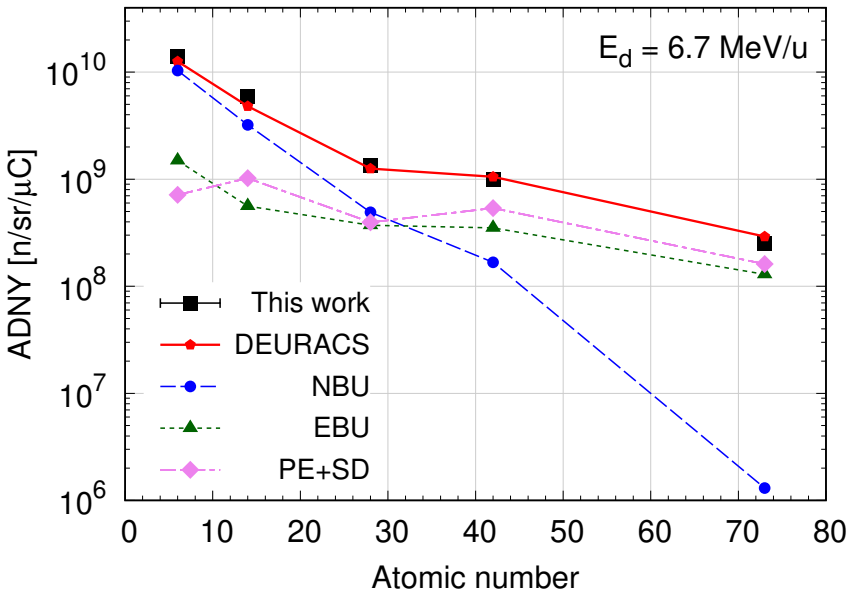

Figure 2.24: Angle-differential neutron yields by bombarding 6.7-MeV/u deuterons at an emission angle of 0°. The lines denote the calculation results by DEURACS, and the red line corresponds to the sum of individual components.

Coulomb repulsion between the proton and target nucleus [75], [76].

Calculation for (t, xn) Spectra

To validate the existing reaction models for triton-induced reactions, theoretical calculations were performed by INCL4.6/GEM, JQMD/GEM, TALYS, and CCONE. We used PHITS [24] for the INCL4.6/GEM and JQMD/GEM calculations.

The experimental and calculated DDTTNYs are compared in Fig. 2.25. The INCL4.6/GEM calculation considerably overestimated the neutron spectra for all targets, while the JQMD/GEM calculation generally agreed with the experimental spectra and underestimated neutron yields at approximately 6 MeV for the Si, Ni, and Mo targets. Because JQMD cannot treat the breakup of incident particles appropriately, the underestimation could be due to a lack of triton breakup.

The TALYS and CCONE calculations for DDTTNYs were performed using Eq.(2.38), in which the DDXs were calculated in increments of 0.5 MeV of incident triton energy. We used the default values as the model parameters used in the calculations. Both models roughly reproduced the experimental spectral shapes but underestimated the magnitude in the high-energy region.

The ADNYs for the triton incidence were derived by integrating DDTTNYs

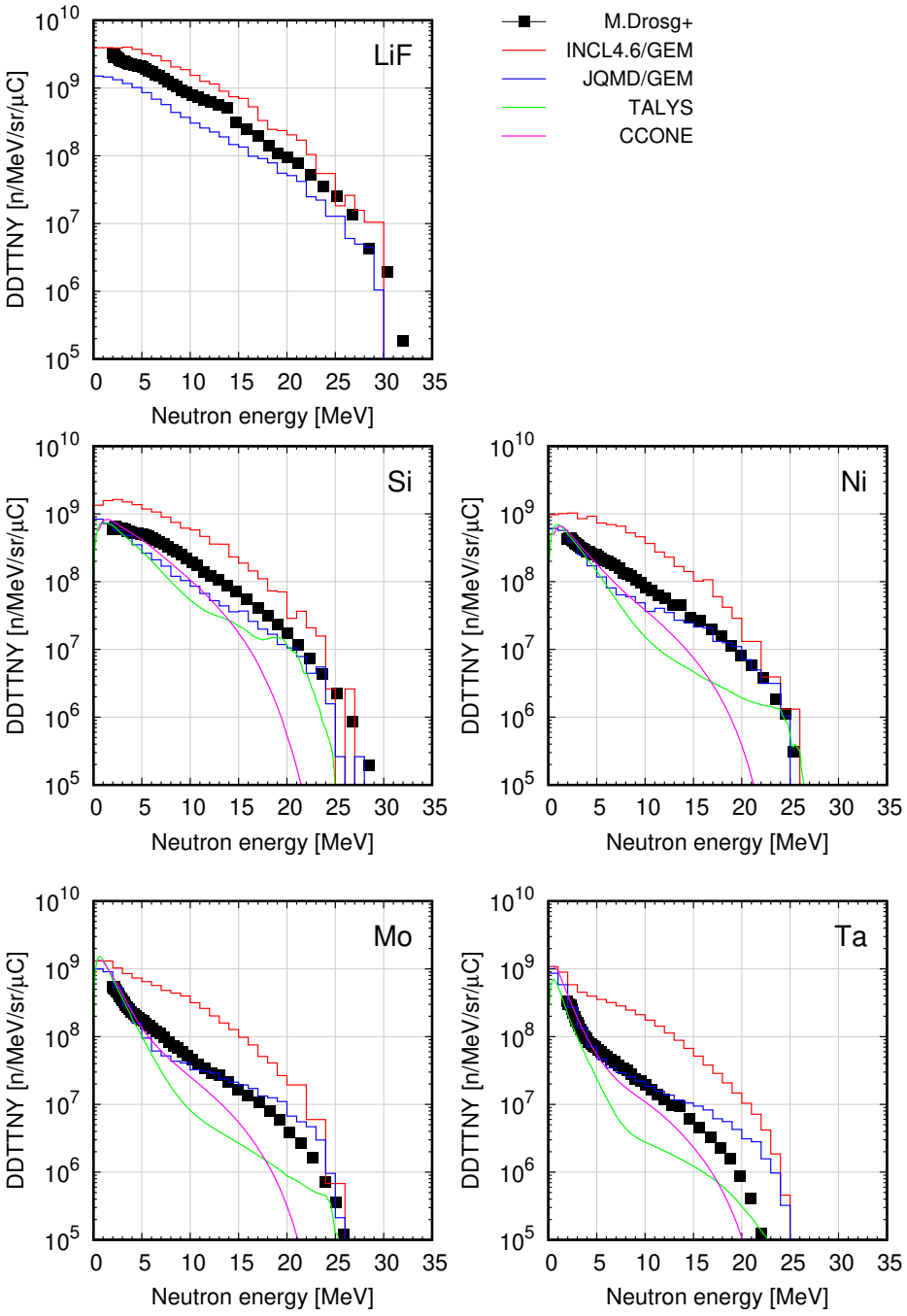

Figure 2.25: Double-differential neutron spectra by bombarding 6.7-MeV/u tritons at an emission angle of 0°. The experimental data is taken from Ref. [37].

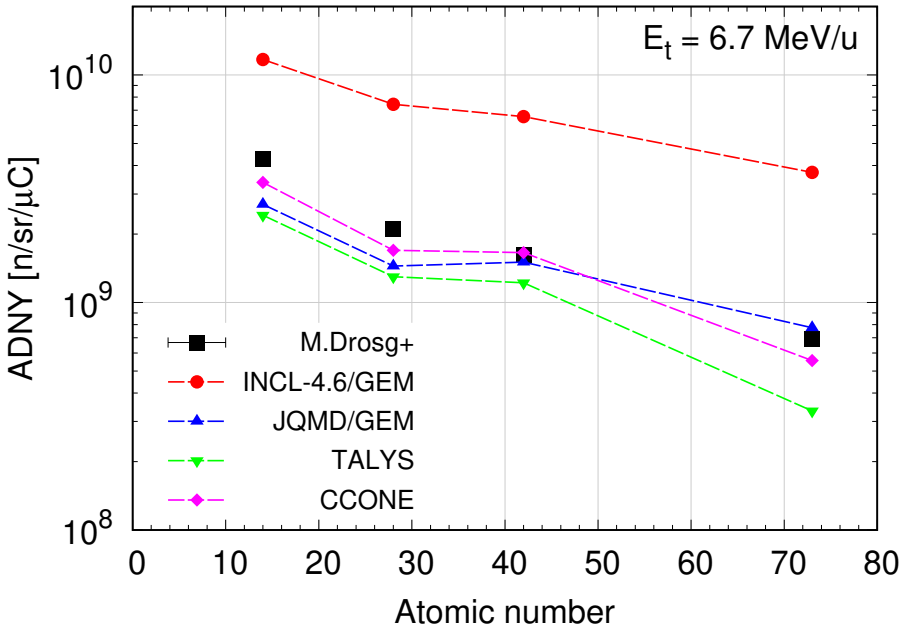

Figure 2.26: Angle-differential neutron yields by bombarding 6.7-MeV/u tritons at an emission angle of 0°. The experimental data is taken from Ref. [37].

over neutron energies ≥2 MeV. Fig. 2.26 shows the experimental and calculated ADNYs for the Si, Ni, Mo, and Ta targets as a function of atomic number Z. As shown, experimental and all calculated ADNYs decreased with increasing Z. Among the calculation models, JQMD/GEM and CCONE showed good agreement with experimental results.

2.7 Conclusions

Six materials (LiF, C, Si, Ni, Mo, and Ta) were bombarded with 6.7-MeV/u deuterons, and their DDTTNYs were measured. The measured neutron spectra at 0° were compared with the previous data of triton incidence at the same incident energy per nucleon. Some characteristic bumps were observed in the neutron spectra of the deuteron incidence, whereas no such structure was seen in those of the triton incidence. The angle-differential neutron yields at 0° were compared as well. We found that deuteron can yield more neutrons from low-Z targets than triton due to a large contribution from deuteron breakup, while the triton can yield more neutrons from high-Z targets.

A benchmark of some calculation codes was performed. For deuteron incidence, DEURACS successfully reproduced the neutron spectra for a wide Z target range.

DEURACS showed that deuteron breakup plays a significant role, especially for low-Z target materials, whereas EBU and SD processes were predominant for high-Z targets. For the triton incidence, JQMD/GEM and CCONE generally agreed with the experimental spectra. From these comparisons, the deuteron-induced reactions seem more suitable as neutron sources because the deuteron generates a more intense neutron beam than the triton at the same incident energy per nucleon whereas the deuteron generates less neutrons when bombarding structural materials. Moreover, the deuteron is stable, and its handling is much easier than the radioactive triton. From the benchmark of DEURACS with thick target neutron yield data measured over a wide range of target atomic number, we conclude that DEURACS is a promising calculation tool in developing basic nuclear data necessary for designing deuteron accelerator-based neutron sources.

3 Nuclide Production Cross Sections of ^{55}Mn, ^{59}Co, ^{nat}Ni, and ^{nat}Zr

3.1 Introduction

Reliable assessment of radioactivity in target and structural materials for high-energy accelerator facilities, such as spallation neutron sources and accelerator-driven transmutation systems (ADS) [77], requires detailed information on nuclide production cross sections induced by high-energy protons. Over many decades, a great deal of effort has been devoted to studying spallation reactions from both experimental and theoretical perspectives. In the 1990s, nuclide production cross sections induced by high-energy protons were measured for various target elements by some researchers [78]–[81]. In Ref. [78]–[80], benchmark analysis of some reaction models, e.g., HETC/KFA2 [82], LAHET [83], and CEM95 [84] were also performed in the proton energy range up to 2.6 GeV. They concluded that the reaction models used in their work could not reproduce the experimental data with sufficient accuracy, and further improvement of reaction models is required.

For these situations, the J-PARC group launched a research program focusing on the systematic measurements of proton-induced nuclide production cross sections for the material elements contained in the spallation target, proton beam window, etc. The measured data for Al, Fe, Pb, and Bi [85]–[87] showed that the experimental uncertainties were reduced due to the stable proton beam irradiation and the well-established beam-profile monitoring system.

This work was conducted as part of the J-PARC program. The elements of Mn, Co, Ni, and Zr were chosen as target materials, which are widely used as constituent elements of structural materials of spallation neutron sources and the insert matrix of the ADS minor actinide fuel. Benchmarks of the following spallation reaction models were performed: INCL4.6/GEM, Bertini/GEM, and Jet A A microscopic model (JAM)/GEM, which are implemented in PHITS3.10, and another reaction model INCL++ [88] combined with ABLA07 code [89] (INCL++/ABLA07). In addition, the benchmark of evaluated nuclear data library JENDL/HE-2007 [35], which is only available for proton energies up to 3.0 GeV, was performed.

3.2 Reaction Models

The spallation reaction is well described by a two-step process, comprising the formation of prefragments via the intra-nuclear cascade process and the de-excitation process of the prefragments by the evaporation of light particles. The PHITS code [24] possess some intra-nuclear cascade models, e.g., INCL4.6 [55], Bertini [90], and JAM [91] for the proton-induced reaction, and GEM [57] as the subsequent evaporation process. Recently, CEA group [58] converted INCL, which was originally developed in FORTRAN, to C++ version (denoted as INCL++) and made some improvements [33]. The benchmark of these models has not been sufficiently performed.

3.3 Experiment

3.3.1 Activation Method

Nuclide production cross sections were measured using a conventional activation method. First, some pure element foils are irradiated by high-energy projectile. After irradiation, the decay γ-rays emitted from the reaction products are measured using a γ-ray detector with high-energy resolution such as lithium-doped germanium and high-purity germanium (HPGe) detectors. Because the γ-ray has a unique energy corresponding to the excitation energy of the daughter nucleus, one can derive the number of reaction products by investigating the measured γ-ray spectra.

3.3.2 J-PARC

The experiment was conducted at J-PARC, which is located at Ibaraki prefecture in Japan. Figure 3.1 shows the entire view of the J-PARC. The J-PARC is a multi-purpose experimental facility with a 1-MW class proton beam power. The facility consists of three major accelerators: the Linac, 3 GeV Rapid Cycling Synchrotron (RCS), and 50 GeV Main Ring (MR). A negative hydrogen ion (H^-) beam is accelerated up to 400 MeV by the Linac, and injected into the RCS. At the RCS injection point, the H^- beam is converted into the proton (H^+) beam using charge stripping foils. The accelerated 3-GeV proton beam is simultaneously delivered to the Material and Life Science Experimental Facility (MLF) as well as to the MR. In the MLF, the proton beam bombard the muon and neutron targets consisting of

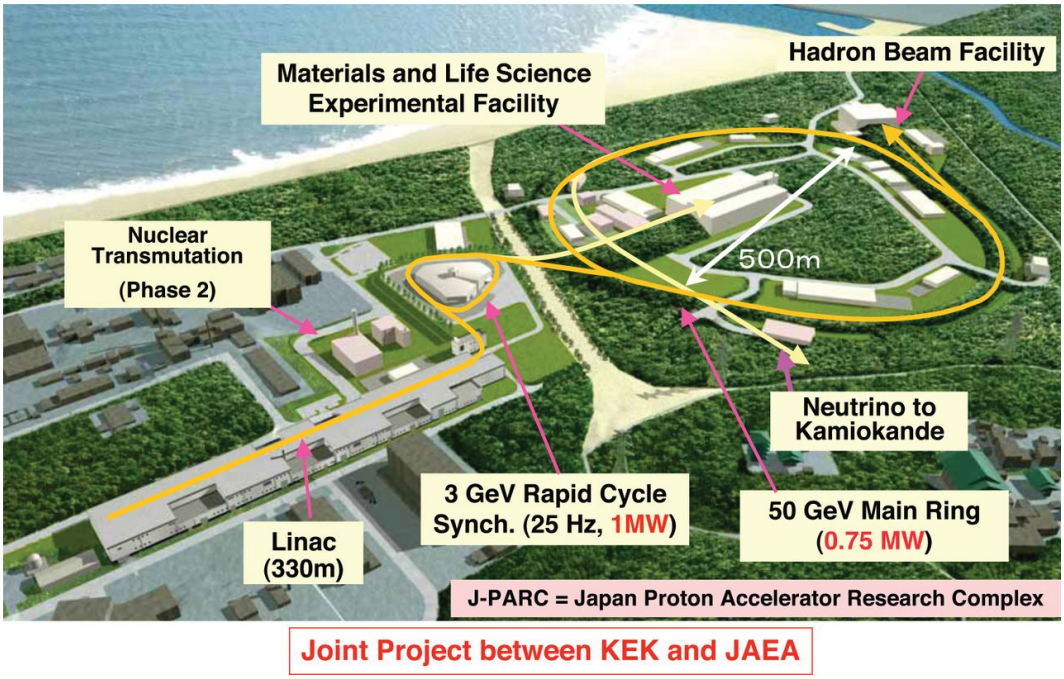

Figure 3.1: Bird's-eye view of the Japan Proton Accelerator Research Complex (J-PARC). The picture is taken from Ref. [92].

carbon and mercury, respectively. After accelerated by the MR, the proton beam is used in the hadron and neutrino experimental facilities.

3.3.3 Irradiation

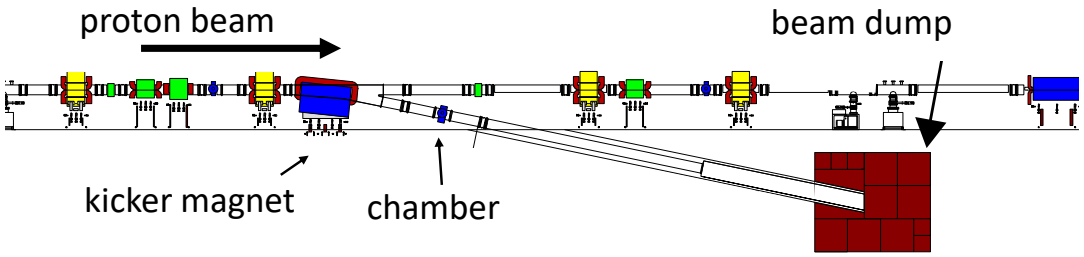

Figure 3.2: Schematic drawing of the irradiation system. Sample foils were set in the vacuum chamber.

Two irradiation experiments were performed at a beam dump [93], [94] near the beam extraction from the RCS. Both experiments were performed in the same experimental setup, as shown in Fig. 3.2 The irradiation targets were set in the

vacuum chamber installed in the beam line. The irradiation targets were assembled in three or four sets of stacked foils. The cross-sectional drawing of the stacked foils is drawn in Fig. 3.3. In each stack, the sample foils were stacked with increasing the atomic number. High-purity element foils of Mn (760 mg/cm^2, 99.95%), Co (110 mg/cm^2, 99.99+%), Ni (90 mg/cm^2, 99%), and Zr (80 mg/cm^2, 99.2%) were supplied by Goodfellow Cambridge Ltd. The cross section data for the other foils of Cr (600 mg/cm^2), Ag (130 mg/cm^2), and Ta (170 mg/cm^2) are to be published. Al foils (0.1-mm-thick) were inserted between the target foils to prevent light product nuclides from entering the neighboring targets. All the stacked foils were enclosed in 0.1-mm-thick Al containers as shown in (c) of Fig. 3.3, and fixed on movable stages. The sample foils were inserted to the irradiation position for the respective proton energies to fix the irradiation conditions.

Irradiation was performed at 1.3, 2.2, and 3.0 GeV for the Mn and Co targets, and 0.4, 1.3, 2.2, and 3.0 GeV for the Ni and Zr targets. The proton beam was accelerated up to 0.4 GeV by the LINAC. The 0.4-GeV proton beam was extracted without acceleration by the RCS. The 1.3- 2.2-, and 3.0-GeV proton beams were delivered from the RCS acceleration by changing the extraction timing of the kicker magnet. Before proton irradiation, the proton-beam profile was monitored by a multi-wire profile monitor [95], which was placed in the beam transport line, and the beam position was adjusted to irradiate the center of the sample foil. The number of protons irradiated onto the sample was monitored using an integrating current transformer (Bergoz instrumentation, ICT-300-070-50:1-LD-H) [96]. The proton beam had an approximate Gaussian shape with full width at half maximum (FWHM) of 11 mm in the radial direction. As described in subsection 3.4.1, the beam profile under each irradiation was accurately determined by the measurement of the spatial activation distribution in the sample foil. The proton beam intensity was 6.7×10^{12} protons per pulse, with a repetition rate of 0.4 Hz. For each energy value, the irradiation time was approximately 100 s, which corresponds to 40 pulses of proton beam irradiation.

3.3.4 Measurement of Decay γ-rays

After proton irradiation, decay γ-rays from the irradiated samples were detected by two HPGe detectors (CANBERRA GC2018). The γ-ray measurement was periodically performed at different intervals as listed in Table 3.1 to obtain the decay curves for products of interest. The sample foil was mounted on an acrylic spacer, which was placed between the sample and the detector to maintain a constant sample-to-detector distance during the γ-ray measurement. The distance between the sample position and the HPGe head was selected to be 5 or 25 cm. The 25-cm acrylic spacer was used to reduce the counting rate, resulting in a small dead time correction. Figure 3.4 shows a typical γ-ray spectrum of the Co target

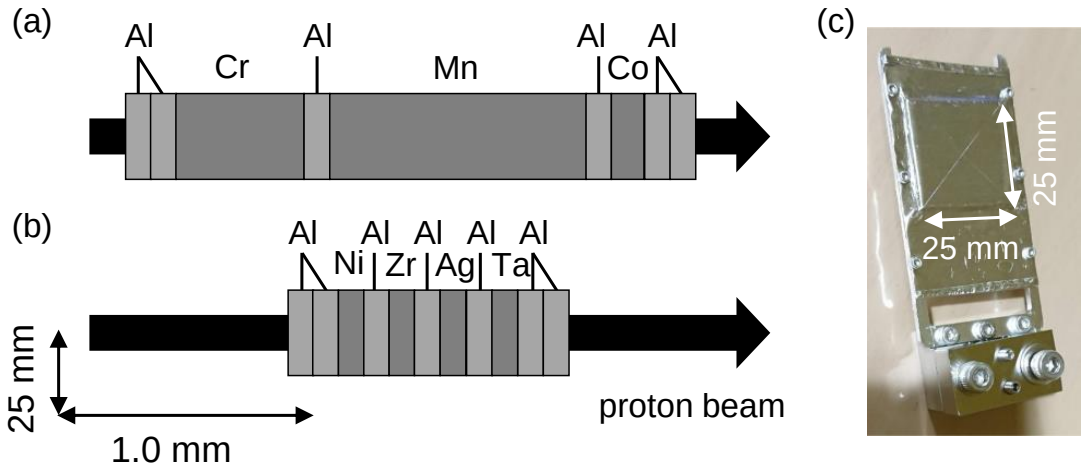

Figure 3.3: Cross-sectional view of the stacked samples used for (a) Mn and Co, (b) Ni and Zr irradiations, and (c) photography of the stack sample. The vertical and horizontal scales are displayed in the lower left-hand corner.

measured at the second cycle of 3-GeV proton irradiation. The energy resolution was good enough to identify each product (1.87 keV of full width at half maximum for the 1332 keV γ-ray of ^{60}Co).

Table 3.1: Typical cooling time (t_c) and γ-ray measurement time (t_m) used for the analysis.

Cycle		1	2	3	4	5	6	7	8
Mn	t_c [h]	6.5	11	13	30	95	263	959	3384
	t_m [h]	0.17	0.25	2.0	8.0	24	72	168	168
Co	t_c [h]	5.9	10	11	21	71	191	766	3215
	t_m [h]	0.17	0.25	2.0	9.0	24	72	193	169
Ni	t_c [h]	10	26	79	240	720	2665	—	—
	t_m [h]	0.5	2.0	8.0	24	59	168	—	—
Zr	t_c [h]	9.2	22	63	192	600	2304	6864	—
	t_m [h]	0.5	1.9	8.0	24	59	192	111895	—

3.3.5 Calibration of Detector Efficiency

The peak efficiency of the HPGe detector was calibrated using the standard γ-ray sources listed in Table 3.2. The relative uncertainty of activity was 2.5% for all the radioactive sources. Sufficient measurement time resulted in a statistical uncertainty of peak counts <1%. The coincidence-summing effect was considered

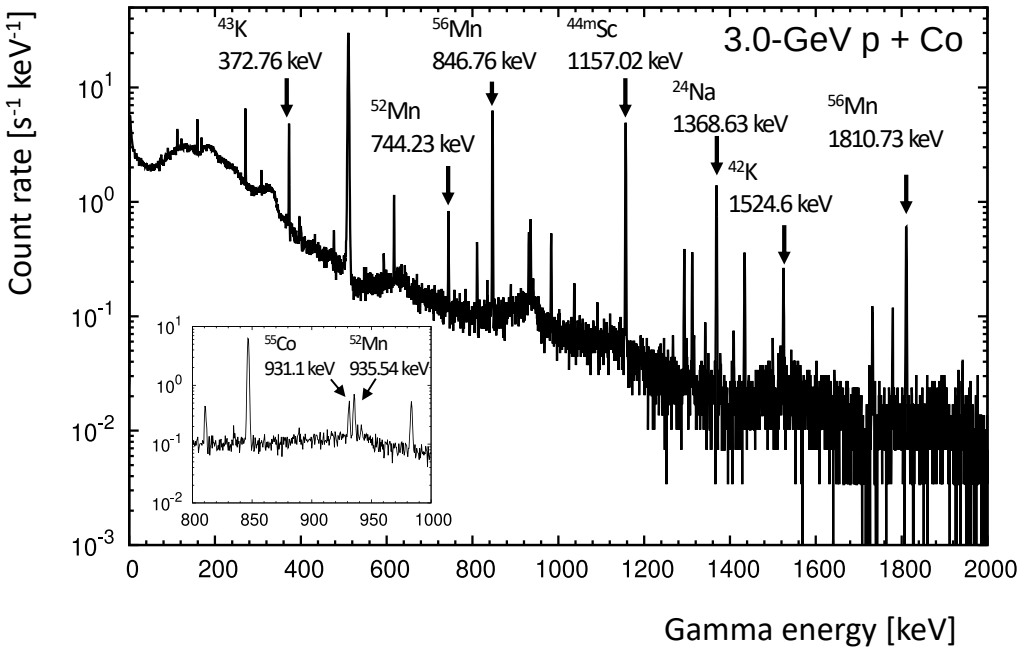

Figure 3.4: Gamma spectrum obtained for the Co target irradiated with 3.0-GeV protons.

using the correction factor (F^S) given in Table 1 of Ref. [97]. The total efficiency (ε_T) was required to obtain the F^S. However, the total efficiency could not be derived by the γ-ray sources used in this work. Thus, an empirical peak-to-total ratio ($\varepsilon_P/\varepsilon_T$) was used. According to Ref. [98], the peak-to-total ratio is expressed by

$$\varepsilon_P/\varepsilon_T = \alpha \ln \varepsilon_r + \beta, \tag{3.1}$$

where, ε_r is the relative efficiency to the NaI detector, and α and β are calculated by

$$\begin{aligned} \alpha &= \exp\left[-1.11 - 0.30 \ln E_\gamma\right] \\ \beta &= \exp\left[-7.97 + 3.31 \ln E_\gamma - 0.383 (\ln E_\gamma)^2\right], \end{aligned} \tag{3.2}$$

where E_γ is the γ-ray energy in the unit of keV.

Figure 3.5 shows the measured detection efficiencies with 5- (closed squares) and 25-cm (closed circles) acrylic spacers. The peak efficiency $\varepsilon_p(E_\gamma)$ for the γ-ray energy (E_γ) was fitted by the following formula:

$$\ln \varepsilon_p(E_\gamma) = \begin{cases} a_0 + a_1 \ln E_\gamma + a_2 (\ln E_\gamma)^2 & \text{for} \quad E_\gamma < E_{\text{knee}} \\ b_0 + b_1 \ln E_\gamma + b_2 (\ln E_\gamma)^2 & \text{for} \quad E_\gamma \geq E_{\text{knee}}, \end{cases} \tag{3.3}$$

where a_0, a_1, a_2, b_0, b_1, b_2, and E_{knee} are the fitting parameters. The fitting curve was smoothly connected at the knee point, E_{knee}.

Table 3.2: Energy and gamma intensity of the standard γ-ray sources used for the calibration of detection efficiencies.

Nuclide	Energy [keV]	Intensity [%]
^{241}Am	59.54	35.9
^{152}Eu	121.78	28.53
	244.7	7.55
	344.28	26.59
	443.96	2.83
	778.90	12.93
	964.06	14.51
	1408.01	20.87
^{137}Cs	661.66	85.1
^{60}Co	1173.23	99.85
	1332.49	99.98

3.4 Data Analysis

3.4.1 Derivation of Production Cross Sections

The production cross sections were derived from the γ-ray measurements of the irradiated samples by the following procedure. In this work, cross sections for product nuclides with half-lives ranging from 1.8 h to 2.6 yr were derived. Since the duration of sample irradiation ($\sim$ 100 s) was much shorter than the half-lives, the decay of the product nuclides during the irradiation could be neglected. Thus, the activity of reaction product A at cooling time t is simply expressed by

$$A(t) = \lambda N_0 e^{-\lambda t}, \tag{3.4}$$

where λ is the decay constant of the product nuclide and N_0 is the number of the product nuclides of interest at $t = 0$. If the half-life of the product nuclide is comparable to that of the precursor nuclide, the activity is expressed by

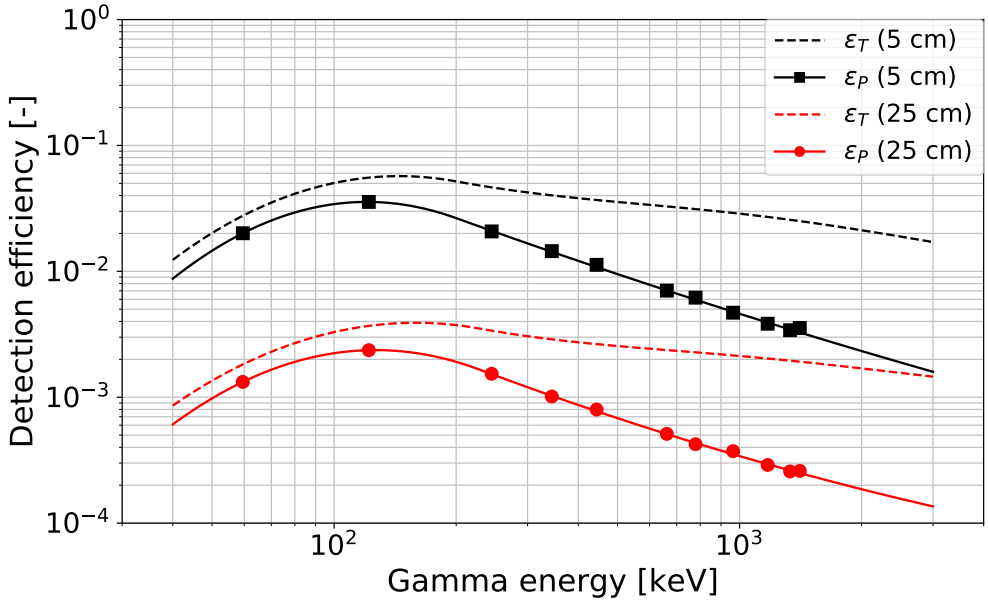

Figure 3.5: Measured and fitted peak-detection efficiencies with the 5- (black square) and 25-cm (red circle) acrylic spacers. Total efficiency was calculated using peak-to-total ratio [98].

$$A(t) = \lambda \left[N_0 e^{-\lambda t} + N_0^p \frac{\nu \lambda^p}{\lambda^p - \lambda} (e^{-\lambda t} - e^{-\lambda^p t}) \right], \tag{3.5}$$

where ν is the decay probability of the precursor into the daughter, λ^p and N_0^p are the decay constant and the number of products of the precursor nuclide, respectively. In this work, Eq.(3.5) was applied only to the decay chain of ^{44m}Sc $\rightarrow$ ^{44g}Sc.

The number of photo-peak counts obtained by the γ-ray measurement, $C(t, t_m)$, is related to the activity, $A(t)$, by the following formula:

$$C(t, t_m) = I_\gamma \varepsilon_p \int_t^{t+t_m} A(t) \mathrm{d}t, \tag{3.6}$$

where t_m is the measurement interval, I_γ is the gamma intensity of the product nuclides, and ε_p is the peak efficiency of the HPGe detector. The number of products at $t = 0$, i.e., N_0 and N_0^p in Eqs.(3.4) and (3.5), were derived by the least-squares method. The chi-square value was defined by

$$\chi^2 = \sum_{i=1}^{L} \left[\frac{C(t_i, t_{m,i}) - I_\gamma \varepsilon_p \int_{t_i}^{t_i + t_{m,i}} A(t) dt}{\Delta C(t_i, t_{m,i})} \right]^2, \tag{3.7}$$

where L is the number of measurement points used for the fitting, $\Delta C(t_i, t_{m,i}) = \sqrt{C(t_i, t_{m,i})}$ is the statistical uncertainty of the peak counts, t_i and $t_{m,i}$ are the cooling time and measurement interval of the i-th measurement, respectively. Figure 3.6 shows the typical fitting results. The fitting was performed only for the measurement points with relatively small statistical uncertainties.

Finally, the nuclide production cross section σ was obtained by

$$\sigma = \frac{f_{\mathrm{abs}} f_{\mathrm{sec}} f_{\mathrm{esc}} N_0}{n f_{\mathrm{beam}} N_{\mathrm{proton}}}, \tag{3.8}$$

where n is the areal number density of the target nuclei in the sample foil, and N_{proton} is the number of protons irradiated on the sample. The correction factors, f_{beam}, f_{abs}, f_{sec}, and f_{esc}, are related to the number of protons actually bombarding the samples, attenuation of γ-rays by self-absorption in the sample foils, contribution to nuclide production by the secondary particles, and incoming and escape of light products, respectively. Each correction method is described in the following subsections.

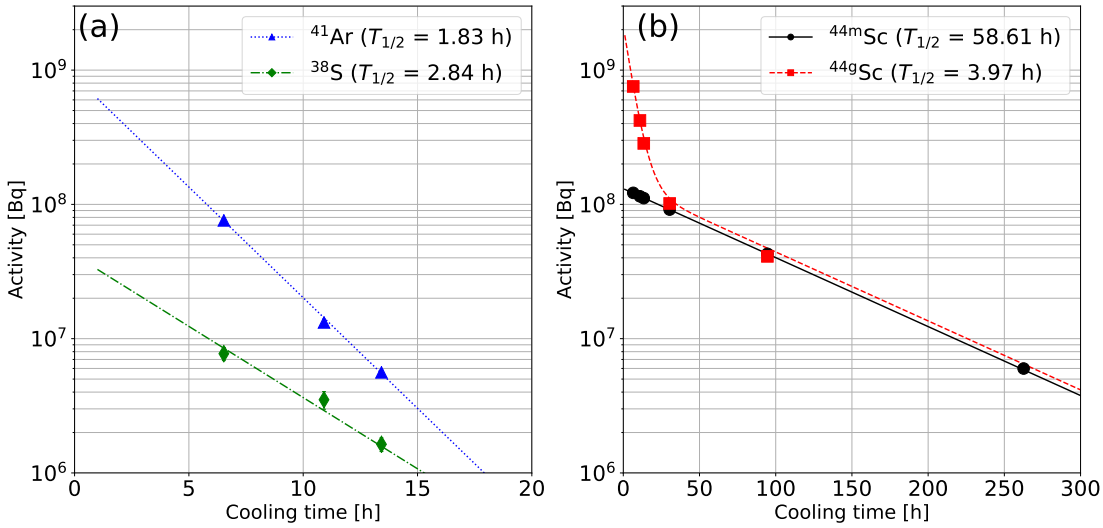

Figure 3.6: Decay curves of (a) ^{41}Ar and ^{38}S and (b) ^{44m}Sc and ^{44m}Sc $\rightarrow$ ^{44g}Sc for the Co target. Equation (3.5) was used only to fit the decay chain of ^{44m}Sc $\rightarrow$ ^{44g}Sc. The decay curves of the other reaction products were fitted using Eq.(3.4).

Proton number determination

The number of protons irradiated on the sample foil was corrected using the spatial activation distribution in the sample foil measured using an imaging plate (Fuji-FILM, BAS-SR2040). The detail of this method is described in Ref. [85]. Here, the

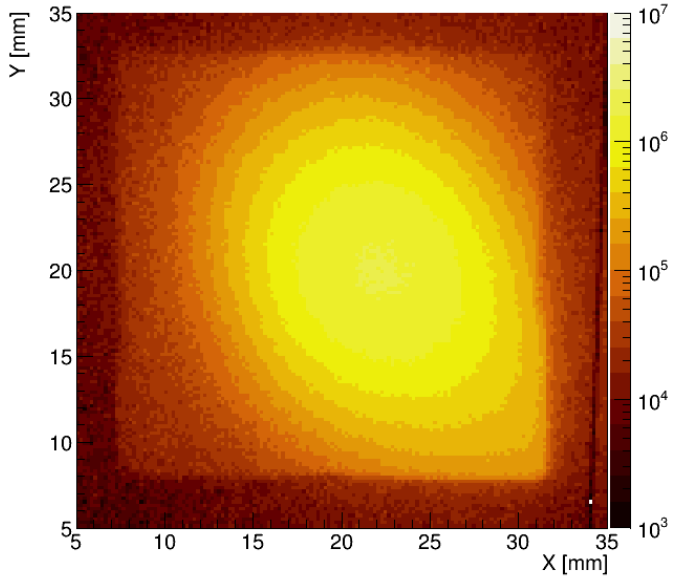

Figure 3.7: Spatial activation distribution measured by an imaging plate. The square indicates the foil area.

spatial activation distribution was assumed to identical to the proton-beam profile. The activation distribution was fitted by a two-dimensional Gaussian function given below:

$$f(x,y) = \frac{N}{2\pi\sigma_x\sigma_y\sqrt{1-r^2}}\exp\left[-\frac{1}{2(1-r^2)}\left\{\frac{(x-\mu_x)^2}{\sigma_x^2}+\frac{(y-\mu_y)^2}{\sigma_y^2} - \frac{2r(x-\mu_x)(y-\mu_y)}{\sigma_x\sigma_y}\right\}\right], \tag{3.9}$$

where N, σ_x, σ_y, μ_x, μ_y, and r are fitting parameters, and N satisfies $N = \int_{-\infty}^{\infty}\int_{-\infty}^{\infty} f(x,y)dxdy$. Using Eq.(3.9), the ratio of the number of protons actually bombarding the sample foils was determined by

$$f_{\mathrm{beam}} = \frac{1}{N}\int_{\mathrm{foil}} f(x,y)\mathrm{d}x\mathrm{d}y, \tag{3.10}$$

where the integration is applied over the target foil area. Table 3.3 summarizes the correction factors, f_{beam}, derived for each target foil.

Table 3.3: Correction factors (f_{beam}) of the sample foils.

	$E_p = 0.4$ GeV	$E_p = 1.3$ GeV	$E_p = 2.2$ GeV	$E_p = 3.0$ GeV
Mn	—	0.966	0.979	0.966
Co	—	0.980	0.984	0.974
Ni	0.990	0.993	0.995	0.974
Zr	0.990	0.993	0.995	0.974

Self-absorption

The self-absorption of γ-rays in the sample foils was also corrected. The correction factor was calculated using the formula,

$$f_{\mathrm{abs}}(E_\gamma) = \frac{\mu(E_\gamma)\rho d}{1 - e^{-\mu(E_\gamma)\rho d}}, \tag{3.11}$$

where $\mu(E_\gamma)$ is the mass absorption coefficient for the γ-ray energy (E_γ), ρ is the mass density of the sample foil, and d is the target thickness. The mass absorption coefficients were taken from the NIST-XCOM database [99]. The correction factor f_{abs} varied depending on the E_γ as shown in Fig. 3.8, ranging from 1.0 to 1.28.

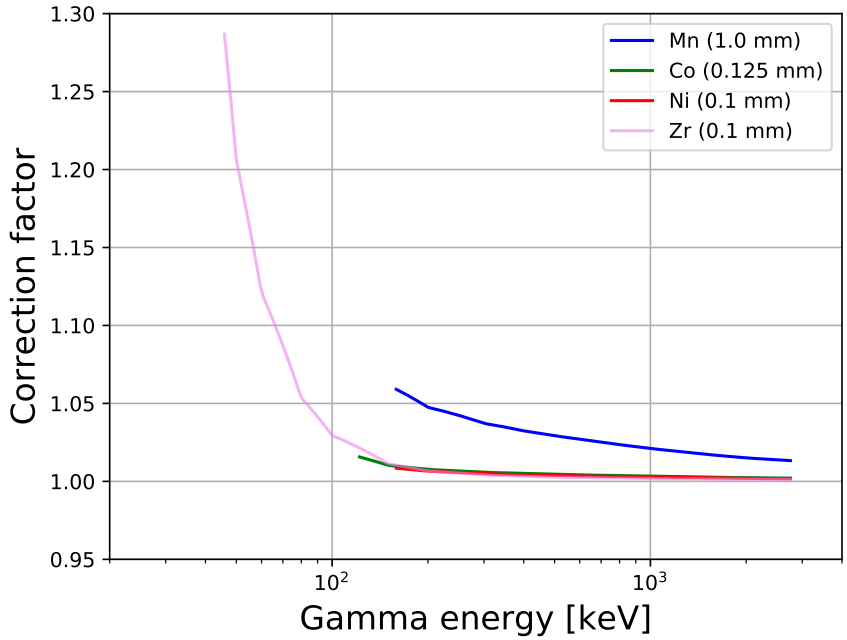

Figure 3.8: Correction factor for the self-absorption (f_{abs}) used in the analysis.

Secondary particles

Contributions of the secondary particles generated in the sample target to the nuclide productions were estimated by particle transport simulation using PHITS version 3.10 (PHITS3.10) [24]. The simulation was performed with the actual geometrical configuration of the irradiated target sample and the default parameter sets of the physical models in PHITS3.10. Figure 3.9 shows the simulated fluxes of the secondary particles produced by the primary 3.0-GeV proton beam irradiation. The contribution of secondary protons and neutrons was considered because these fluxes are much larger than the other secondary light ions, such as deuterons, tritons, and α-particles. The contributions of the primary and secondary protons and secondary neutrons to the nuclide production were calculated with the Liège intra-nuclear cascade model version 4.6 (INCL4.6) [55] coupled with the generalized evaporation model (GEM), except for the production by neutrons with energy $\leq$20 MeV, where the nuclide production cross sections were obtained from the JENDL-4.0 nuclear data library [100], [101]. In the simulation, the numbers of nuclides produced by primary protons (N_{primary}) and secondary particles ($N_{\mathrm{secondary}}$) were tallied. The correction factor was defined by $f_{\mathrm{sec}} = N_{\mathrm{primary}}/(N_{\mathrm{primary}} + N_{\mathrm{secondary}})$ for the correction of each reaction product. The correction factor (f_{sec}) varied from 0.372 to 1.0. Notably, a f_{sec} value of $<$0.9 is adopted for the following heavy products: ^{54}Mn from Mn and ^{54}Mn, ^{52}Fe, ^{56}Co, ^{57}Co, ^{58}Co, and ^{57}Ni from the Co target, and $^{92\mathrm{m}}$Nb from the Zr target.

Incoming and escape of reaction products

In the sample stack, Al foils were inserted to prevent the reaction products in the sample foil from escaping to the neighboring sample foils, as shown in Fig. 3.3. However, light products, such as ^{7}Be, ^{22}Na, and ^{24}Na, generated in the Al foil and other target foils may escape to the neighboring foils. To consider the effects of the incoming and escape of the light products, the particle transport of the products, including ^{7}Be, ^{22}Na, and ^{24}Na was simulated by the PHITS3.10 with the same sample stack geometry as in the measurement. The simulation tallied the total number of products of interest generated in the target foil, N_{pro}, and the number of products that finally stopped in the target foil by ion transport, N_{stop}, which include the products generated in the target and neighboring Al foils. The correction factor for the light products was defined by $f_{\mathrm{esc}} = N_{\mathrm{pro}}/N_{\mathrm{stop}}$. The correction was applied to only the ^{7}Be production because the corrections for the products heavier than ^{7}Be, i.e., ^{22}Na and ^{24}Na, were negligible (less than 1%). The result is listed in Table 3.4. In contrast, the corrections for the Mn target were negligible because the Mn sample was much thicker than the other samples.

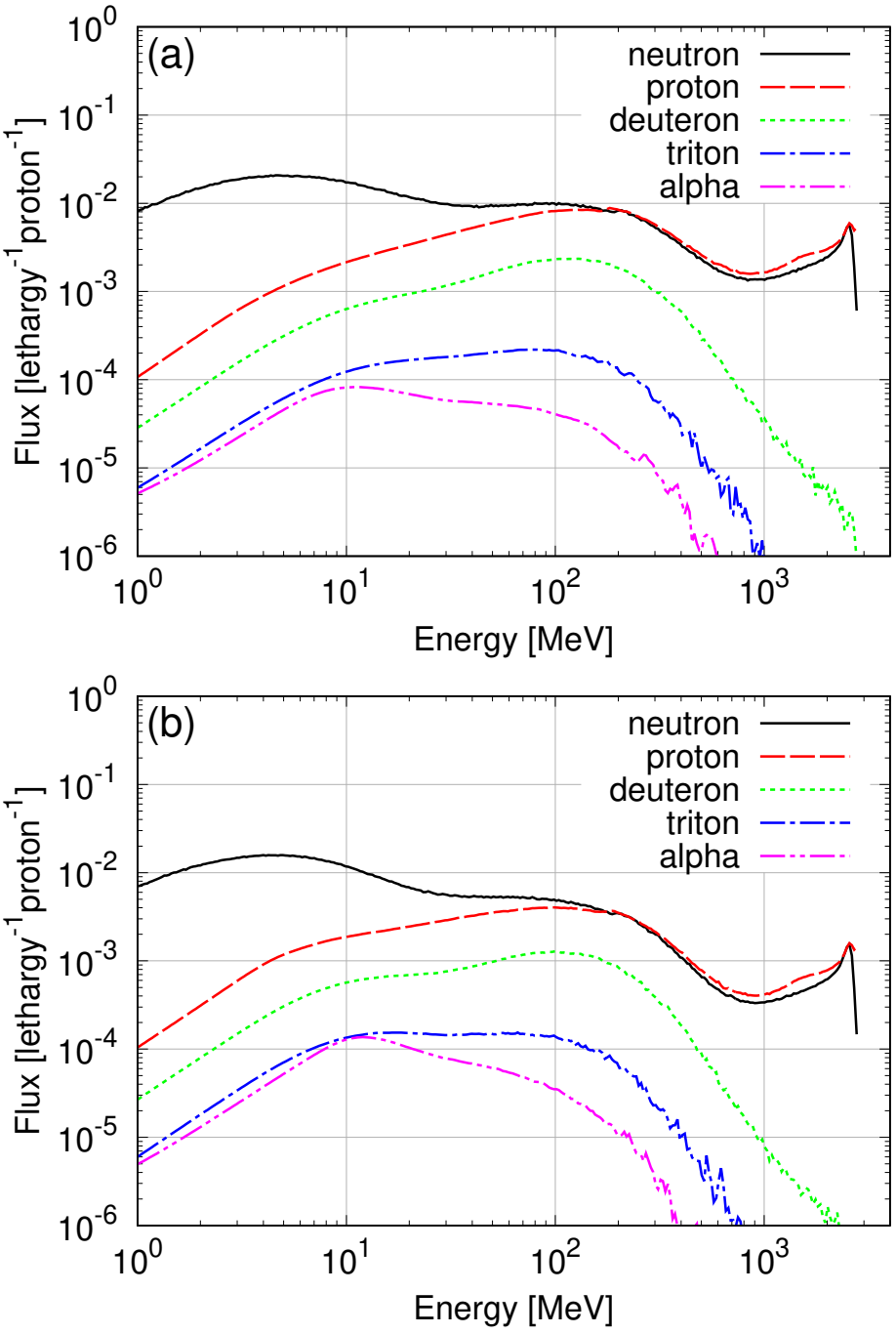

Figure 3.9: Calculated fluxes of the secondary protons, neutrons, deuterons, tritons, and α-particles in the (a) Mn and (b) Zr targets bombarded with 3.0-GeV protons.

Table 3.4: Correction factors (f_{beam}) of the sample foils.

	$E_p = 0.4$ GeV	$E_p = 1.3$ GeV	$E_p = 2.2$ GeV	$E_p = 3.0$ GeV
Mn	—	—	—	—
Co	—	0.966	0.953	0.968
Ni	0.935	0.970	0.994	0.998
Zr	0.634	0.809	0.892	0.892

3.4.2 Uncertainties

The following sources of uncertainty were considered and included in the total uncertainties of the measured production cross sections.

(1) Uniformity of target foil thickness: The target thickness was measured using a digital micrometer at nine different points on each sample foil. The standard deviation of the thickness was <3.3%.

(2) Nuclide production from the impurities contained in the target foils: The contribution of the products produced from the impurities was considered. Because the contributions of impurities for Mn, Co, Zr were considerably small, this uncertainty was considered only for the Ni target by the following procedure: The cross section for the measured (including impurities) σ_{meas} is related with the true (without impurities) cross section σ_{true} by

$$\sigma_{\mathrm{meas}} = p_{\mathrm{Ni}}\sigma_{\mathrm{true}} + \sum_i f_i\sigma_i, \tag{3.12}$$

where $p_{\mathrm{Ni}} = 0.99$ represents the purity of the Ni target and f_i denotes the fraction of i-th impurities contained in the Ni foil. Because the maxima of the impurity fractions are only available as shown in Table 3.5, the uncertainty caused by the impurities were estimated as $|1 - \sigma_{\mathrm{true}}/\sigma_{\mathrm{meas}}|$.

(3) Statistical uncertainties of the γ-ray measurements: The statistical uncertainty of the photo-peak counts was considered using the error propagation law.

(4) Proton number determination: The number of protons was measured by the integrating current transformer, and the uncertainty was 2%.

(5) Detector efficiency: The uncertainty of the standard γ-ray source activity was considered using the error propagation law. The uncertainty varied from 1.0% to 7.0% depending on the γ-ray energy.

(6) Dead-time and pile-up losses in γ-ray measurements: The dead time correction was accomplished using the ratio of real-time to live-time of the HPGe detector. The dead time was maintained below 14% by adjusting the foil-to-detector distance, and the uncertainty arising from this correction was neglected.

(7) Nuclear data: The nuclear data used in the data analysis were obtained from the Evaluated Nuclear Structure Data File (ENSDF) [102]. Only the uncertainties of the decay gamma intensity greater than 1% were considered, and those for the other nuclear data, such as half-lives and branching ratio of product decay, were neglected.

Table 3.5: Impurities contained in the sample foils.

Target	Impurities [ppm]
Mn	Al = 0.58, Sb = 53, B = 0.6, Ca = 2.2, Cr = 0.44, Co = 0.86, Cu = 26, Au < 0.5, Fe = 2.4, Pb = 15, Mg = 110, Mo = 2.5, Ni = 0.43 K = 1.8, Se = 250, Si = 9.1, Na = 1.1, Sr = 0.12, Ta < 5, Ti = 0.25 Sn = 1.1, Zn = 56
Co	Al = 1, Bi < 1, Ca < 1, Cr = 2, Fe = 5, Mg < 1, Mn < 1, Si = 20, Ag = 1
Ni	Cu<2500, Fe<4000, Mg<2000, Mn<3500, Si<1500, Ti<1000, C<1500, S<100
Zr	Fe = 39, Hf = 2070, Cr = 10, O = 52, H = 1, N = 3, C = 4

The abovementioned sources of uncertainties were considered independent. Thus, the total uncertainties quoted for the measured cross sections were evaluated according to the error propagation law following the same method employed in Ref. [79].

3.5 Results and Discussion

In this work, 21, 27, 24, and 43 residual nuclides produced in proton-induced reactions on ^{55}Mn, ^{59}Co, ^{nat}Ni, and ^{nat}Zr, respectively, or totally 384 cross sections, were measured. The numerical data are listed in Tables A.1–A.4. Among them, the data of the following reactions were measured for the first time: ^{55}Mn(p,X)^{38}S, ^{55}Mn(p,X)^{41}Ar, ^{59}Co(p,X)^{38}S, ^{nat}Zr(p,X)^{28}Mg, ^{nat}Zr(p,X)^{42}K, ^{nat}Zr(p,X)^{43}K, ^{nat}Zr(p,X)^{44g}Sc, ^{nat}Zr(p,X)^{55}Co, ^{nat}Zr(p,X)^{69m}Zn, and ^{nat}Zr(p,X)^{93}Y reactions.

The measured data were compared with the previous data [78]–[81], [103]–[128]

taken from the EXFOR database[129], model-based cross section calculations, and evaluated data of nuclear data library JENDL/HE-2007 [35], [130], [131]. To compare the calculated cross sections with the experimental results, cumulative cross sections were calculated from the theoretical predictions because the calculated cross sections are independent, whereas most experimental results are cumulative. If a reaction product is the n-th nuclide in a decay chain, the cumulative cross section, $\sigma_n^{\rm cum}$, is calculated by the formula [132],

$$\sigma_n^{\rm cum} = \sigma_n^{\rm ind} + \sum_{i=1}^{n-1}(\sigma_i^{\rm ind}\prod_{j=i}^{n-1}\nu_j), \tag{3.13}$$

where $\sigma_i^{\rm ind}$ is the independent cross section of the i-th precursor nuclide, and ν_j is the decay probability of the j-th nuclide into the $(j+1)$-th one.

Since a vast number of cross sections were measured, not all results are shown in the next section. The results are shown by three mass regions, i.e., light ($A_{\rm product} < 30$), medium-heavy ($30 \leq A_{\rm product} \lesssim 0.9A_{\rm target}$), and heavy ($A_{\rm product} \gtrsim 0.9A_{\rm target}$), classified by incident energy dependence.

3.5.1 Excitation Functions

Cross sections for light reaction products

The lightest products measured in this work were ^{7}Be, followed by ^{22}Na, ^{24}Na, etc. The experimental results for these products are shown in Figs. 3.10–3.12. The subscripts, "ind." and "cum.," in the residual nuclei indicate whether the cross section is independent and cumulative.

The present data are generally consistent with the previous data taken from EXFOR database within the experimental uncertainties. One can see that the experimental uncertainty of the present work is smaller than previous works, which are typically >10%. This is because the cross sections were derived as the relative value of monitor reactions, such as ^{27}Al(p,X)^{22}Na reaction, in the previous works. The uncertainty of the monitor reactions increased the experimental uncertainties. In this work, the cross sections were derived as absolute values, and total uncertainties were reduced to typically <6%.

The experimental cross sections for ^{7}Be, ^{22}Na, and ^{24}Na show similar energy incident energy dependence: the cross sections increase as the incident proton energy increases, as shown in Figs. 3.10–3.12. The cross sections for ^{7}Be and ^{24}Na take close values among the four targets, although the cross sections of ^{22}Na from $^{\rm nat}$Zr takes smaller value by about two. The calculated cross sections and evaluated values successfully reproduced the incident energy dependence for all cases. The INCL4.6/GEM and JAM/GEM generally underestimate the experimental

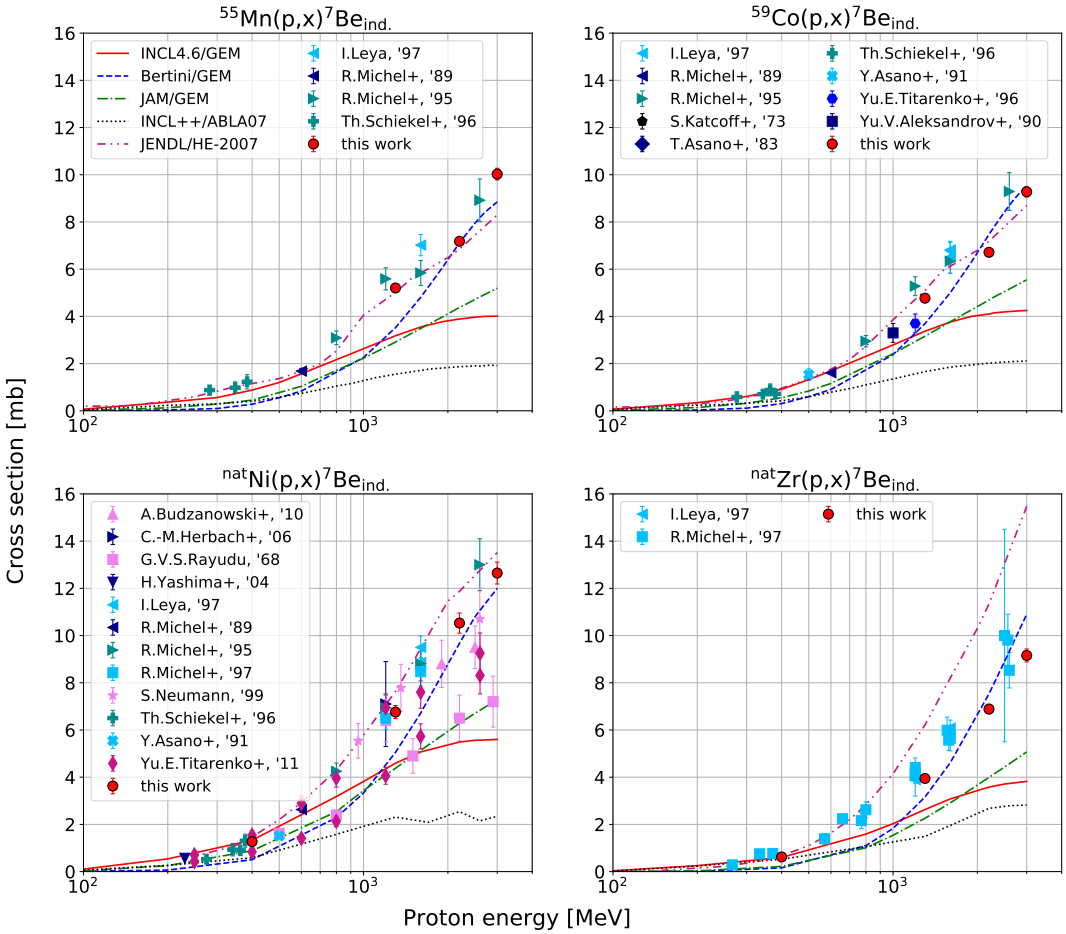

Figure 3.10: Experimental, calculated, and evaluated production cross sections for ^{7}Be production from the ^{55}Mn, ^{59}Co, $^{\mathrm{nat}}$Ni, and $^{\mathrm{nat}}$Zr targets.

cross sections for ^{7}Be, ^{22}Na, and ^{24}Na. Because the light products are mainly produced in the evaporation processes, the GEM may underestimate the production of light products. Conversely, the Bertini/GEM show relatively good agreement with the experimental data. This may be due to the higher excitation energy formed just after the INC process, compared with the INCL4.6 and JAM models. The INCL++/ABLA07 generally underestimates the ^{7}Be production, while it overestimates the cross sections for ^{24}Na production. This may be because the ABLA07 uses an empirical formula to describe the intermediate mass fragment emission [89]. The JENDL/HE-2007 successfully reproduces the experimental cross sections with some exceptions: cross sections of $^{\mathrm{nat}}$Ni$(p,X)^{24}$Na and $^{\mathrm{nat}}$Zr$(p,X)^{24}$Na reactions are underestimated.

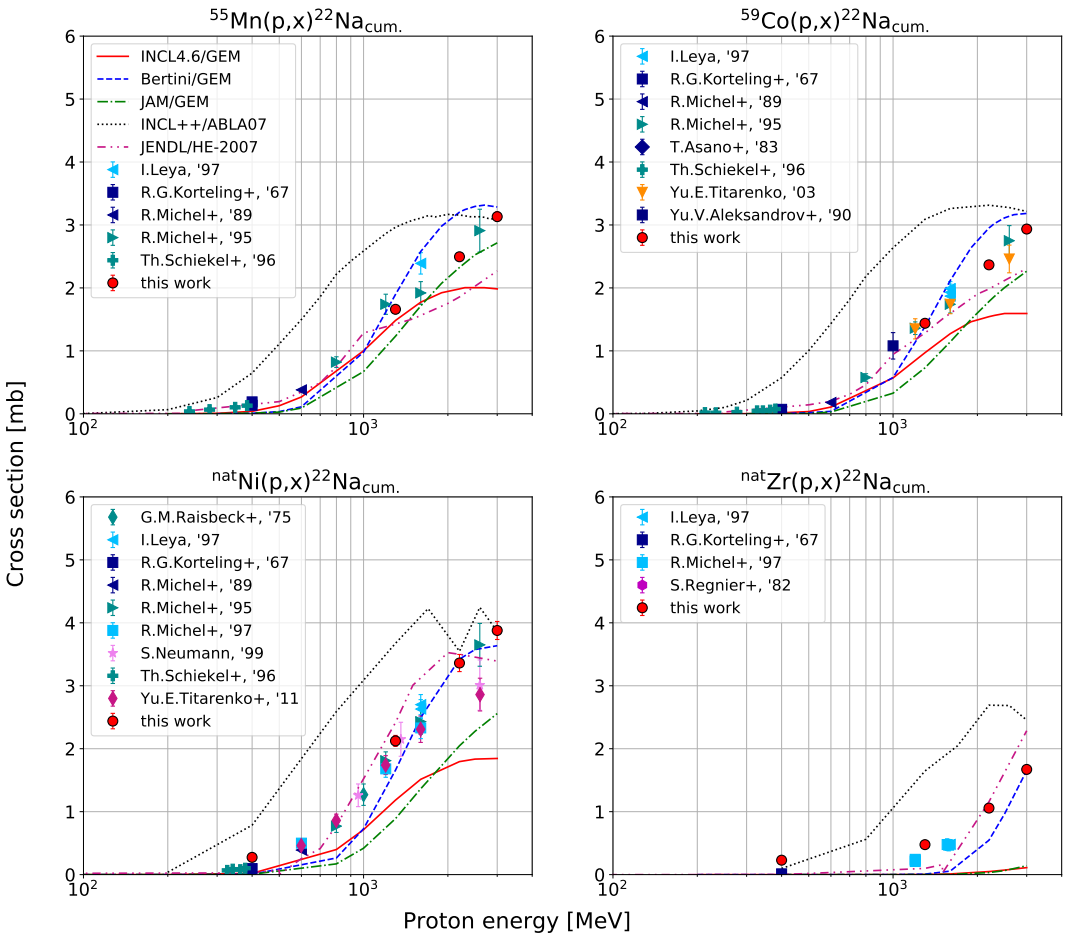

Figure 3.11: Same as Fig. 3.10, but for ^{22}Na production.

Cross sections for medium-heavy products

The experimental results for medium-heavy products ($30 \leq A_{\mathrm{product}} \lesssim 0.9A_{\mathrm{target}}$) are shown in Figs. 3.13–3.16. The cross sections for these products have a broad maximum between 0.4 and 1.0 GeV for the ^{55}Mn, ^{59}Co, $^{\mathrm{nat}}$Ni targets, and for the $^{\mathrm{nat}}$Zr target, the maximum generally shift to higher incident energy. The maximum shifts to lower energies with an increase in the mass number of the reaction products. The spallation models and JENDL/HE-2007 generally reproduce the incident energy dependencies for medium-heavy products.

A large discontinuity can be observed in some excitation functions in Figs. 3.13–3.16 around 250 MeV. According to Ref. [35], this discontinuity is due to the use of different model codes in the cross section evaluation at incident energies less than 250 MeV and above.

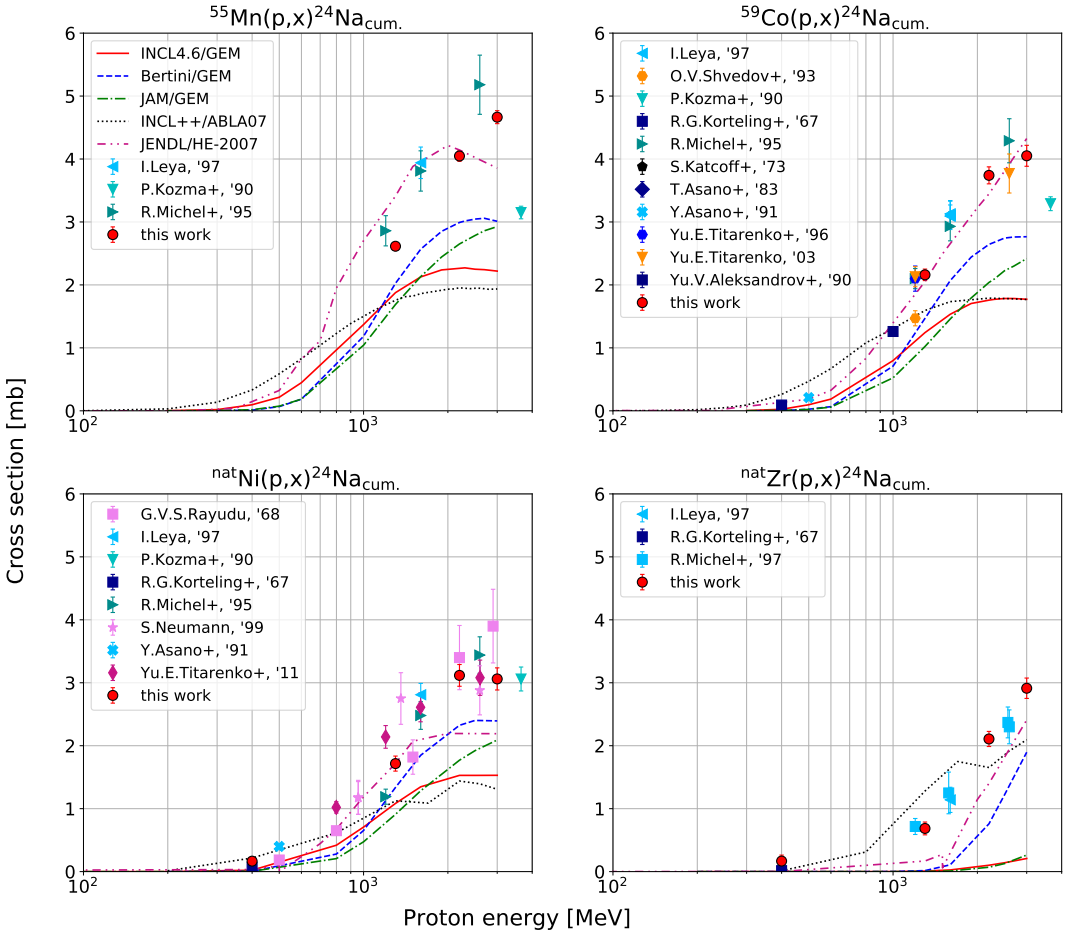

Figure 3.12: Same as Fig. 3.10, but for ^{24}Na production.

When focusing on the cross section of the same product, the cross section gets smaller with increasing the target mass number. An example is the cross section of ^{42}K from ^{55}Mn, ^{59}Co, $^{\mathrm{nat}}$Ni, and $^{\mathrm{nat}}$Zr (Figs. 3.13–3.16). This is because the heavier target must emit more nucleons and requires higher excitation energy to produce the same products, and therefore, the production cross section decreases with increasing target atomic number. The same is true for other products, e.g., ^{43}K, ^{47}Ca, and ^{46}Sc.

The reaction models and JENDL/HE-2007 show relatively good agreement for the production of medium-heavy products. However, some discrepancies were observed: the Bertini/GEM considerably overestimates the cross section of ^{55}Mn(p,X)^{47}Ca, ^{55}Mn(p,X)^{48}Cr, and ^{59}Co(p,X)^{47}Ca reactions. The INCL++/ABLA07 underestimates ^{55}Mn(p,X)^{42}K, ^{55}Mn(p,X)^{46}Sc, $^{\mathrm{nat}}$Zr(p,X)^{72}As, and $^{\mathrm{nat}}$Zr(p,X)^{84}Rb reactions.

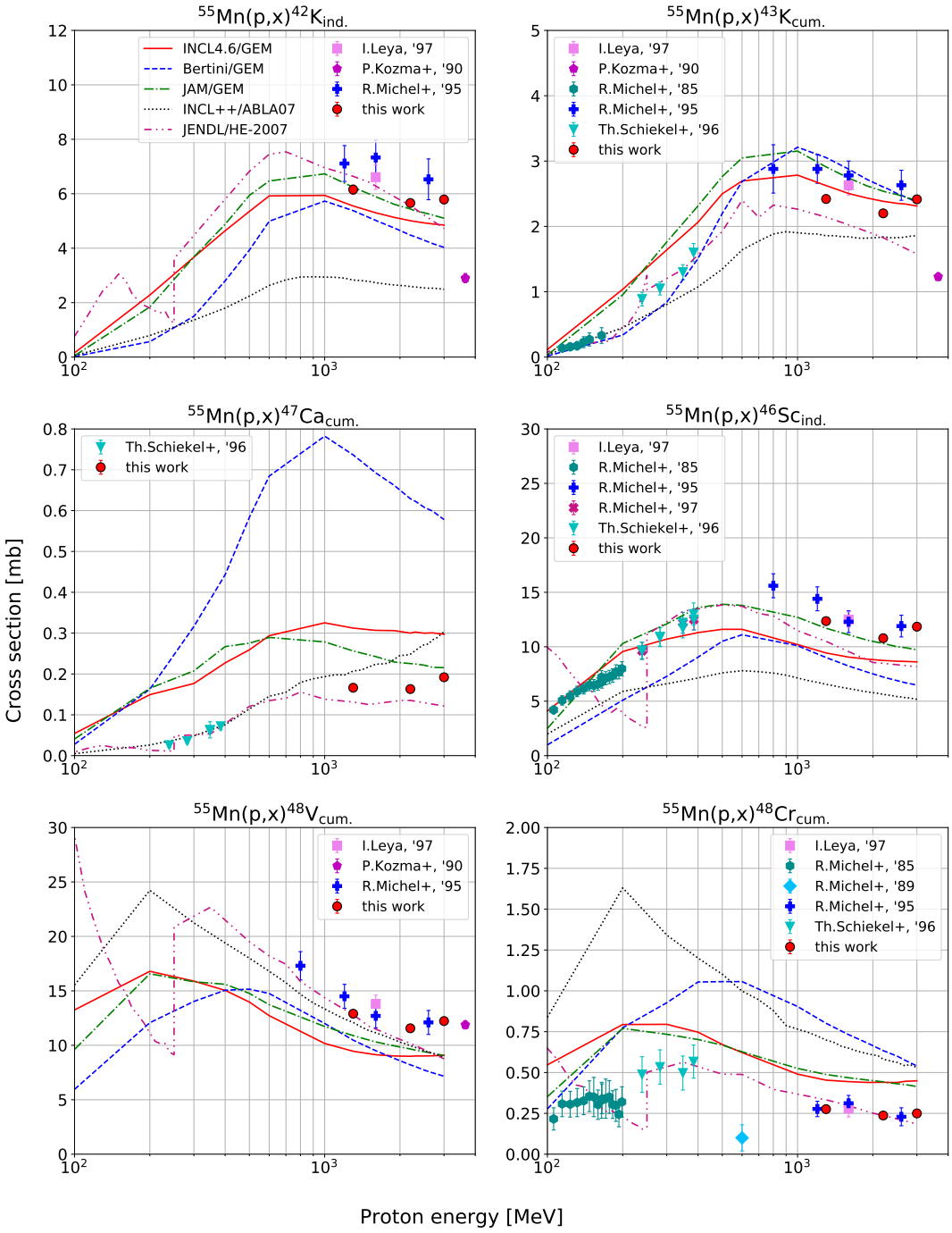

Figure 3.13: Experimental, calculated, and evaluated production cross sections for medium-heavy products from the ^{55}Mn target.

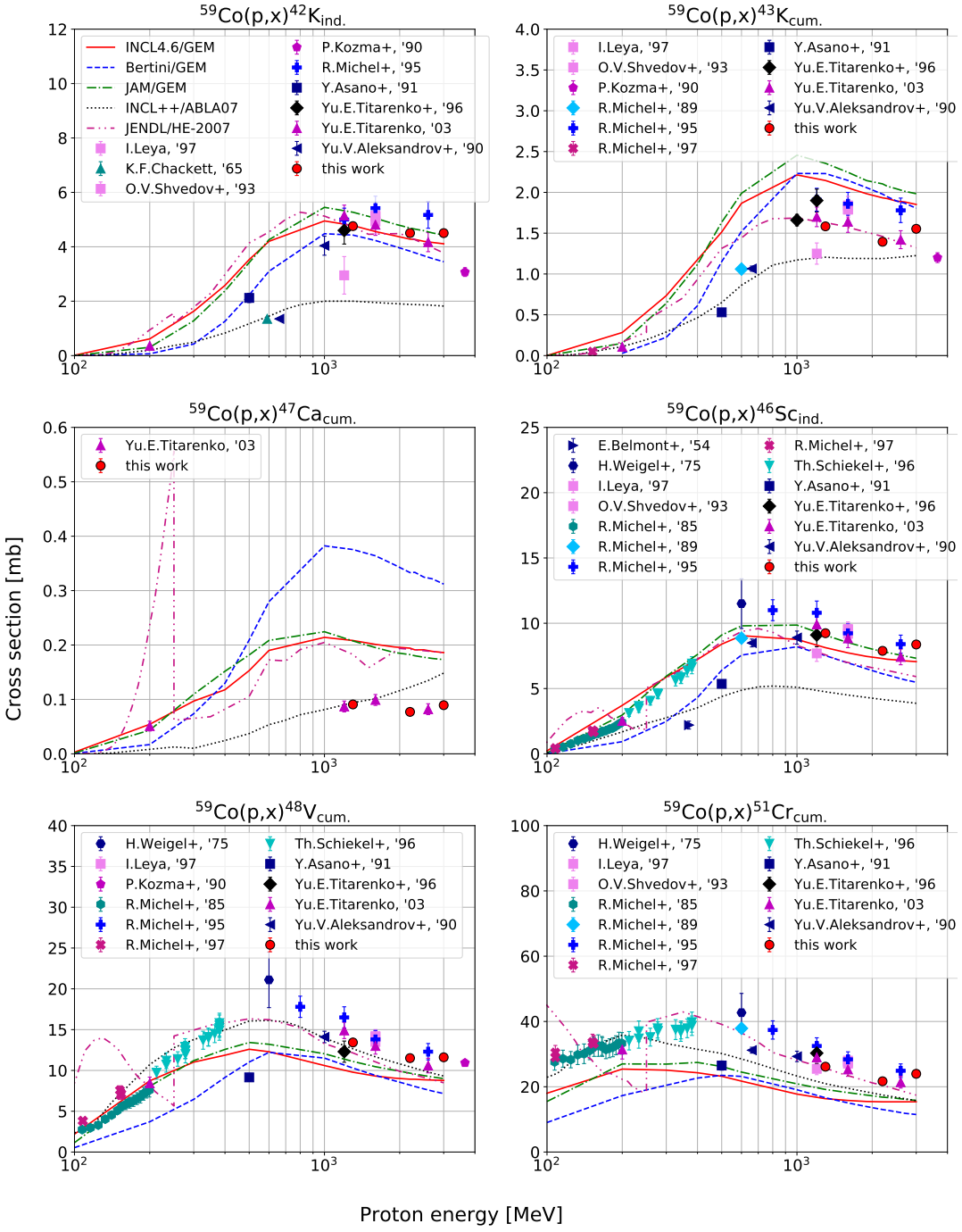

Figure 3.14: Same as Fig. 3.13, but for the ^{59}Co target.

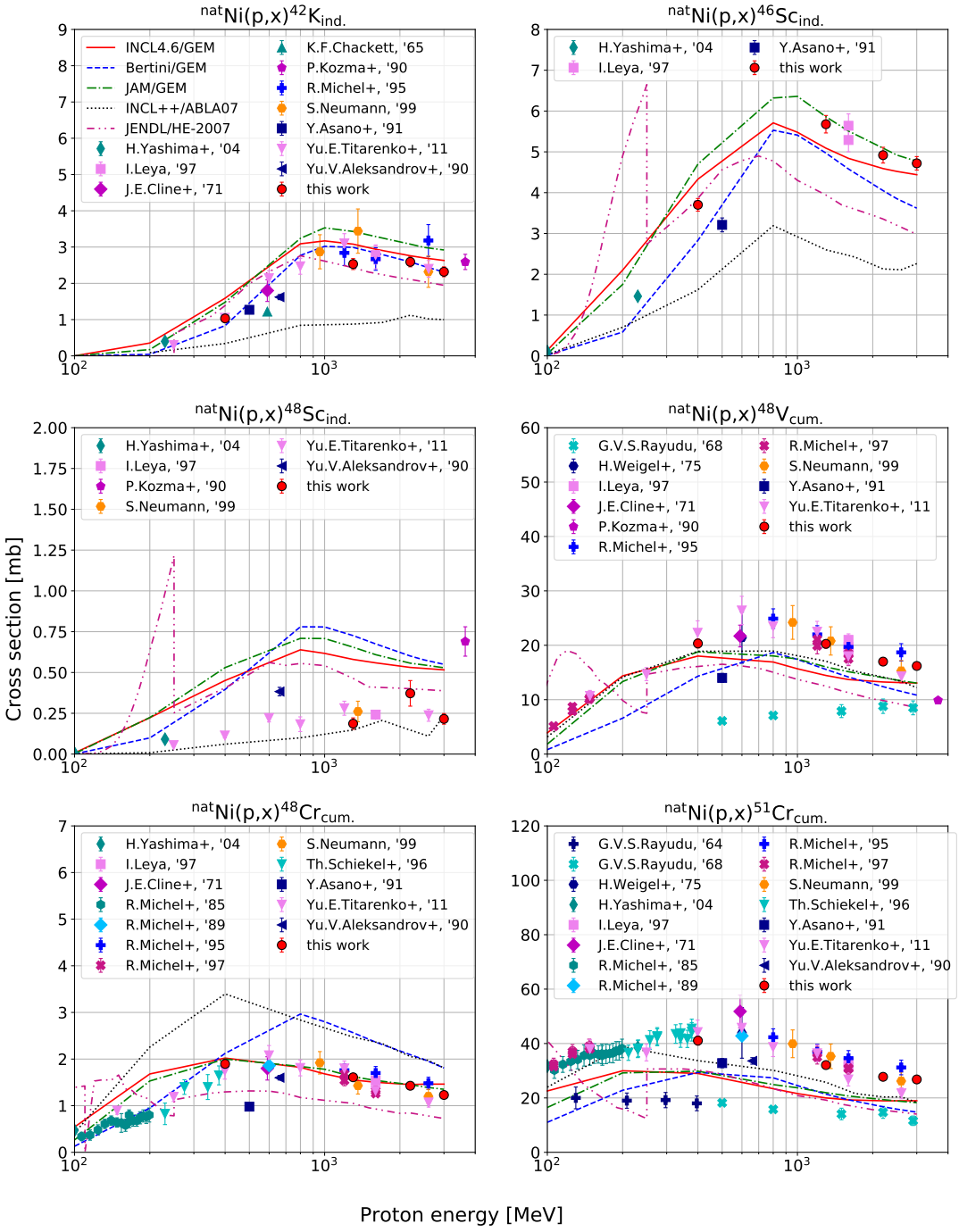

Figure 3.15: Same as Fig. 3.13, but for the $^{\text{nat}}$Ni target.

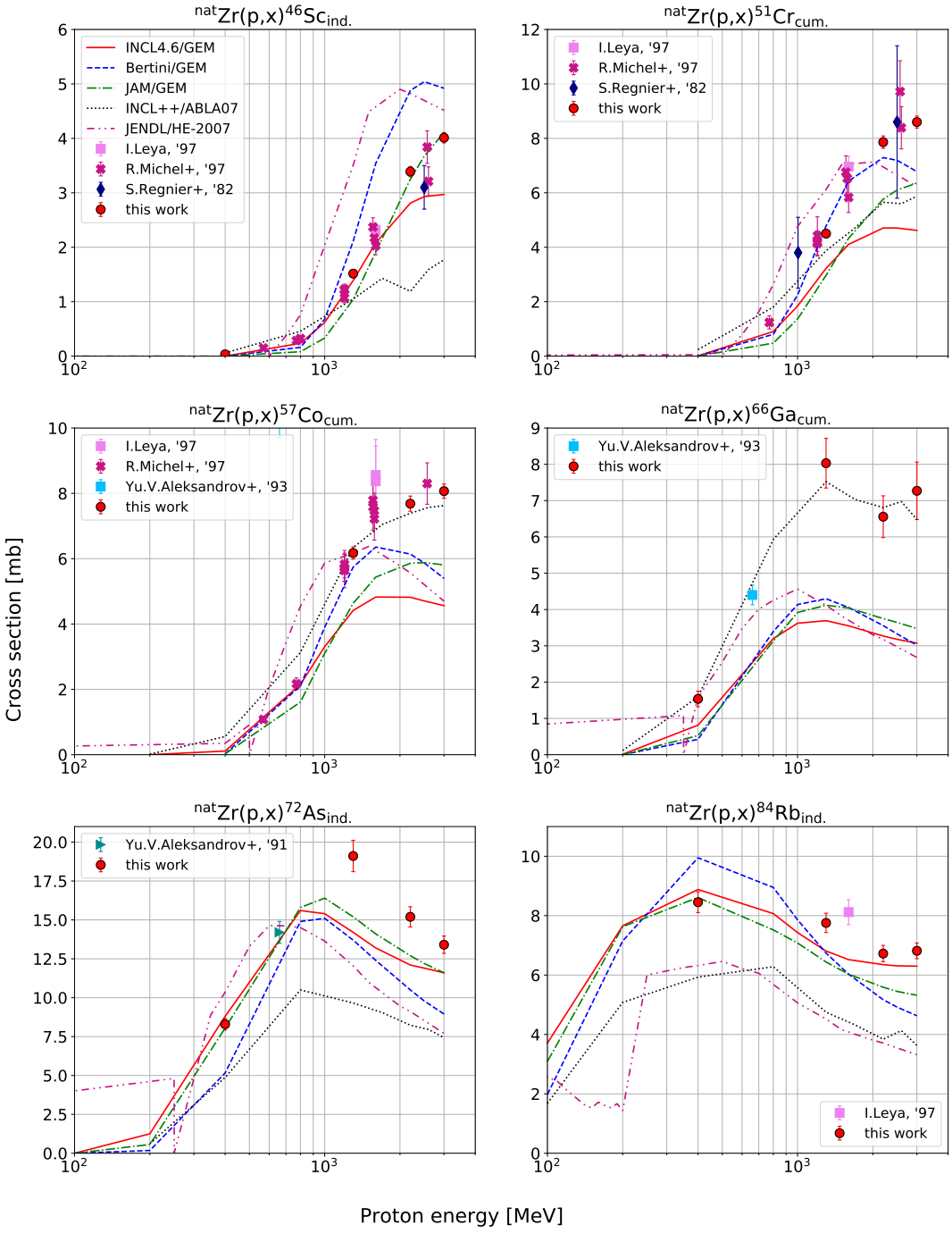

Figure 3.16: Same as Fig. 3.13, but for the ^{nat}Zr target.

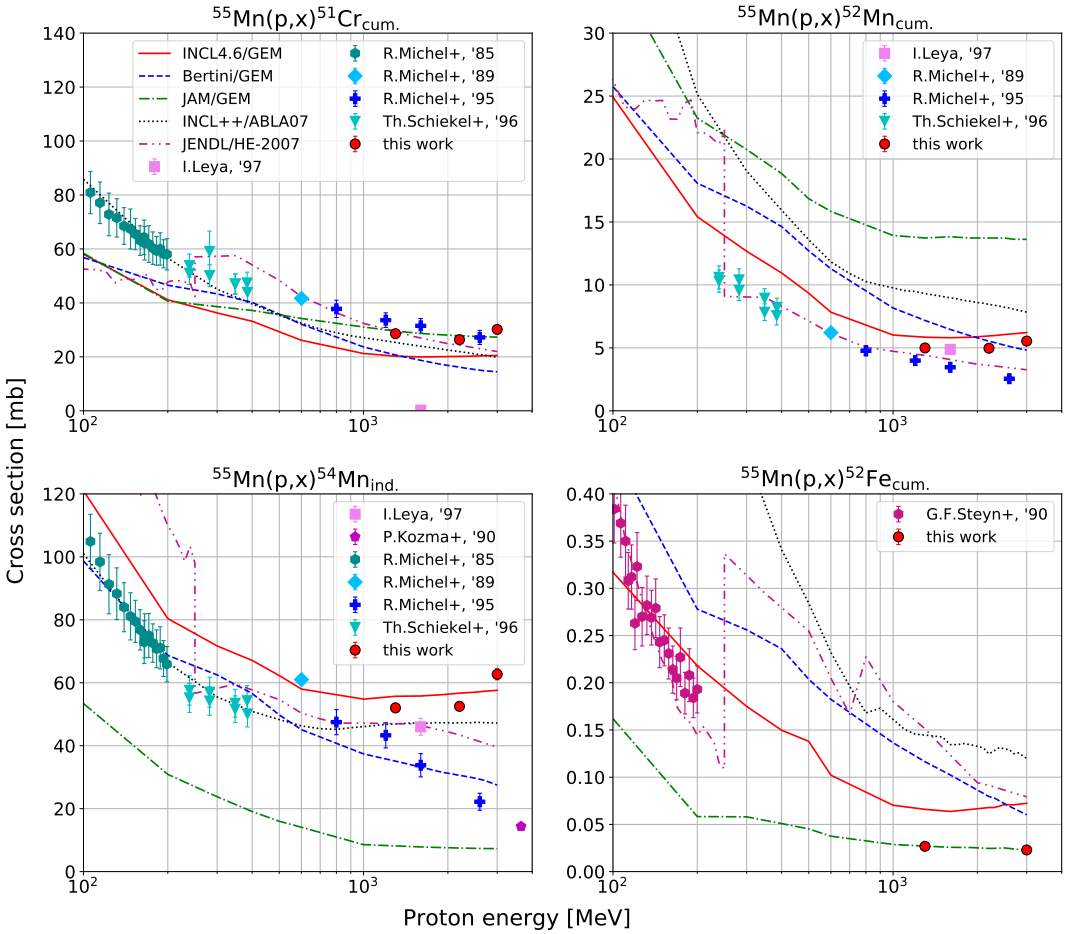

Figure 3.17: Experimental, calculated, and evaluated production cross sections for heavy products from the ^{55}Mn target.

Cross sections for heavy products

Figures 3.17–3.20 show the experimental results for heavy products ($A_{\mathrm{product}} \gtrsim 0.9A_{\mathrm{target}}$). The cross section for the heavy products decrease with an increase in the incident proton energy above 100 MeV. The model-based cross section calculations and JENDL/HE-2007 generally reproduce the incident energy dependencies for the heavy products.

The present data generally consistent with most of previous data within the experimental uncertainties. However, the incident energy dependencies of the cross sections for ^{55}Mn(p,X)^{54}Mn, ^{59}Co(p,X)^{58}Co, and $^{\mathrm{nat}}$Ni(p,X)^{58}Co reactions are quite different between the present data and previously measured data [78], [104], as shown in Fig. 3.17–3.19. In the previous work, a significant correction for

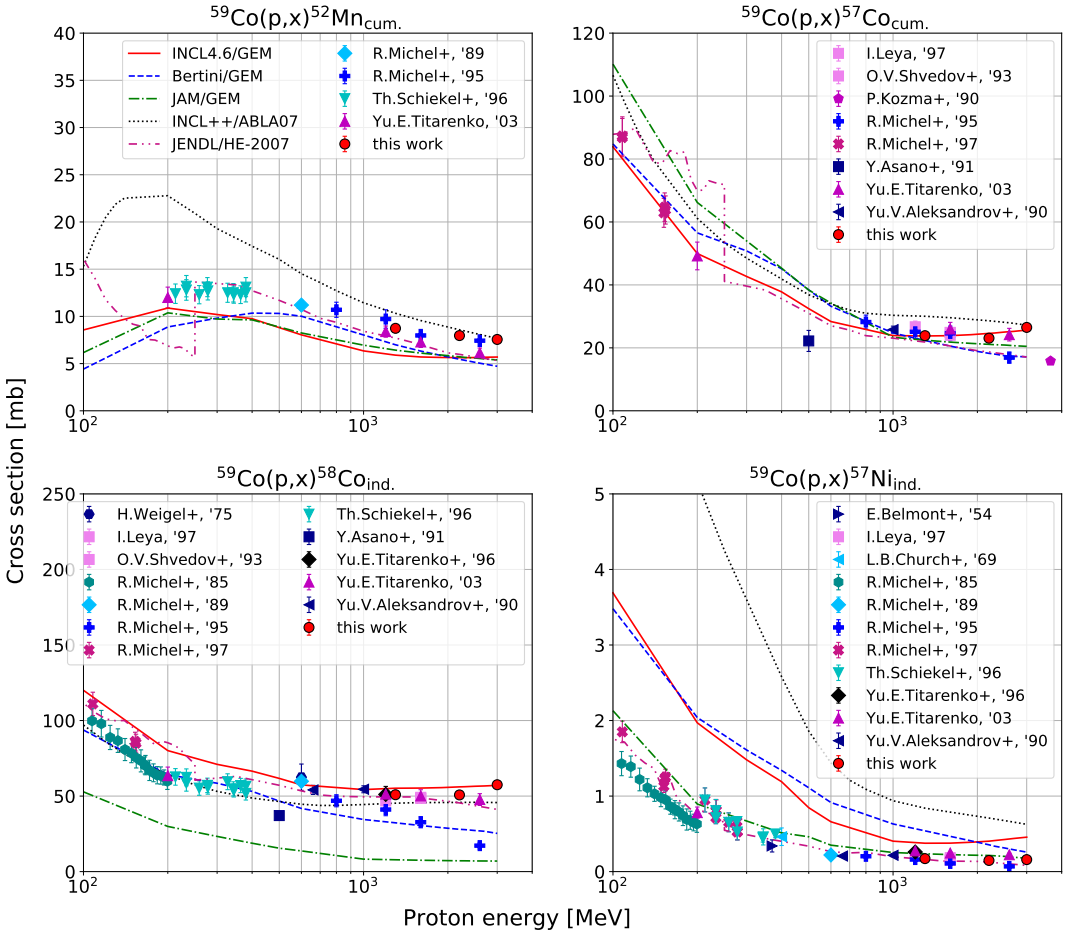

Figure 3.18: Same as Fig. 3.17, but for the ^{59}Co target.

the secondary particles were performed: as for the ^{55}Mn(p,X)^{54}Mn reaction, for example, Fig.4 in Ref. [78] indicates that the ratio of the corrected cross section to that of the non-corrected cross section for 2.6 GeV was approximately 0.25. In this work, however, the corresponding correction, $f_{\rm sec}$ as detained in Section 3.4.1, is approximately 0.85. The large correction in Ref. [78] may be caused by the rather thick target stack used in their experiment (between 9.35 and 15.6 g/cm^2), compared to those used in the present measurement ($\sim$1.55 g/cm^2).

The spallation models and JENDL/HE-2007 show relatively good agreement for heavy products as well. However, cross sections for some reaction products are failed to reproduce: the cross sections for ^{55}Mn(p,$p3n$)^{52}Mn, $^{\rm nat}$Ni(p,pX)^{56}Ni, and $^{\rm nat}$Zr(p,X)^{86}Zr reactions are overestimated by all the spallation models used in this work. The JENDL/HE-2007 successfully reproduces the cross sections for ^{55}Mn(p,X)^{52}Mn, ^{59}Co(p,X)^{57}Ni, and $^{\rm nat}$Ni(p,X)^{56}Ni reactions. The JAM/GEM

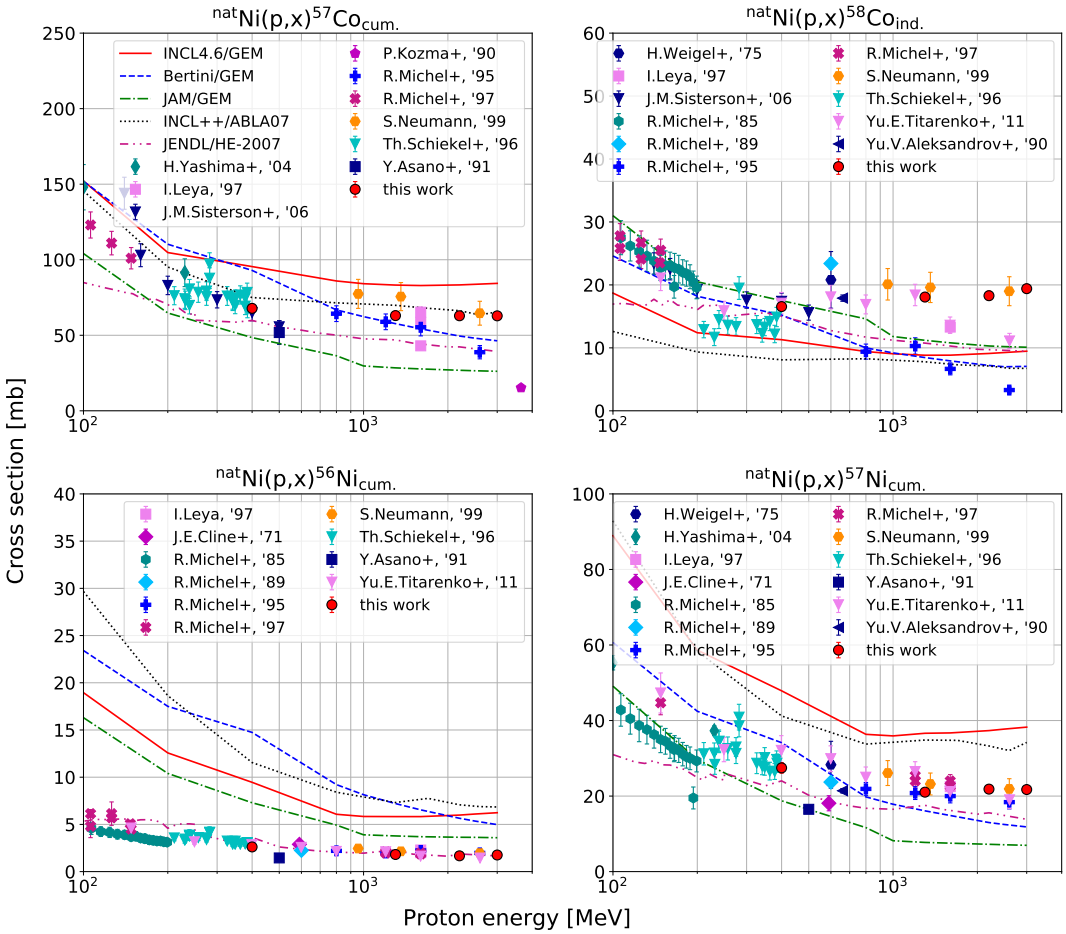

Figure 3.19: Same as Fig. 3.17, but for $^{\mathrm{nat}}$Ni target.

successfully reproduces the measured cross sections of the reaction products whose atomic numbers are larger than the respective targets by one, i.e., ^{55}Mn(p,X)^{52}Fe and ^{59}Co(p,X)^{57}Ni reactions.

Newly measured data

Among the measured data, the cross sections for 10 target/production combinations were measured for the first time in this work. Figs. 3.21 and 3.22 show the comparison of the measured data with the model-based cross section calculations and evaluated cross sections. It should be noted that the calculations for $^{\mathrm{nat}}$Zr(p,X)$^{69\mathrm{m}}$Zn and $^{\mathrm{nat}}$Zr(p,X)$^{44\mathrm{g}}$Sc reactions were not available because the spallation reaction models cannot treat the transition to isomeric states of product nuclides and therefore, cannot distinguish between the ground and isomeric state

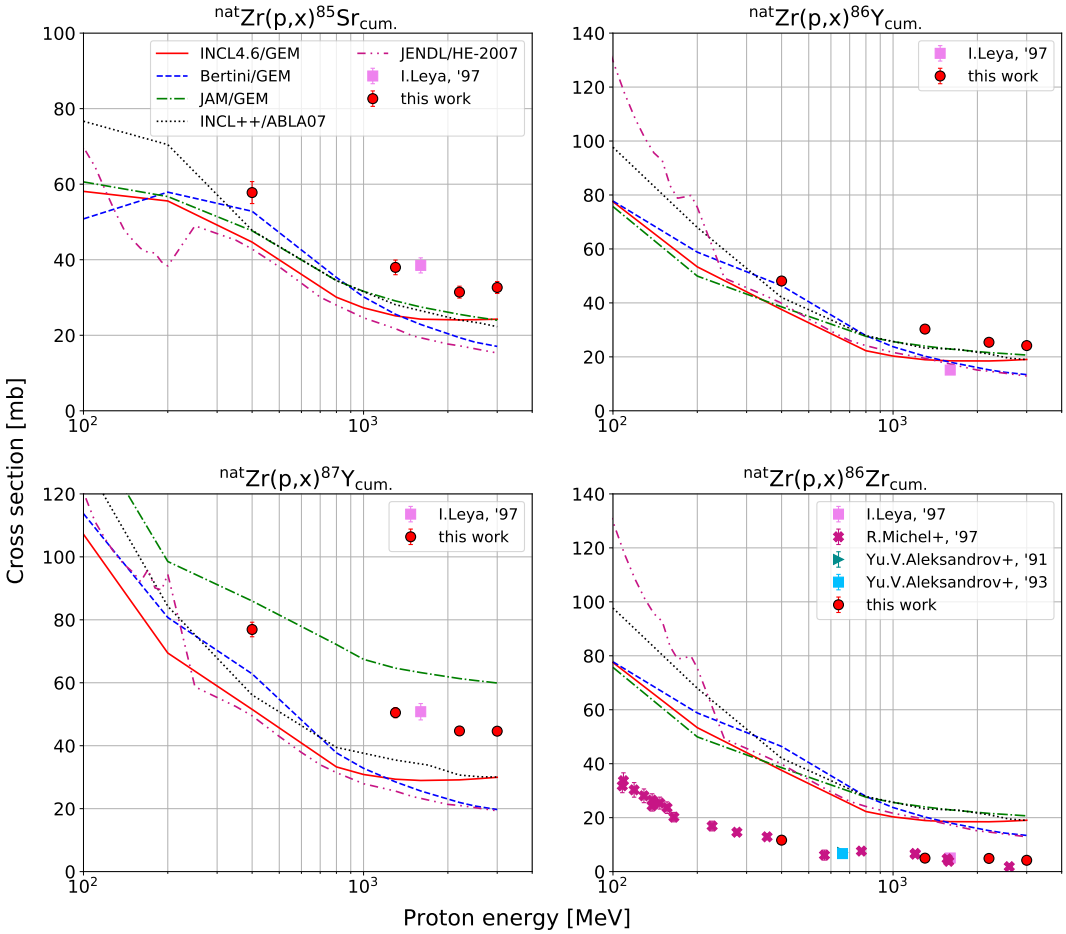

Figure 3.20: Same as Fig. 3.17, but for ^{nat}Zr target.

of the products.
For these products, the spallation models and JENDL/HE-2007 roughly reproduce the incident energy dependencies. However, the INCL++/ABLA07 considerably overestimates the cross sections of ^{55}Mn(p,X)^{38}S, ^{59}Co(p,X)^{38}S, and ^{nat}Zr(p,X)^{55}Co reactions. Moreover, all the calculations and JENDL/HE-2007 remarkably underestimate the cross section of ^{nat}Zr(p,X)^{28}Mg reaction.

3.5.2 Deviation Factors

As discussed in Section 3.5.1, spallation reaction models and JENDL/HE-2007 library generally reproduce the incident energy dependencies of the production cross sections. In this section, the benchmark analysis of the spallation reaction models and the JENDL/HE-2007 is quantitatively performed by introducing the

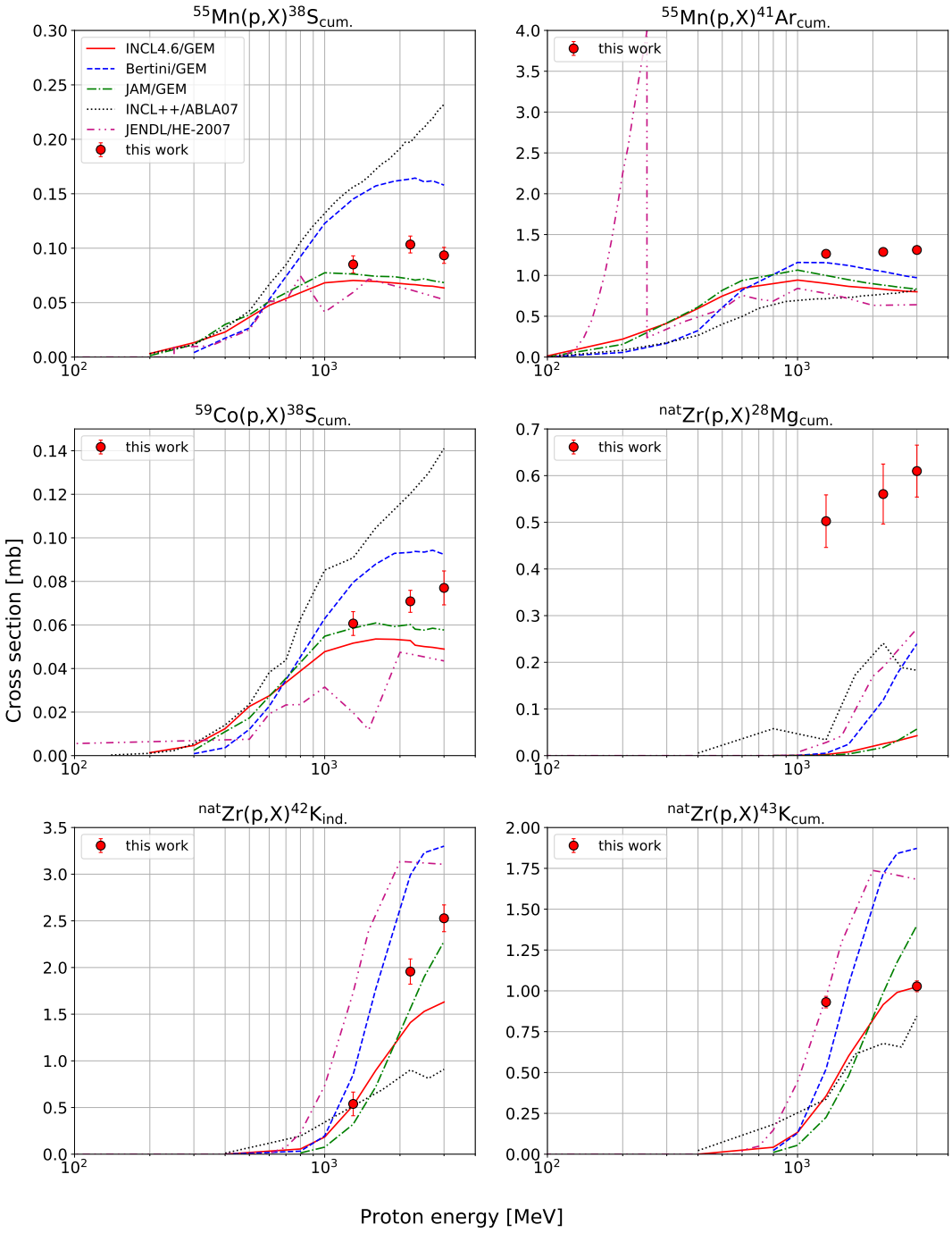

Figure 3.21: Experimental, calculated, and evaluated cross sections of reaction products, which were newly measured in this work.

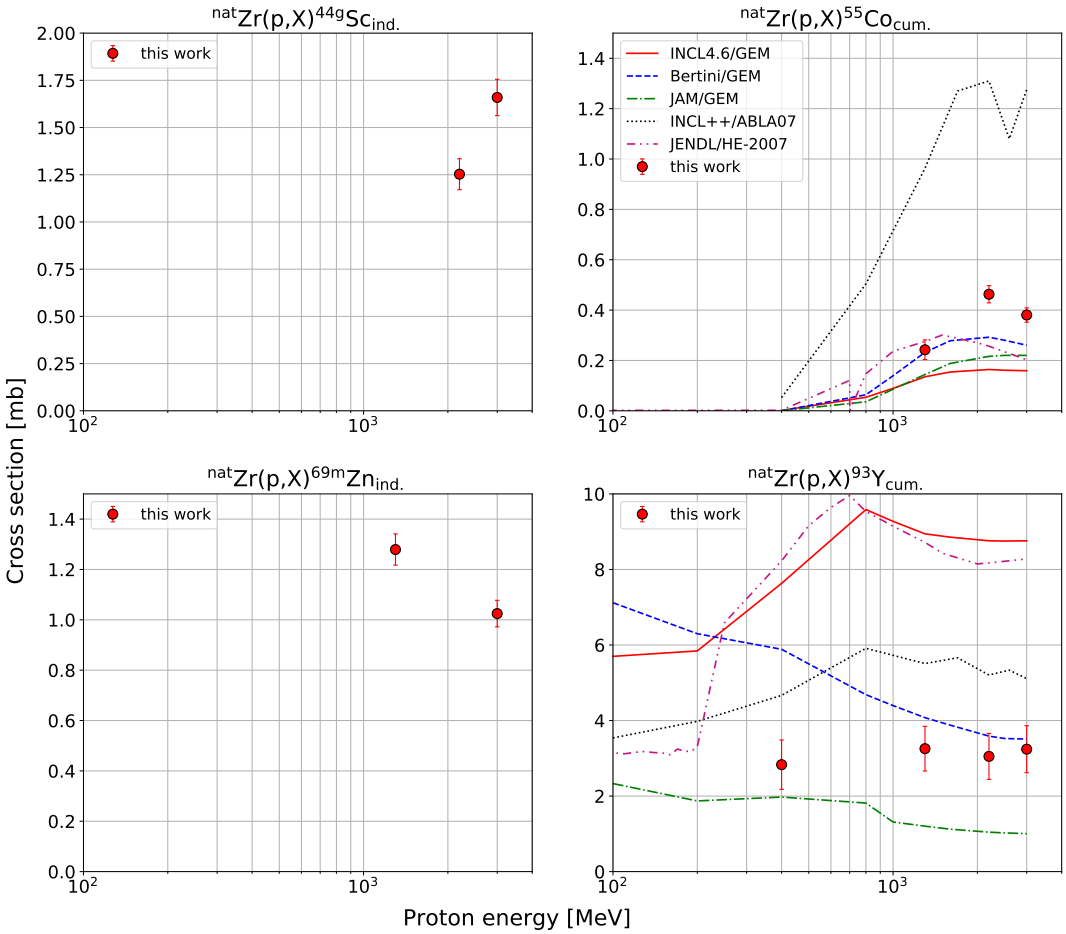

Figure 3.22: Same as Fig. 3.21.

mean square deviation factor $\langle F \rangle$. The deviation factor $\langle F \rangle$ is defined in same manner as in Ref. [133] by the following expression:

$$\langle F \rangle = 10^{\sqrt{R}}, \tag{3.14}$$

where exponent R is defined by

$$R = \frac{1}{n_r} \sum_{i=1}^{n_r} \left[\log_{10}(\sigma_{\mathrm{cal},i}/\sigma_{\mathrm{exp},i}) \right]^2 . \tag{3.15}$$

Here, $\sigma_{\mathrm{exp},i}$ and $\sigma_{\mathrm{cal},i}$ denote the experimental data in this work and the calculated cross sections or the JENDL/HE-2007 data for the i-th reaction product, respectively; n_r denotes the number of the data points in this work included in the calculation of $\langle F \rangle$. Because the shape of the excitation functions differs de-

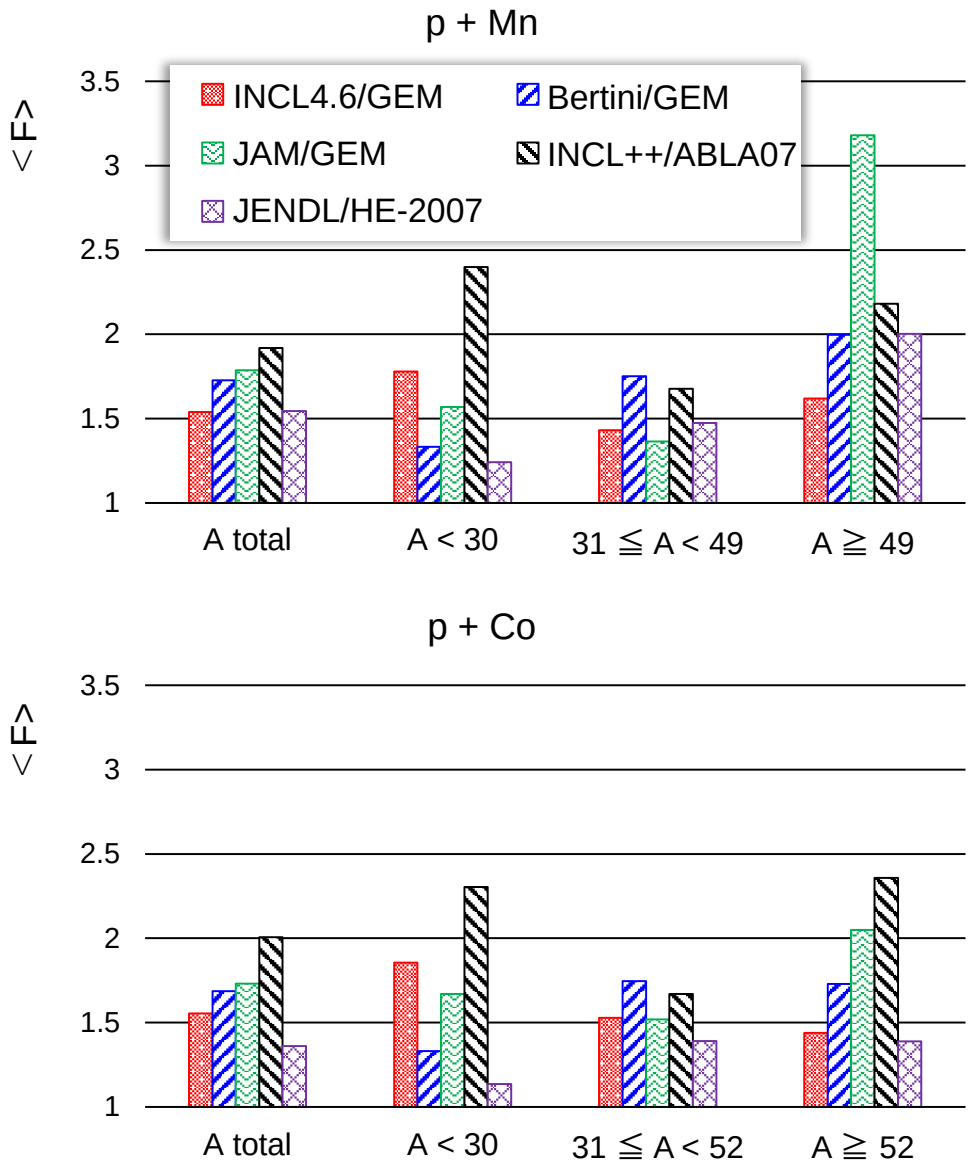

Figure 3.23: Deviation factor $\langle F \rangle$ of the ^{55}Mn and ^{59}Co targets calculated by the INCL4.6/GEM, Bertini/GEM, JAM/GEM, INCL++/ABLA07, and evaluated nuclear data library JENDL/HE-2007.

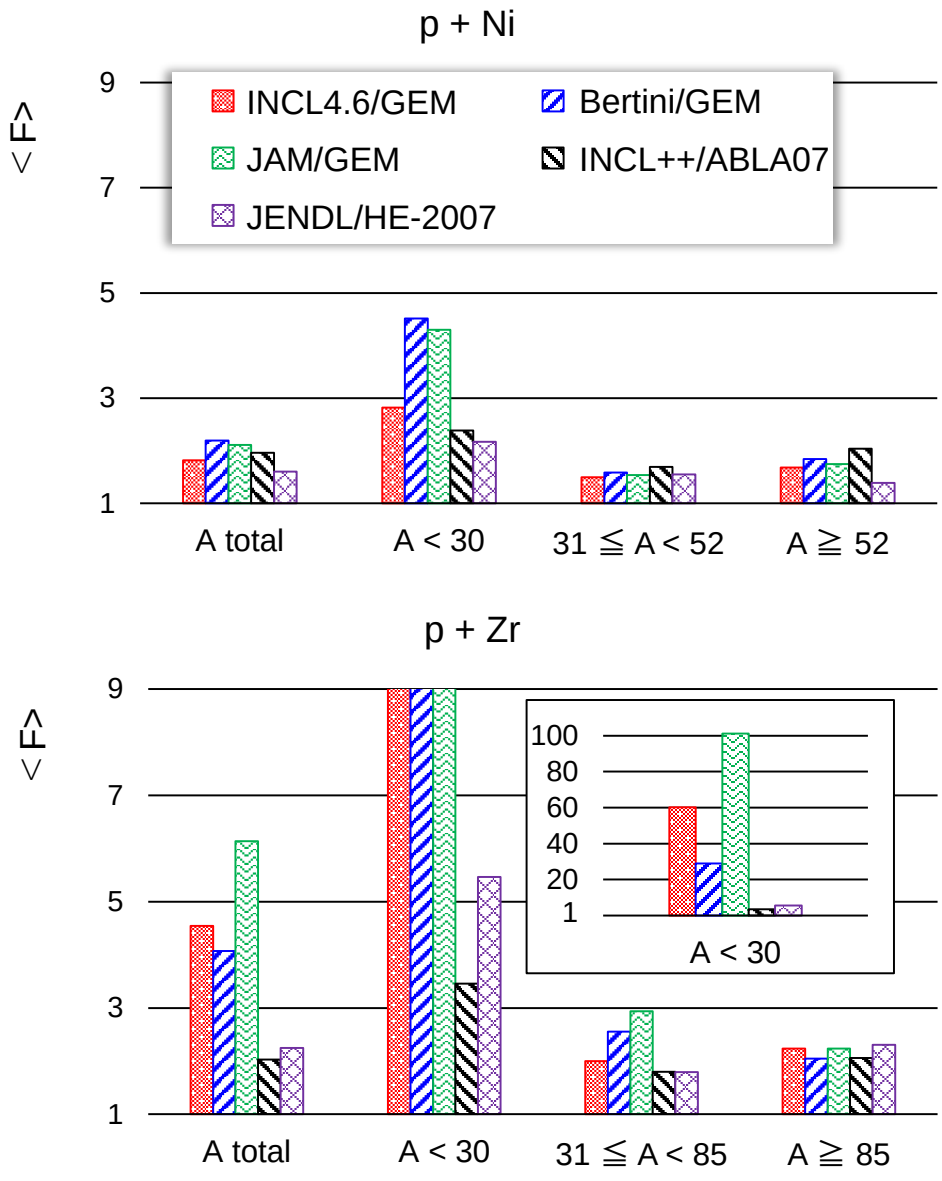

Figure 3.24: Same as Fig. 3.23, but for the $^{\mathrm{nat}}$Ni and $^{\mathrm{nat}}$Zr targets. The additional figure in the lower figure shows the $\langle F \rangle$ for the light products ($A < 30$) with a wide range.

pending on the mass number of reaction products, as discussed in Section 3.5.1, the deviation factor $\langle F \rangle$ was calculated for the respective mass regions: $A < 30$, $30 \leq A < 49$, and $A \geq 49$ for the Mn target, $A < 30$, $30 \leq A < 52$, and $A \geq 52$ for the Co and Ni targets, $A < 30$, $30 \leq A < 85$, and $A \geq 85$ for the Zr target, as well as for all the reaction products (denoted as "A total" in Figs. 3.23 and 3.24). Notably, the calculations for ^{44g}Sc and isomers were not considered. The numerical values of $\langle F \rangle$ are listed in Table A.5. The factor $\langle F \rangle$ assumes a value close to one if the reproducibility of the calculation is good, and assumes a larger value as the reproducibility worsens.

The calculated factors $\langle F \rangle$ of the Mn and Co targets are shown in Fig. 3.23 and those of the Ni and Zr targets are shown in 3.24. The factor $\langle F \rangle$ for the INCL4.6/GEM provides relatively small values for the medium-heavy and heavy products, $A > 30$. For the Zr target, a large discrepancy is seen for light nuclides, $A < 30$, leading to a large $\langle F \rangle$ for "A total." The same is true for the Bertini/GEM and JAM/GEM. This is because the production cross section for ^{24}Na production is remarkably underestimated, as shown in Fig. 3.12. The Bertini/GEM results are in good agreement for the production of light nuclides for the Mn and Co targets. Contrary, the Bertini/GEM agrees well for the medium-heavy and heavy products from the Ni and Zr targets, and shows poor reproducibility for light products. The JAM/GEM gives relatively small values for medium-heavy products for the Mn, Co targets. For the Ni and Zr targets, the JAM/GEM gives relatively small values. The INCL++/ABLA07 exhibits poor reproducibility for heavy products from the Mn and Co targets although it shows good agreements for the Ni and Zr targets. The JENDL/HE-2007 library gives the lowest values for light products for the Mn, Co, and Ni targets. As for the $\langle F \rangle$ of "A total," the JENDL/HE-2007 exhibits the best reproducibility for the Co and Ni targets. Moreover, JENDL/HE-2007 also exhibits high reproducibility for the Ni and Zr targets, for which INCL4.6/GEM and INCL++/ABLA07 exhibit the best reproducibilities, respectively. The JENDL/HE-2007 library exhibits the best reproducibility, its $\langle F \rangle$ values of "A total" take values >1.4, which corresponds to average deviation of >40% from the experimental data. These values still exceed the required accuracy of 30% [134].

3.6 Conclusions

Nuclide production cross sections in proton-induced spallation reactions on Mn, Co, Ni, and Zr were measured with proton energies between 0.4 and 3.0 GeV at J-PARC. Due to the stable proton beam irradiation, the well-established beam profile-monitoring system, and the proton number correction method by the imaging plate, the systematic uncertainties could be reduced. The cross sections of fol-

lowing reactions were measured for the first time: ^{55}Mn(p,X)^{38}S, ^{55}Mn(p,X)^{41}Ar, ^{59}Co(p,X)^{38}S, ^{nat}Zr(p,X)^{28}Mg, ^{nat}Zr(p,X)^{42}K, ^{nat}Zr(p,X)^{43}K, ^{nat}Zr(p,X)^{44g}Sc, ^{nat}Zr(p,X)^{55}Co, ^{nat}Zr(p,X)^{69m}Zn, and ^{nat}Zr(p,X)^{93}Y reactions. The present results are consistent with the existing experimental data; however, some data were found to be inconsistent. This inconsistency might be due to the large correction for the secondary particles performed by previous work.

The incident energy dependence of the production cross sections differ depending on the mass number of reaction products: light ($A_{\mathrm{product}} < 30$), medium-heavy ($30 \leq A_{\mathrm{product}} \lesssim 0.9A_{\mathrm{target}}$), and heavy ($A_{\mathrm{product}} \gtrsim 0.9A_{\mathrm{target}}$) products. The cross sections for the light products increase as the incident proton energy increase. The cross sections for the medium-heavy products have a broad maximum, and the maximum shifts to lower incident energy with an increase in the mass number of the reaction products. For the heavy products, the cross sections decrease with an increase in the incident proton energy.

The model-based cross section calculation by INCL4.6/GEM, Bertini/GEM, JAM/GEM, and INCL++/ABLA07, and the evaluated nuclear data of JENDL/HE-2007 successfully reproduce the incident energy dependences of the experimental data. However, they disagree with the experimental data of some reactions. To examine the prediction capability of the spallation reaction models as well as the nuclear data, the mean square deviation factor [133] was introduced. As a result, the INCL4.6/GEM and INCL++/ABLA07 indicated the best reproducibility over a wide mass number range of residual nuclei for the Mn and Zr targets, respectively. The JENDL/HE-2007 exhibited the best reproducibility for the Co and Ni targets and showed good for the Mn and Zr targets. However, the deviation factor for the total mass range ("A total") exceeded 1.4, which corresponds to the deviation of 40% from the experimental value. This value exceeds the required data accuracy of 30%[135]. Thus, further improvement of data accuracy is required for PHITS simulation and nuclear data evaluation in the GeV energy range.

4 Conclusions and Future Works

4.1 Summary and Conclusions

The demands for intense neutron sources are expected to grow. The nuclear data play a vital role in the reliable assessment of the facilities. This work focuses on the deuteron accelerator-based neutron source and proton-induced spallation neutron sources, which are expected to expand neutron application fields due to its favorable characteristics.

In Chapter 2, double-differential neutron yields from LiF, C, Si, Ni, Mo, and Ta targets were measured using 6.7-MeV/u deuterons. These data are necessary for estimating the neutron yields from the target and the structural materials. The measured data were compared with the previously measured data using the 6.7-MeV/u tritons. From the comparison, the (d,xn) spectra have some characteristic bumps whereas no such structure was seen in the (t,xn) spectra. The (d,xn) reaction generated higher neutron yields than the (t,xn) reaction for low-Z targets. For low-Z targets, the contribution of deuteron breakup becomes larger. Contrarily, the (d,xn) reaction yielded less neutrons for high-Z target. For high-Z targets, the contribution of breakup of incident particle become less, and the neutron yields from the (t,xn) reactions become greater because the total kinetic energy is larger.

The measured (d,xn) data and the previous (t,xn) reactions were also compared with the theoretical calculations. For the (d,xn) data, INCL4.6/GEM generally overestimates the experimental values while the JQMD/GEM underestimate them. This is because both the reaction models cannot treat deuteron breakup process in an appropriate way. DEURACS, which is dedicated for deuteron-induced reactions, successfully reproduced the experimental data for the wide range of atomic numbers. By decomposing neutron spectra by each reaction process component, theoretical analysis of the (d,xn) reaction was performed. For the light targets, characteristic bumps in the (d,xn) spectra are caused by the non-elastic breakup reaction. For medium-heavy targets, the statistical decay component is responsible for the low-energy neutron emission, and the non-elastic breakup reaction is dominant at high-energy neutron emission. For the heavy targets, the contribution of

non-elastic breakup is negligible and the elastic breakup reaction, pre-equilibrium process and statistical decay make a large contribution.

The benchmark analysis of PHITS (INCL4.6/GEM and JQMD/GEM), CCONE and TALYS codes for the (t,xn) reactions were performed. INCL4.6/GEM overestimated the neutron spectra considerably for the heavy targets. TALYS roughly reproduced the experimental spectra although it underestimated the magnitudes of spectra. JQMD/GEM and CCONE showed relatively good agreement for Si, Ni, Mo, and Ta targets. For the deuteron-induced reaction, DEURACS was only the model that successfully reproduced the experimental spectra for the targets with wide range of atomic number. DEURACS is considered a promising calculation tool in developing basic nuclear data necessary for designing deuteron-based neutron sources.

In Chapter 3, the nuclide production cross sections were measured for Mn, Co, Ni, and Zr targets with incident proton energies ranging from 0.4 to 3.0 GeV at J-PARC. In total, the cross sections of 115 target/product combinations were measured. Among the measured data, the cross sections for the following reactions were measured for the first time: ^{55}Mn(p,X)^{38}S, ^{55}Mn(p,X)^{41}Ar, ^{59}Co(p,X)^{38}S, $^{\mathrm{nat}}$Zr(p,X)^{28}Mg, $^{\mathrm{nat}}$Zr(p,X)^{42}K, $^{\mathrm{nat}}$Zr(p,X)^{43}K, $^{\mathrm{nat}}$Zr(p,X)$^{44\mathrm{g}}$Sc, $^{\mathrm{nat}}$Zr(p,X)^{55}Co, $^{\mathrm{nat}}$Zr(p,X)$^{69\mathrm{m}}$Zn, and $^{\mathrm{nat}}$Zr(p,X)^{93}Y reactions. Due to the stable proton beam irradiation, well-established beam profile monitoring system, and many efforts on detailed analysis, the experimental uncertainties were reduced. The measured data agreed with the previously measured data within experimental uncertainty except for some discrepancies: cross sections of ^{55}Mn(p,X)^{54}Mn, ^{59}Co(p,X)^{58}Co, and $^{\mathrm{nat}}$Ni(p,X)^{58}Co reactions were quite different between the present data and previous data. This disagreement is considered to be caused by the corrections for the secondary particles generated in the target stack. This work used thinner target stack than used in the previous studies. The correction made in this work is smaller than those in the previous works. Therefore, our data are considered to have more accuracy than the previous data. The measured data are useful for the evaluation of nuclear data.

For the benchmark, the measured data were compared with model-based calculations by spallation reaction models (INCL4.6/GEM, Bertini/GEM, JAM/GEM, and INCL++/ABLA07 version 6.28) and with the evaluated data (from the nuclear data library JENDL/HE-2007). All the reaction models and JENDL/HE-2007 generally reproduce the incident energy dependence of the experimental data: the cross sections for light products increase as the incident proton energy increases, and those for the medium-heavy products have a broad maximum around 1 GeV, and those for the heavy targets decreases with an increase of incident energy. However, some model prediction disagreed with the measured data by a factor equal to or greater than two. To investigate the prediction capabilities

quantitatively, the mean square deviation factor was introduced. The deviation factor indicated that none of the calculated or evaluated data meets the requirement accuracy of 30%. Therefore, improved spallation reaction modes are required.

4.2 Suggestion for Future Work

This work validated the DEURACS prediction capabilities for DDTTNYs at an emission angle of 0°. The neutron spectra at an emission angle of 0° are very important to evaluate the neutron source performance. However, the validation at the larger emission angles is also needed for the dose assessment and shielding design of deuteron accelerator-based neutron sources. Therefore, further measurements of double-differential neutron yields or double-differential cross sections are to be performed, and the validation of DEURACS should be performed.

In the experiment of nuclide production cross section, some corrections were made using transport calculations by PHITS. It is very difficult to estimate uncertainties caused by corrections done by PHITS calculation, e.g., nuclide production by secondary particles, and incoming and escape loss of light products. For the correction concerning secondary particle and incoming and escape loss, the energy-angle-double-differential cross sections of proton, neutron and light products such as ^{7}Be are required.

For the reliable assessment of nuclide production yields for spallation neutron source, improved spallation reaction models are required. Another approach is interpolation of experimental data. In both cases, accurate experimental data play fundamental and important roles. To improve the reaction models, optimizing the physical parameters used in the models and more precise description of nuclear reactions are necessary. To achieve these improvements, experimental data with small uncertainties are essential. Therefore, further measurements of the accurate data in J-PARC are desired for a wide range of target atomic numbers.

Acknowledgements

This work carried out at the Department of Advanced Energy Engineering Science, Interdisciplinary Graduate School of Engineering Sciences, Kyushu University, under the supervision of Professor Yukinobu Watanabe. This thesis would not be accomplished without the support of many people and I would like to express my sincere thanks to all of them.

First and foremost I am extremely grateful to my supervisor Professor Yukinobu Watanabe for his invaluable advice, continuous support, and constant encouragement. I could learned a lot from him in my five-year laboratory life.

I would like to express my appreciation to Professor Nobuo Ikeda (Department of Applied Quantum Physics and Nuclear Engineering) and Professor Hironao Sakaki (Department of Advanced Energy Engineering Science, and National Institutes for Quantum Science and Technology) for reviewing and giving helpful comments on this thesis.

I am also grateful to Associate Professor Takashi Teranishi (Department of Physics), Associate Professor Tamaki Yoshioka (Research Center for Advanced Particle Physics), Dr. Masaomi Tanaka (Reserch Center for Superheavy Elements), Nobuhiro Shigyo (Department of Applied Quantum Physics and Nuclear Engineering), Associate Professor Tadahiro Kin (Department of Advanced Energy Engineering Science), Dr. Keita Nakano (Japan Atomic Energy Agency), Dr. Seiya Manabe (National Institute of Advanced Industrial Science and Technology), Katsumi Aoki, Naoto Araki, Kosuke Yoshinami, Dr. Jun Koga, and So Makise for cooperation in the experiment carried out at Center for Accelerator and Beam Applied Science, Kyushu University. Without their support, this thesis would not be possible.

I am deeply grateful to Dr. Fujio Maekawa (Japan Atomic Energy Agency), Dr. Shin-ichiro Meigo (Japan Atomic Energy Agency), Dr. Hiroki Iwamoto (Japan Atomic Energy Agency), and Dr. Hiroki Matsuda (National Institutes for Quantum Science and Technology) for taking care of me during my stay at J-PARC and cooperating in the experiment carried out at J-PARC. I would like to make the most of what I have learned from them.

Special thanks to Dr. Shinsuke Nakayama (Japan Atomic Energy Agency), Dr. Shouhei Araki (Japan Atomic Energy Agency). They gave me advice about my future path. Thanks to their advice, I could decide to study in doctoral course and accomplish this thesis.

I'm deeply indebted to Assistant Professor Shoichiro Kawase. His advice and discussion always support my research.

Many thanks to past and present Watanabe-Kin Laboratory members. Thanks to them, I could enjoyed laboratory life.

Finally, I would like to express my gratitude to my friends, family, and rabbits Chirol and Kukuri. Without their supports, I could not complete this work.

This work was partially funded by ImPACT Program of Council for Science, Technology and Innovation (Cabinet Office, Government of Japan). This work was partially supported by Q-Energy Innovator Fellowship, Kyushu University. This paper includes results obtained with the Subsidy for Research and Development on Nuclear Transmutation Technology.

References

[1] J. Chadwick, "Possible existence of a neutron," *Nature*, vol. 129, no. 3252, pp. 312–312, Feb. 1932, ISSN: 1476-4687. DOI: 10.1038/129312a0.

[2] J. Chadwick, "The existence of a neutron," *Proceedings of the Royal Society of London. Series A, Containing Papers of a Mathematical and Physical Character*, vol. 136, no. 830, pp. 692–708, 1932.

[3] I. S. Shlimak, "Neutron transmutation doping in semiconductors: Science and applications," *Physics of the Solid State*, vol. 41, no. 5, pp. 716–719, May 1999, ISSN: 1090-6460. DOI: 10.1134/1.1130856.

[4] T. Kin, T. Kawagoe, S. Araki, and Y. Watanabe, "Production of high-purity medical radio isotope ^{64}Cu with accelerator-based neutrons generated with 9 and 12 MeV deuterons," *Journal of Nuclear Science and Technology*, vol. 54, no. 10, pp. 1123–1130, 2017.

[5] T. Kin, Y. Nagai, N. Iwamoto, F. Minato, O. Iwamoto, Y. Hatsukawa, M. Segawa, H. Harada, C. Konno, K. Ochiai, and K. Takakura, "New production routes for medical isotopes ^{64}Cu and ^{67}Cu using accelerator neutrons," *Journal of the Physical Society of Japan*, vol. 82, no. 3, p. 034 201, 2013. DOI: 10.7566/JPSJ.82.034201.

[6] R. F. Barth and J. C. Grecula, "Boron neutron capture therapy at the crossroads-where do we go from here?" *Applied Radiation and Isotopes*, p. 109 029, 2019.

[7] H. Okuno, H. Sakurai, Y. Mori, R. Fujita, and M. Kawashima, "Proposal of a 1-ampere-class deuteron single-cell linac for nuclear transmutation," *Proceedings of the Japan Academy, Series B*, vol. 95, no. 7, pp. 430–439, 2019. DOI: 10.2183/pjab.95.030.

[8] K. Tsujimoto, T. Sasa, K. Nishihara, T. Takizuka, and H. Takano, "Accelerator-driven system for transmutation of high-level waste," *Progress in Nuclear Energy*, vol. 37, no. 1, pp. 339–344, 2000, Global Environment and Nuclear Energy Systems-3 Proceedings of the Third International Symposium, ISSN: 0149-1970. DOI: https://doi.org/10.1016/S0149-1970(00)00068-8.

[9] M. Matsubayashi, A. Tsuruno, and Y. Horiguchi, "Jrr-3 neutron radiography facility," Japan, Tech. Rep., 1992, JAERI-M–92-028, pp. 600–607.

[10] T. Yoshiie, Y. Hayashi, S. Yanagita, Q. Xu, Y. Satoh, H. Tsujimoto, T. Kozuka, K. Kamae, K. Mishima, S. Shiroya, K. Kobayashi, M. Utsuro, and Y. Fujita, "A new materials irradiation facility at the Kyoto university reactor," *Nuclear Instruments and Methods in Physics Research Section A: Accelerators, Spectrometers, Detectors and Associated Equipment*, vol. 498, no. 1, pp. 522–531, 2003, ISSN: 0168-9002. DOI: https://doi.org/10.1016/S0168-9002(02)02143-5.

[11] Y. Kiyanagi, "Neutron applications developing at compact accelerator-driven neutron sources," *AAPPS Bulletin*, vol. 31, no. 1, p. 22, Sep. 2021, ISSN: 2309-4710. DOI: 10.1007/s43673-021-00022-3.

[12] B. Bayanov, V. Belov, E. Bender, M. Bokhovko, G. Dimov, V. Kononov, O. Kononov, N. Kuksanov, V. Palchikov, V. Pivovarov, R. Salimov, G. Silvestrov, A. Skrinsky, N. Soloviov, and S. Taskaev, "Accelerator-based neutron source for the neutron-capture and fast neutron therapy at hospital," *Nuclear Instruments and Methods in Physics Research Section A: Accelerators, Spectrometers, Detectors and Associated Equipment*, vol. 413, no. 2, pp. 397–426, 1998, ISSN: 0168-9002. DOI: https://doi.org/10.1016/S0168-9002(98)00425-2.

[13] T. A. Gabriel, J. R. Haines, and T. J. McManamy, "Overview of the Spallation Neutron Source (SNS) with emphasis on target systems," *Journal of Nuclear Materials*, vol. 318, pp. 1–13, 2003, Fifth International Workshop on Spallation Materials Technology, ISSN: 0022-3115. DOI: https://doi.org/10.1016/S0022-3115(03)00010-2.

[14] H. Tatsumoto, D. Lyngh, Y. Beßler, M. Klaus, F. Hanusch, P. Arnold, and H. Quack, "Design status of the ESS cryogenic moderator system," *IOP Conference Series: Materials Science and Engineering*, vol. 755, p. 012 101, Jun. 2020. DOI: 10.1088/1757-899x/755/1/012101.

[15] J. Wei, H. Chen, Y. Chen, Y. Chen, Y. Chi, C. Deng, H. Dong, L. Dong, S. Fang, J. Feng, S. Fu, L. He, W. He, Y. Heng, K. Huang, X. Jia, W. Kang, X. Kong, J. Li, T. Liang, G. Lin, Z. Liu, H. Ouyang, Q. Qin, H. Qu, C. Shi, H. Sun, J. Tang, J. Tao, C. Wang, F. Wang, D. Wang, Q. Wang, S. Wang, T. Wei, J. Xi, T. Xu, Z. Xu, W. Yin, X. Yin, J. Zhang, Z. Zhang, Z. Zhang, M. Zhou, and T. Zhu, "China Spallation Neutron Source: Design, R&D, and outlook," *Nuclear Instruments and Methods in Physics Research Section A: Accelerators, Spectrometers, Detectors and Associated Equipment*, vol. 600, no. 1, pp. 10–13, 2009, ISSN: 0168-9002. DOI: https://doi.org/10.1016/j.nima.2008.11.017.

[16] Y. Iwamoto, M. Hagiwara, D. Satoh, H. Iwase, H. Yashima, T. Itoga, T. Sato, Y. Nakane, H. Nakashima, Y. Sakamoto, T. Matsumoto, A. Masuda, J. Nishiyama, A. Tamii, K. Hatanaka, C. Theis, E. Feldbaumer, L. Jaegerhofer, C. Pioch, V. Mares, and T. Nakamura, "Quasi-monoenergetic neutron energy spectra for 246 and 389 MeV ^{7}Li(p, n) reactions at angles from 0° to 30°," *Nuclear Instruments and Methods in Physics Research Section A: Accelerators, Spectrometers, Detectors and Associated Equipment*, vol. 629, no. 1, pp. 43–49, 2011, ISSN: 0168-9002. DOI: https://doi.org/10.1016/j.nima.2010.12.022.

[17] S. Meigo, H. Takada, S. Chiba, T. Nakamoto, K. Ishibashi, N. Matsufuji, K. Maehata, N. Shigyo, Y. Watanabe, and M. Numajiri, "Measurements of neutron spectra produced from a thick lead target bombarded with 0.5- and 1.5-gev protons," *Nuclear Instruments and Methods in Physics Research Section A: Accelerators, Spectrometers, Detectors and Associated Equipment*, vol. 431, no. 3, pp. 521–530, 1999, ISSN: 0168-9002. DOI: https://doi.org/10.1016/S0168-9002(99)00282-X.

[18] Y. Uwamino, T. Ohkubo, A. Torii, and T. Nakamura, "Semi-monoenergetic neutron field for activation experiments up to 40 MeV," *Nuclear Instruments and Methods in Physics Research Section A: Accelerators, Spectrometers, Detectors and Associated Equipment*, vol. 271, no. 3, pp. 546–552, 1988, ISSN: 0168-9002. DOI: https://doi.org/10.1016/0168-9002(88)90318-X.

[19] M. Saltmarsh, C. Ludemann, C. Fulmer, and R. Styles, "Characteristics of an intense neutron source based on the d+Be reaction," *Nuclear Instruments and Methods*, vol. 145, no. 1, pp. 81–90, 1977, ISSN: 0029-554X. DOI: https://doi.org/10.1016/0029-554X(77)90559-6.

[20] A. Moeslang, V. Heinzel, H. Matsui, and M. Sugimoto, "The IFMIF test facilities design," *Fusion Engineering and Design*, vol. 81, no. 8-14, pp. 863–871, 2006.

[21] M. Fadil and B. Rannou, "About the production rates and the activation of the uranium carbide target for SPIRAL 2," English, *Nuclear Inst. and Methods in Physics Research, B*, vol. 266, no. 19-20, pp. 4318–4321, 2008. DOI: 10.1016/j.nimb.2008.05.138.

[22] S. Peng, F. Zhu, Z. Wang, Y. Gao, and Z. Guo, "The deuteron accelerator preliminary design for BISOL," English, *Nuclear Instruments and Methods in Physics Research Section B: Beam Interactions with Materials and Atoms*, vol. 376, no. C, pp. 420–424, 2016. DOI: 10.1016/j.nimb.2016.01.008.

[23] A. B. Smith, P. R. Fields, and J. H. Roberts, "Spontaneous fission neutron spectrum of Cf^{252}," *Phys. Rev.*, vol. 108, pp. 411–413, 2 Oct. 1957. DOI: 10.1103/PhysRev.108.411.

[24] T. Sato, Y. Iwamoto, S. Hashimoto, T. Ogawa, T. Furuta, S.-i. Abe, T. Kai, P.-E. Tsai, N. Matsuda, H. Iwase, N. Shigyo, L. Sihver, and K. Niita, "Features of Particle and Heavy Ion Transport code System (PHITS) version 3.02," *Journal of Nuclear Science and Technology*, vol. 55, no. 6, pp. 684–690, 2018. DOI: 10.1080/00223131.2017.1419890.

[25] S. Agostinelli, J. Allison, K. Amako, J. Apostolakis, H. Araujo, P. Arce, M. Asai, D. Axen, S. Banerjee, G. Barrand, F. Behner, L. Bellagamba, J. Boudreau, L. Broglia, A. Brunengo, H. Burkhardt, S. Chauvie, J. Chuma, R. Chytracek, G. Cooperman, G. Cosmo, P. Degtyarenko, A. Dell'Acqua, G. Depaola, D. Dietrich, R. Enami, A. Feliciello, C. Ferguson, H. Fesefeldt, G. Folger, F. Foppiano, A. Forti, S. Garelli, S. Giani, R. Giannitrapani, D. Gibin, J. Gomez Cadenas, I. Gonzalez, G. Gracia Abril, G. Greeniaus, W. Greiner, V. Grichine, A. Grossheim, S. Guatelli, P. Gumplinger, R. Hamatsu, K. Hashimoto, H. Hasui, A. Heikkinen, A. Howard, V. Ivanchenko, A. Johnson, F. Jones, J. Kallenbach, N. Kanaya, M. Kawabata, Y. Kawabata, M. Kawaguti, S. Kelner, P. Kent, A. Kimura, T. Kodama, R. Kokoulin, M. Kossov, H. Kurashige, E. Lamanna, T. Lampen, V. Lara, V. Lefebure, F. Lei, M. Liendl, W. Lockman, F. Longo, S. Magni, M. Maire, E. Medernach, K. Minamimoto, P. Mora de Freitas, Y. Morita, K. Murakami, M. Nagamatu, R. Nartallo, P. Nieminen, T. Nishimura, K. Ohtsubo, M. Okamura, S. O'Neale, Y. Oohata, K. Paech, J. Perl, A. Pfeiffer, M. Pia, F. Ranjard, A. Rybin, S. Sadilov, E. Di Salvo, G. Santin, T. Sasaki, N. Savvas, Y. Sawada, S. Scherer, S. Sei, V. Sirotenko, D. Smith, N. Starkov, H. Stoecker, J. Sulkimo, M. Takahata, S. Tanaka, E. Tcherniaev, E. Safai Tehrani, M. Tropeano, P. Truscott, H. Uno, L. Urban, P. Urban, M. Verderi, A. Walkden, W. Wander, H. Weber, J. Wellisch, T. Wenaus, D. Williams, D. Wright, T. Yamada, H. Yoshida, and D. Zschiesche, "Geant4 a simulation toolkit," *Nuclear Instruments and Methods in Physics Research Section A: Accelerators, Spectrometers, Detectors and Associated Equipment*, vol. 506, no. 3, pp. 250–303, 2003, ISSN: 0168-9002. DOI: https://doi.org/10.1016/S0168-9002(03)01368-8.

[26] A. Koning, D. Rochman, J.-C. Sublet, N. Dzysiuk, M. Fleming, and S. van der Marck, "TENDL: Complete Nuclear Data Library for Innovative Nuclear Science and Technology," *Nuclear Data Sheets*, vol. 155, pp. 1–55, 2019, Special Issue on Nuclear Reaction Data, ISSN: 0090-3752. DOI: https://doi.org/10.1016/j.nds.2019.01.002.

[27] A. Koning and D. Rochman, "Modern nuclear data evaluation with the talys code system," *Nuclear Data Sheets*, vol. 113, no. 12, pp. 2841–2934, 2012, Special Issue on Nuclear Reaction Data, ISSN: 0090-3752.

[28] M. Chadwick, M. Herman, P. Oblo?insky, M. Dunn, Y. Danon, A. Kahler, D. Smith, B. Pritychenko, G. Arbanas, R. Arcilla, R. Brewer, D. Brown, R. Capote, A. Carlson, Y. Cho, H. Derrien, K. Guber, G. Hale, S. Hoblit, S. Holloway, T. Johnson, T. Kawano, B. Kiedrowski, H. Kim, S. Kunieda, N. Larson, L. Leal, J. Lestone, R. Little, E. McCutchan, R. MacFarlane, M. MacInnes, C. Mattoon, R. McKnight, S. Mughabghab, G. Nobre, G. Palmiotti, A. Palumbo, M. Pigni, V. Pronyaev, R. Sayer, A. Sonzogni, N. Summers, P. Talou, I. Thompson, A. Trkov, R. Vogt, S. van der Marck, A. Wallner, M. White, D. Wiarda, and P. Young, "Endf/b-vii.1 nuclear data for science and technology: Cross sections, covariances, fission product yields and decay data," *Nuclear Data Sheets*, vol. 112, no. 12, pp. 2887–2996, 2011, Special Issue on ENDF/B-VII.1 Library, ISSN: 0090-3752. DOI: https://doi.org/10.1016/j.nds.2011.11.002.

[29] S. Nakayama, H. Kouno, Y. Watanabe, O. Iwamoto, and K. Ogata, "Theoretical model analysis of (d, xn) reactions on ^{9}Be and ^{12}C at incident energies up to 50 MeV," *Physical Review C*, vol. 94, no. 1, p. 014 618, 2016.

[30] S. Araki, Y. Watanabe, M. Kitajima, H. Sadamatsu, K. Nakano, T. Kin, Y. Iwamoto, D. Satoh, M. Hagiwara, H. Yashima, and T. Shima, "Systematic measurement of double-differential neutron production cross sections for deuteron-induced reactions at an incident energy of 102MeV," *Nuclear Instruments and Methods in Physics Research Section A: Accelerators, Spectrometers, Detectors and Associated Equipment*, vol. 842, pp. 62–70, 2017, ISSN: 0168-9002.

[31] H. Sadamatsu, Y. Watanabe, K. Nakano, S. Kawase, T. Kin, S. Araki, Y. Iwamoto, D. Satoh, M. Hagiwara, H. Yashima, *et al.*, "Systematic measurement of double-differential (d, xn) cross sections at an incident energy of 200 MeV," *JAEA-Conf 2018-001*, pp. 131–136, 2018.

[32] S. Nakayama, O. Iwamoto, Y. Watanabe, and K. Ogata, "JENDL/DEU-2020: Deuteron nuclear data library for design studies of accelerator-based neutron sources," *Journal of Nuclear Science and Technology*, vol. 58, no. 7, pp. 805–821, 2021. DOI: 10.1080/00223131.2020.1870010.

[33] A. Boudard, J. Cugnon, J.-C. David, S. Leray, and D. Mancusi, "New potentialities of the Liège intranuclear cascade model for reactions induced by nucleons and light charged particles," *Phys. Rev. C*, vol. 87, p. 014 606, 1 Jan. 2013.

[34] S. Kunieda, O. Iwamoto, N. Iwamoto, F. Minato, T. Okamoto, T. Sato, H. Nakashima, Y. Iwamoto, H. Iwamoto, F. Kitatani, T. Fukahori, Y. Watanabe, N. Shigyo, and S. Chiba, "Overview of JENDL-4.0/HE and benchmark calculation," Tech. Rep., 2016, pp. 41–46.

[35] Y. Watanabe, T. Fukahori, K. Kosako, N. Shigyo, T. Murata, N. Yamano, T. Hino, K. Maki, H. Nakashima, N. Odano, and S. Chiba, "Nuclear data evaluations for JENDL high-energy file," *AIP Conference Proceedings*, vol. 769, no. 1, pp. 326–331, 2005. DOI: 10.1063/1.1945015.

[36] H. Iwamoto, "Generation of nuclear data using gaussian process regression," *Journal of Nuclear Science and Technology*, vol. 57, no. 8, pp. 932–938, 2020. DOI: 10.1080/00223131.2020.1736202.

[37] M. Drosg and D. M. Drake, "Neutron emission spectra of triton beams of 20.22-MeV fully stopped in targets of H_2O, D_2O, LiF, Si, Ni, Mo, Ta, W, Pt, and Au," *Nuclear Science and Engineering*, vol. 182, no. 2, pp. 256–260, 2016.

[38] N. Shigyo, K. Hidaka, K. Hirabayashi, Y. Nakamura, D. Moriguchi, M. Kumabe, H. Hirano, S. Hirayama, Y. Naitou, C. Motooka, C. Lan, T. Watanabe, Y. Watanabe, K. Sagara, S. Maebaru, H. Sakaki, and H. Takahashi, "Measurement of deuteron induced thick target neutron yields at 9 MeV," *J.Korean Phys.Soc.*, vol. 59, 1725s, 2011.

[39] Y. Tajiri, Y. Watanabe, N. Shigyo, K. Hirabayashi, T. Nishizawa, and K. Sagara, "Measurement of double differential neutron yields from thick carbon target irradiated by 5-MeV and 9-MeV deuterons," *Progress in Nuclear Science and Technology*, vol. 4, pp. 582–586, 2014.

[40] K. Hirabayashi, T. Nishizawa, H. Uehara, H. Hirano, T. Kajimoto, N. Shigyo, M. Maeda, T. Yasumune, K. Maehata, Y. Tajiri, *et al.*, "Measurement of neutron yields from thick Al and SUS304 targets bombarded by 5-MeV and 9-MeV deuterons," *Progress in Nuclear Science and Technology*, vol. 3, pp. 60–64, 2012.

[41] S. Araki, Y. Watanabe, T. Kin, N. Shigyo, and K. Sagara, "Measurement of double differential neutron yields from thick aluminum target irradiated by 9 MeV deuteron," *Energy Procedia*, vol. 71, pp. 197–204, 2015, The Fourth International Symposium on Innovative Nuclear Energy Systems, INES-4, ISSN: 1876-6102.

[42] S. Nakayama, N. Furutachi, O. Iwamoto, and Y. Watanabe, "Role of breakup processes in deuteron-induced spallation reactions at 100–200 MeV/nucleon," *Physical Review C*, vol. 98, no. 4, p. 044 606, 2018.

[43] S. Nakayama, O. Iwamoto, and Y. Watanabe, "Consistent description of light composite particle emission in deuteron-induced reactions," *Physical Review C*, vol. 100, no. 4, p. 044 603, 2019.

[44] M. Yahiro, K. Ogata, T. Matsumoto, and K. Minomo, "The continuum discretized coupled-channels method and its applications," *Progress of Theoretical and Experimental Physics*, vol. 2012, no. 1, Sep. 2012, 01A206, ISSN: 2050-3911.

[45] Y. Iseri, M. Yahiro, and M. Kamimura, "Chapter IV. Coupled-Channels Approach to Deuteron and ^{3}He Breakup Reactions," *Progress of Theoretical Physics Supplement*, vol. 89, pp. 84–117, Apr. 1986, ISSN: 0375-9687. DOI: 10.1143/PTPS.89.84.

[46] G. Ohlsen, "Kinematic relations in reactions of the form A+B→C+D+E," *Nuclear Instruments and Methods*, vol. 37, pp. 240–248, 1965.

[47] T. Ye, S. Hashimoto, Y. Watanabe, K. Ogata, and M. Yahiro, "Analysis of inclusive (d, xp) reactions on nuclei from ^{9}Be to ^{238}U at 100 MeV," *Phys. Rev. C*, vol. 84, Nov. 2011.

[48] O. Iwamoto, N. Iwamoto, S. Kunieda, F. Minato, and K. Shibata, "The ccone code system and its application to nuclear data evaluation for fission and other reactions," *Nuclear Data Sheets*, vol. 131, pp. 259–288, 2016, Special Issue on Nuclear Reaction Data, ISSN: 0090-3752.

[49] C. Kalbach, "Two-component exciton model: Basic formalism away from shell closures," *Phys. Rev. C*, vol. 33, pp. 818–833, 3 Mar. 1986. DOI: 10.1103/PhysRevC.33.818.

[50] W. Hauser and H. Feshbach, "The inelastic scattering of neutrons," *Phys. Rev.*, vol. 87, pp. 366–373, 2 Jul. 1952. DOI: 10.1103/PhysRev.87.366.

[51] A. Koning and M. Duijvestijn, "A global pre-equilibrium analysis from 7 to 200 MeV based on the optical model potential," *Nuclear Physics A*, vol. 744, pp. 15–76, 2004, ISSN: 0375-9474. DOI: https://doi.org/10.1016/j.nuclphysa.2004.08.013.

[52] A. Koning, S. Hilaire, and S. Goriely, "User manual of TALYS-1.8," *Nuclear Research and Consultancy Group, Petten, The Netherlands*, 2015.

[53] A. Koning and J. Akkermans, "Randomness in multi-step direct reactions," *Annals of Physics*, vol. 208, no. 1, pp. 216–250, 1991, ISSN: 0003-4916. DOI: https://doi.org/10.1016/0003-4916(91)90345-9.

[54] C. Kalbach, "Systematics of continuum angular distributions: Extensions to higher energies," *Phys. Rev. C*, vol. 37, pp. 2350–2370, 6 Jun. 1988. DOI: 10.1103/PhysRevC.37.2350.

[55] A. Boudard, J. Cugnon, J.-C. David, S. Leray, and D. Mancusi, "New potentialities of the Liège intranuclear cascade model for reactions induced by nucleons and light charged particles," *Phys. Rev. C*, vol. 87, p. 014 606, 1 2013. DOI: 10.1103/PhysRevC.87.014606.

[56] K. Niita, S. Chiba, T. Maruyama, T. Maruyama, H. Takada, T. Fukahori, Y. Nakahara, and A. Iwamoto, "Analysis of the (N, xN') reactions by quantum molecular dynamics plus statistical decay model," *Phys. Rev. C*, vol. 52, pp. 2620–2635, 5 Nov. 1995.

[57] S. Furihata, "Statistical analysis of light fragment production from medium energy proton-induced reactions," *Nuclear Instruments and Methods in Physics Research Section B: Beam Interactions with Materials and Atoms*, vol. 171, no. 3, pp. 251–258, 2000, ISSN: 0168-583X. DOI: 10.1016/s0168-583x(00)00332-3.

[58] *INCL the Liège Intranuclear Cascade Model*, https://irfu.cea.fr/dphn/Spallation/incl.html.

[59] A. Gilbert and A. G. W. Cameron, "A composite nuclear-level density formula with shell corrections," *Canadian Journal of Physics*, vol. 43, no. 8, pp. 1446–1496, 1965. DOI: 10.1139/p65-139.

[60] *Eljen technology*, https://eljentechnology.com/products/liquid-scintillators/ej-301-ej-309.

[61] J. F. Ziegler, M. Ziegler, and J. Biersack, "Srim-the stopping and range of ions in matter (2010)," *Nuclear Instruments and Methods in Physics Research Section B: Beam Interactions with Materials and Atoms*, vol. 268, no. 11, pp. 1818–1823, 2010, 19th International Conference on Ion Beam Analysis, ISSN: 0168-583X.

[62] G. Dietze and H. Klein, "Gamma-calibration of NE 213 scintillation counters," *Nuclear Instruments and Methods in Physics Research*, vol. 193, no. 3, pp. 549–556, 1982, ISSN: 0167-5087.

[63] N. Nakao, T. Nakamura, M. Baba, Y. Uwamino, N. Nakanishi, H. Nakashima, and S.-i. Tanaka, "Measurements of response function of organic liquid scintillator for neutron energy range up to 135 MeV," *Nuclear Instruments and Methods in Physics Research Section A: Accelerators, Spectrometers, Detectors and Associated Equipment*, vol. 362, no. 2-3, pp. 454–465, 1995.

[64] R. Johnson, D. Ingersoll, B. Wehring, and J. Dorning, "NE-213 neutron spectrometry system for measurements from 1.0 to 20 MeV," *Nuclear Instruments and Methods*, vol. 145, no. 2, pp. 337–346, 1977, ISSN: 0029-554X.

[65] T. Adye, "Unfolding algorithms and tests using RooUnfold," in *Proceedings of the PHYSTAT 2011 Workshop, CERN, Geneva, Switzerland, CERN-2011-006*, 2011, pp. 313–318.

[66] G. D'Agostini, "A multidimensional unfolding method based on bayes' theorem," *Nuclear Instruments and Methods in Physics Research Section A: Accelerators, Spectrometers, Detectors and Associated Equipment*, vol. 362, no. 2, pp. 487–498, 1995, ISSN: 0168-9002. DOI: 10.1016/0168-9002(95)00274-X.

[67] A. Hocker and V. Kartvelishvili, "SVD approach to data unfolding," *Nuclear Instruments and Methods in Physics Research Section A: Accelerators, Spectrometers, Detectors and Associated Equipment*, vol. 372, no. 3, pp. 469–481, 1996, ISSN: 0168-9002. DOI: 10.1016/0168-9002(95)01478-0.

[68] D. Satoh, T. Sato, A. Endo, Y. Yamaguchi, M. Takada, and K. Ishibashi, "Measurement of response functions of a liquid organic scintillator for neutrons up to 800 MeV," *Journal of Nuclear Science and Technology*, vol. 43, pp. 714–719, Jul. 2006.

[69] D. Satoh, S. Kunieda, Y. Iwamoto, N. Shigyo, and K. Ishibashi, "Development of SCINFUL-QMD code to calculate the neutron detection efficiencies for liquid organic scintillator up to 3 GeV," *Journal of Nuclear Science and Technology*, vol. 39, no. sup2, pp. 657–660, 2002. DOI: 10.1080/00223131.2002.10875185.

[70] R. Cecil, B. Anderson, and R. Madey, "Improved predections of neutron detection efficiency for hydrocarbon scintillators from 1 MeV to about 300 MeV," *Nuclear Instruments and Methods*, vol. 161, no. 3, pp. 439–447, 1979, ISSN: 0029-554X.

[71] K. Weaver, J. Anderson, H. Barschall, and J. Davis, "Neutron spectra from deuteron bombardment of D, Li, Be, and C," *Nucl. Sci. Eng., v. 52, no. 1, pp. 35-45*, vol. 52, Sep. 1973.

[72] K. Minomo, K. Washiyama, and K. Ogata, "Deuteron-nucleus total reaction cross sections up to 1 GeV," *Journal of Nuclear Science and Technology*, vol. 54, no. 1, pp. 127–130, 2017.

[73] P. Kunz, "Computer code DWUCK4," *University of Colorado*, unpublished.

[74] K. Ogata and K. Yoshida, "Applicability of the continuum-discretized coupled-channels method to the deuteron breakup at low energies," *Phys. Rev. C*, vol. 94, p. 051 603, 5 Nov. 2016.

[75] J. R. Oppenheimer and M. Phillips, "Note on the transmutation function for deuterons," *Physical Review*, vol. 48, no. 6, p. 500, 1935.

[76] D. Hurst, R. Latham, and W. B. Lewis, "On the production of radium E and polonium by deuteron bombardment of bismuth," *Proceedings of the Royal Society of London. Series A. Mathematical and Physical Sciences*, vol. 174, no. 956, pp. 126–136, 1940.

[77] T. Sugawara, Y. Eguchi, H. Obayashi, H. Iwamoto, and K. Tsujimoto, "Conceptual design study of beam window for accelerator-driven system with subcriticality adjustment rod," *Nuclear Engineering and Design*, vol. 331, pp. 11–23, 2018, ISSN: 0029-5493. DOI: 10.1016/j.nucengdes.2018.02.011.

[78] R. Michel, M. Gloris, H.-J. Lange, I. Leya, M. Lupke, U. Herpers, B. Dittrich-Hannen, R. Rosel, T. Schiekel, D. Filges, P. Dragovitsch, M. Suter, H.-J. Hofmann, W. Wolfli, P. Kubik, H. Baur, and R. Wieler, "Nuclide production by proton-induced reactions on elements ($6 \leq Z \leq 29$) in the energy range from 800 to 2600 MeV," *Nuclear Instruments and Methods in Physics Research Section B: Beam Interactions with Materials and Atoms*, vol. 103, no. 2, pp. 183–222, 1995, ISSN: 0168-583X. DOI: 10.1016/0168-583X(95)00566-8.

[79] R. Michel, R. Bodemann, H. Busemann, R. Daunke, M. Gloris, H.-J. Lange, B. Klug, A. Krins, I. Leya, M. Lupke, S. Neumann, H. Reinhardt, M. Schnatz-Buttgen, U. Herpers, T. Schiekel, F. Sudbrock, B. Holmqvist, H. Conde, P. Malmborg, M. Suter, B. Dittrich-Hannen, P.-W. Kubik, H.-A. Synal, and D. Filges, "Cross sections for the production of residual nuclides by low- and medium-energy protons from the target elements C, N, O, Mg, Al, Si, Ca, Ti, V, Mn, Fe, Co, Ni, Cu, Sr, Y, Zr, Nb, Ba and Au," *Nuclear Instruments and Methods in Physics Research Section B: Beam Interactions with Materials and Atoms*, vol. 129, no. 2, pp. 153–193, 1997, ISSN: 0168-583X. DOI: 10.1016/S0168-583X(97)00213-9.

[80] Y. E. Titarenko, E. I. Karpikhin, A. F. Smolyakov, M. M. Igumnov, O. V. Shvedov, N. V. Stepanov, V. D. Kazarizki, V. F. Batyaev, S. G. Mashnik, and T. A. Gabriehl, "Experimental and calculative research of radioactive nuclei formation-products of target and constructional materials of electronuclear facilities irradiated by protons with energies 1.5 GeV and 130 MeV.," *Inst. Teoret. i Experiment. Fiziki, Moscow Repts*, p. 184, 1996.

[81] T. Schiekel, F. Sudbrock, U. Herpers, M. Gloris, H.-J. Lange, I. Leya, R. Michel, B. Dittrich-Hannen, H.-A. Synal, M. Suter, P. Kubik, M. Blann, and D. Filges, "Nuclide production by proton-induced reactions on elements ($6 \leq Z \leq 29$) in the energy range from 200 MeV to 400 MeV," *Nuclear Instruments and Methods in Physics Research Section B: Beam Interactions*

with Materials and Atoms, vol. 114, no. 1, pp. 91–119, 1996, ISSN: 0168-583X. DOI: 10.1016/0168-583X(96)00145-0.

[82] T. W. Armstrong and K. C. Chandler, "HETC: A high energy transport code," *Nuclear Science and Engineering*, vol. 49, no. 1, pp. 110–111, 1972. DOI: 10.13182/NSE72-A22535.

[83] L. S. Waters and R. E. Prael, "Status of the LAHET code system," Dec. 1995.

[84] S. Mashnik and A. Sierk, "CEM2k - recent developments in CEM," 2000.

[85] H. Matsuda, S. Meigo, and H. Iwamoto, "Proton-induced activation cross section measurement for aluminum with proton energy range from 0.4 to 3 GeV at J-PARC," *Journal of Nuclear Science and Technology*, vol. 55, no. 8, pp. 955–961, 2018. DOI: 10.1080/00223131.2018.1461694.

[86] H. Matsuda, H. Takeshita, S. Meigo, F. Maekawa, and H. Iwamoto, "Measurement of nuclide production cross-sections of ^{nat}Fe for 0.4–3.0 GeV protons in J-PARC," in *Proceedings of the 3rd J-PARC Symposium (J-PARC2019)*, 2021, p. 011 047.

[87] H. Matsuda, S.-i. Meigo, H. Iwamoto, and F. Maekawa, "Measurement of nuclide production cross section for lead and bismuth with proton in energy range from 0.4 GeV to 3.0 GeV," *EPJ Web Conf.*, vol. 239, p. 06 004, 2020. DOI: 10.1051/epjconf/202023906004.

[88] D. Mancusi, A. Boudard, J. Cugnon, J.-C. David, P. Kaitaniemi, and S. Leray, "Extension of the Liège intranuclear-cascade model to reactions induced by light nuclei," *Phys. Rev. C*, vol. 90, p. 054 602, 5 Nov. 2014. DOI: 10.1103/PhysRevC.90.054602.

[89] A. Kelić, M. V. Ricciardi, and K.-H. Schmidt, *ABLA07–towards a complete description of the decay channels of a nuclear system from spontaneous fission to multifragmentation*, 2009.

[90] H. W. Bertini, "Intranuclear-cascade calculation of the secondary nucleon spectra from nucleon-nucleus interactions in the energy range 340 to 2900 MeV and comparisons with experiment," *Phys. Rev.*, vol. 188, pp. 1711–1730, 4 Dec. 1969. DOI: 10.1103/PhysRev.188.1711.

[91] Y. Nara, N. Otuka, A. Ohnishi, K. Niita, and S. Chiba, "Relativistic nuclear collisions at 10A gev energies from p+Be to Au+Au with the hadronic cascade model," *Phys. Rev. C*, vol. 61, p. 024 901, 2 Dec. 1999. DOI: 10.1103/PhysRevC.61.024901.

[92] S. Nagamiya, "Introduction to J-PARC," *Progress of Theoretical and Experimental Physics*, vol. 2012, no. 1, Oct. 2012, 02B001, ISSN: 2050-3911. DOI: 10.1093/ptep/pts025.

[93] S. Meigo, F. Noda, S. Ishikura, M. Futakawa, S. Sakamoto, and Y. Ikeda, "Evaluation of the 3-GeV proton beam profile at the spallation target of the JSNS," *Nuclear Instruments and Methods in Physics Research Section A: Accelerators, Spectrometers, Detectors and Associated Equipment*, vol. 562, no. 2, pp. 569–572, 2006, Proceedings of the 7th International Conference on Accelerator Applications, ISSN: 0168-9002. DOI: 10.1016/j.nima.2006.02.011.

[94] S. Meigo, M. Ohi, T. Kai, T. Ono, K. Ikezaki, T. Haraguchi, H. Fujimori, and S. Sakamoto, "Beam commissioning for neutron and muon facility at J-PARC," *Nuclear Instruments and Methods in Physics Research Section A: Accelerators, Spectrometers, Detectors and Associated Equipment*, vol. 600, no. 1, pp. 41–43, 2009, ISSN: 0168-9002. DOI: 10.1016/j.nima.2008.11.068.

[95] S. Hiroki, N. Hayashi, M. Kawase, F. Noda, P. Saha, H. Sako, H. Takahashi, A. Ueno, Y. Arakida, S. Lee, *et al.*, "Multi-wire profile monitor for J-PARC 3 GeV RCS," *EPAC08, Genoa, Italy*, pp. 1131–1133, 2008.

[96] *Technical design report of spallation neutron source facility in J-PARC, JAEA-Tech. 2011-035.* 2012.

[97] E. Tomarchio and S. Rizzo, "Coincidence-summing correction equations in gamma-ray spectrometry with p-type HP Ge detectors," *Radiation Physics and Chemistry*, vol. 80, no. 3, pp. 318–323, 2011, ISSN: 0969-806X. DOI: 10.1016/j.radphyschem.2010.09.014.

[98] Y. Mizumoto, T. Kusakabe, and S. Iwata, "Ratio of peak to total efficiencies for germanium detectors," *Radioisotopes (Tokyo)*, vol. 36, no. 1, pp. 20–23, 1987.

[99] M. Berger, J. Hubbell, S. Seltzer, J. Chang, J. Coursey, D. Z. R. Sukumar, and K. Olsen, *XCOM: Photon cross sections database*, https://www.nist.gov/pml/xcom-photon-cross-sections-database, 1987.

[100] K. Shibata, O. Iwamoto, T. Nakagawa, N. Iwamoto, A. Ichihara, S. Kunieda, S. Chiba, K. Furutaka, N. Otuka, T. Ohsawa, T. Murata, H. Matsunobu, A. Zukeran, S. Kamada, and J. Katakura, "JENDL-4.0: A new library for nuclear science and engineering," *Journal of Nuclear Science and Technology*, vol. 48, no. 1, pp. 1–30, 2011. DOI: 10.1080/18811248.2011.9711675.

[101] G. Chiba, K. Okumura, K. Sugino, Y. Nagaya, K. Yokoyama, T. Kugo, M. Ishikawa, and S. Okajima, "JENDL-4.0 benchmarking for fission reactor applications," *Journal of Nuclear Science and Technology*, vol. 48, no. 2, pp. 172–187, 2011. DOI: 10.1080/18811248.2011.9711692.

[102] M. R. Bhat, "Evaluated nuclear structure data file (ENSDF)," in *Nuclear Data for Science and Technology*, S. M. Qaim, Ed., Berlin, Heidelberg: Springer Berlin Heidelberg, 1992, pp. 817–821.

[103] I. Leya, "Modelling of the interactions between galactic cosmic rays with stone and iron meteorites - thin-target irradiations and thick-target experiments," Ph.D. dissertation, Univ. Hannover, 1997.

[104] P. Kozma and B. Tumendemberel, "Nuclear reactions of medium and heavy target nuclei with high-energy projectiles," *Czechoslovak Journal of Physics*, vol. 40, pp. 29–37, 1 Jan. 1990. DOI: 10.1007/BF01598352.

[105] R. Michel, F. Peiffer, and R. Stuck, "Measurement and hybrid model analysis of integral excitation functions for proton-induced reactions on vanadium, manganese and cobalt up to 200 MeV," *Nuclear Physics A*, vol. 441, no. 4, pp. 617–639, 1985, ISSN: 0375-9474. DOI: 10.1016/0375-9474(85)90441-5.

[106] R. Michel, B. Dittrich, U. Herpers, F. Peiffer, T. Schiffmann, P. Cloth, P. Dragovitsch, and D. Filges, "Proton-induced spallation at 600 MeV," *Analyst*, vol. 114, pp. 287–293, 3 1989. DOI: 10.1039/AN9891400287.

[107] H. Weigel, R. Michel, U. Herpers, and W. Herr, "Survey of 600 MeV proton cross-sections for spallogenic radionuclides in quartz-, Fe-, Co-, and Ni-targets," *Radiochemical and Radioanalytical Letters*, vol. 21, no. 5, pp. 293–300, 1975.

[108] I. Haller and G. Rudstam, "Relative yields of the isomeric pairs ^{69g}Zn-^{69m}Zn and ^{52g}Mn-^{52m}Mn in some spallation reactions induced by 20–153 MeV protons," *Journal of Inorganic and Nuclear Chemistry*, vol. 19, no. 1, pp. 1–8, 1961, ISSN: 0022-1902. DOI: 10.1016/0022-1902(61)80038-9.

[109] O. V. Shvedov, Y. E. Titarenko, E. I. Karpikhin, I. V. Fedotov, V. D. Kazaritskiy, V. F. Batyaev, Y. V. Kochevalin, and N. V. Stepanov, "The experimental and theoretical investigations deep spallation cross section reaction on Co-59 by 1.2 GeV protons.," *Inst. Teoret. i Experiment. Fiziki, Moscow Repts*, no. 81-93, 1993.

[110] Y. Asano, S. Mori, M. Sakano, K. Katoh, K. Kondo, and M. Noguchi, "Nuclear reactions of Ti, Fe, Co, Ni, Cu, and Zn by 500-MeV protons," *Journal of the Physical Society of Japan*, vol. 60, no. 1, pp. 107–113, 1991. DOI: 10.1143/JPSJ.60.107.

[111] Y. E. Titarenko, "Experimental yields for Co-59 irradiated with 0.2, 1.2, 1.6 and 2.6-GeV protons," *USSR report to the I.N.D.C.*, no. 433, p. 91, 2003.

[112] Y. V. Aleksandrov, A. I. Bogdanov, S. K. Vasil'ev, R. B. Ivanov, M. A. Mikhaylova, T. I. Popova, and V. P. Prikhodtseva, "The radionuclide production by 1 GeV protons in the middle atomic weight elements," *Izv. Rossiiskoi Akademii Nauk, Ser. Fiz.*, vol. 54, p. 2249, 1990.

[113] G. Steyn, S. Mills, F. Nortier, B. Simpson, and B. Meyer, "Production of ^{52}Fe via proton-induced reactions on manganese and nickel," *International Journal of Radiation Applications and Instrumentation. Part A. Applied Radiation and Isotopes*, vol. 41, no. 3, pp. 315–325, 1990, ISSN: 0883-2889. DOI: 10.1016/0883-2889(90)90197-O.

[114] R. G. Korteling and A. Caretto, "Systematics of ^{24}Na and ^{22}Na production with 400 MeV protons," *Journal of Inorganic and Nuclear Chemistry*, vol. 29, no. 12, pp. 2863–2878, 1967, ISSN: 0022-1902. DOI: 10.1016/0022-1902(67)80117-9.

[115] A. Budzanowski, M. Fidelus, D. Filges, F. Goldenbaum, H. Hodde, L. Jarczyk, B. Kamys, M. Kistryn, S. Kistryn, S. Kliczewski, A. Kowalczyk, E. Kozik, P. Kulessa, H. Machner, A. Magiera, B. Piskor-Ignatowicz, K. Pysz, Z. Rudy, R. Siudak, and M. Wojciechowski, "Comparison of nonequilibrium processes in p+Ni and p+Au collisions at GeV energies," *Phys. Rev. C*, vol. 82, p. 034 605, 3 Sep. 2010. DOI: 10.1103/PhysRevC.82.034605.

[116] C.-M. Herbach, D. Hilscher, U. Jahnke, V. G. Tishchenko, J. Galin, A. Letourneau, A. Peghaire, D. Filges, F. Goldenbaum, L. Pienkowski, W. U. Schroder, and J. Toke, "Systematic investigation of 1.2-GeV proton-induced spallation reactions on targets between Al and U," *Nuclear Instruments and Methods in Physics Research Section A: Accelerators, Spectrometers, Detectors and Associated Equipment*, vol. 562, no. 2, pp. 729–732, 2006, Proceedings of the 7th International Conference on Accelerator Applications, ISSN: 0168-9002. DOI: https://doi.org/10.1016/j.nima.2006.02.033.

[117] E. Belmont and J. M. Miller, "Reactions of 370-MeV protons with cobalt," *Phys. Rev.*, vol. 95, pp. 1554–1561, 6 Sep. 1954. DOI: 10.1103/PhysRev.95.1554.

[118] G. M. Raisbeck and F. Yiou, "Production cross sections for ^{7}Be and ^{22}Na in targets of Si, Mg, Fe, and Ni irradiated by 1, 2, 3, and 23 GeV protons," *Phys. Rev. C*, vol. 12, pp. 915–920, 3 Sep. 1975. DOI: 10.1103/PhysRevC.12.915.

[119] G. V. S. Rayudu, "Formation cross sections of various radionuclides from Ni, Fe, Si, Mg, O, and C for protons of energies between 130 and 400 MeV," *Canadian Journal of Chemistry*, vol. 42, no. 5, pp. 1149–1154, 1964. DOI: 10.1139/v64-178.

[120] G. V. S. Rayudu, "Formation cross sections of various radionuclides from Ni, Fe, Si, Mg, O and C for protons of energies between 0.5 and 2.9 GeV," *Journal of Inorganic and Nuclear Chemistry*, vol. 30, no. 9, pp. 2311–2315, 1968, ISSN: 0022-1902. DOI: https://doi.org/10.1016/0022-1902(68)80239-8.

[121] H. Yashima, Y. Uwamino, H. Iwase, H. Sugita, T. Nakamura, S. Ito, and A. Fukumura, "Cross sections for the production of residual nuclides by high-energy heavy ions," *Nuclear Instruments and Methods in Physics Research Section B: Beam Interactions with Materials and Atoms*, vol. 226, no. 3, pp. 243–263, 2004, ISSN: 0168-583X. DOI: https://doi.org/10.1016/j.nimb.2004.06.025.

[122] J. Cline and E. Nieschmidt, "Measurements of spallation cross sections for 590 MeV protons on thin targets of copper, nickel, iron and aluminum," *Nuclear Physics A*, vol. 169, no. 2, pp. 437–448, 1971, ISSN: 0375-9474. DOI: https://doi.org/10.1016/0375-9474(71)90897-9.

[123] J. Sisterson and J. Vincent, "Cross section measurements for proton-induced reactions in Fe and Ni producing relatively short-lived radionuclides at *Ep*=140–500MeV," *Nuclear Instruments and Methods in Physics Research Section B: Beam Interactions with Materials and Atoms*, vol. 251, no. 1, pp. 1–8, 2006, ISSN: 0168-583X. DOI: https://doi.org/10.1016/j.nimb.2006.05.015.

[124] K. Chackett, "Yields of potassium isotopes in high energy bombardments of vanadium, iron, cobalt, nickel, copper and zinc," *Journal of Inorganic and Nuclear Chemistry*, vol. 27, no. 12, pp. 2493–2505, 1965, ISSN: 0022-1902. DOI: https://doi.org/10.1016/0022-1902(65)80148-8.

[125] L. B. Church and A. A. Caretto, "Study of (p, xn) reactions at 400 MeV," *Phys. Rev.*, vol. 178, pp. 1732–1742, 4 Feb. 1969. DOI: 10.1103/PhysRev.178.1732.

[126] S. Neumann, "Activation experiments with medium-energy neutrons and the production of cosmogenic nuclides in extraterrestrial matter," Ph.D. dissertation, Leibniz University Hannover, 1999.

[127] S. Regnier, B. Lavielle, M. Simonoff, and G. N. Simonoff, "Nuclear reactions in Rb, Sr, Y, and Zr targets," *Phys. Rev. C*, vol. 26, pp. 931–943, 3 Sep. 1982. DOI: 10.1103/PhysRevC.26.931.

[128] Y. Titarenko, V. Batyaev, A. Titarenko, M. Butko, K. Pavlov, S. Florya, R. Tikhonov, V. Zhivun, A. Ignatyuk, S. Mashnik, S. Leray, and A. Boudard, "Measurement and simulation of the cross sections for nuclide production in ^{93}Nb and ^{nat}Ni targets irradiated with 0.04- to 2.6 GeV protons," *Physics of Atomic Nuclei - PHYS ATOM NUCL-ENGL TR*, vol. 74, pp. 537–550, Apr. 2011. DOI: 10.1134/S106377881104017X.

[129] V. Zerkin and B. Pritychenko, "The experimental nuclear reaction data (EXFOR): Extended computer database and web retrieval system," *Nuclear Instruments and Methods in Physics Research Section A: Accelerators, Spectrometers, Detectors and Associated Equipment*, vol. 888, pp. 31–43, 2018, ISSN: 0168-9002. DOI: 10.1016/j.nima.2018.01.045.

[130] Y. Watanabe, K. Kosaka, S. Kunieda, S. Chiba, R. Fujimoto, H. Harada, M. Kawai, F. Maekawa, T. Murata, H. Nakashima, *et al.*, "Status of JENDL high energy file," *Journal of the Korean Physical Society*, vol. 59, pp. 1040–1045, 2 2011.

[131] K. Kosako, T. Fukahori, and Y. Watanabe, "Evaluations of K, Ca, Ti, V, Cr, Mn, Fe, Co, Ni, and Zn for JENDL/HE," *AIP Conference Proceedings*, vol. 769, no. 1, pp. 398–401, 2005. DOI: 10.1063/1.1945032.

[132] Y. E. Titarenko, O. V. Shvedov, V. F. Batyaev, E. I. Karpikhin, V. M. Zhivun, A. B. Koldobsky, R. D. Mulambetov, S. V. Kvasova, A. N. Sosnin, S. G. Mashnik, R. E. Prael, A. J. Sierk, T. A. Gabriel, M. Saito, and H. Yasuda, "Cross sections for nuclide production in 1 GeV proton-irradiated ^{208}Pb," *Phys. Rev. C*, vol. 65, p. 064 610, 6 May 2002. DOI: 10.1103/PhysRevC.65.064610.

[133] Y. E. Titarenko, V. F. Batyaev, A. Y. Titarenko, M. A. Butko, K. V. Pavlov, S. N. Florya, R. S. Tikhonov, S. G. Mashnik, A. V. Ignatyuk, N. N. Titarenko, W. Gudowski, M. T ě šıénský, C.-M. L. Persson, H. A. Abderrahim, H. Kumawat, and H. Duarte, "Cross sections for nuclide production in a ^{56}Fe target irradiated by 300, 500, 750, 1000, 1500, and 2600 MeV protons compared with data on a hydrogen target irradiated by 300, 500, 750, 1000, and 1500 MeV/nucleon ^{56}Fe ions," *Phys. Rev. C*, vol. 78, p. 034 615, 3 Sep. 2008. DOI: 10.1103/PhysRevC.78.034615.

[134] A. J. Koning, "Review of high energy data and model codes for accelerator-based transmutation," Netherlands, Tech. Rep., 1993, ECN-C–93-005, p. 135.

[135] Y. E. Titarenko, V. F. Batyaev, A. Titarenko, M. A. Butko, K. Pavlov, S. N. Florya, R. S. Tikhonov, V. M. Zhivun, A. Ignatyuk, S. Mashnik, S. Leray, A. Boudard, J. Cugnon, D. Mancusi, Y. Yariv, K. Nishihara, N. Matsuda, H. Kumawat, G. Mank, and W. Gudowski, "Measurement and

simulation of the cross sections for nuclide production in ^{nat}W and ^{181}Ta targets irradiated with 0.04- to 2.6-GeV protons," *Physics of Atomic Nuclei*, vol. 74, pp. 551–572, 2011.

A Nuclide Production Data

A.1 Cross Section Data

A.1.1 ^{55}Mn

Table A.1: Nuclide production cross sections of Mn by irradiation of 1.3-, 2.2-, and 3.0-GeV protons. Types "i" and "c" represent independent and cumulative cross sections, respectively. The uncertainty is given in the parenthesis below each cross section.

Product	Type	$T_{1/2}$	1.3 GeV [mb]	2.2 GeV [mb]	3.0 GeV [mb]
^{7}Be	i	53.22 d	5.20	7.18	10.0
			(0.13)	(0.16)	(0.2)
^{22}Na	c	2.6018 y	1.66	2.49	3.13
			(0.04)	(0.06)	(0.07)
^{24}Na	c	14.997 h	2.61	4.05	4.66
			(0.06)	(0.08)	(0.10)
^{28}Mg	c	20.915 h	0.374	0.520	0.590
			(0.011)	(0.013)	(0.015)
^{38}S	c	2.84 h	0.0851	0.103	0.0934
			(0.0079)	(0.008)	(0.0073)
^{41}Ar	c	1.83 h	1.26	1.29	1.31
			(0.04)	(0.03)	(0.04)
^{42}K	i	12.355 h	6.15	5.66	5.79
			(0.16)	(0.14)	(0.15)
^{43}K	c	22.3 h	2.42	2.20	2.41
			(0.06)	(0.05)	(0.06)
^{47}Ca	c	4.536 d	0.166	0.163	0.192
			(0.005)	(0.004)	(0.005)

Table A.1 – continued from previous page

Product	Type	$T_{1/2}$	1.3 GeV [mb]	2.2 GeV [mb]	3.0 GeV [mb]
^{43}Sc	c	3.891 h	4.21	3.55	3.71
			(0.18)	(0.15)	(0.15)
^{44g}Sc	i	3.97 h	7.43	6.66	6.76
			(0.19)	(0.15)	(0.17)
^{44m}Sc	i	58.61 h	6.91	6.35	6.30
			(0.17)	(0.15)	(0.15)
^{46}Sc	i	83.79 d	12.4	10.8	11.8
			(0.3)	(0.2)	(0.3)
^{47}Sc	c	3.3492 d	5.38	5.11	5.45
			(0.14)	(0.17)	(0.14)
^{48}Sc	i	43.67 h	1.40	1.35	1.49
			(0.04)	(0.03)	(0.04)
^{48}V	c	15.974 d	12.9	11.6	12.2
			(0.3)	(0.2)	(0.3)
^{48}Cr	c	21.56 h	0.276	0.237	0.250
			(0.009)	(0.008)	(0.008)
^{51}Cr	c	27.704 d	28.6	26.4	30.2
			(0.7)	(0.6)	(0.7)
^{52}Mn	c	5.591 d	4.99	4.97	5.55
			(0.14)	(0.13)	(0.15)
^{54}Mn	i	312.2 d	52.0	52.5	62.7
			(1.5)	(1.4)	(1.8)
^{52}Fe	c	8.275 h	0.0268	—	0.0230
			(0.0025)		(0.0020)

A.1.2 ^{59}Co

Table A.2: Same as Table A.1, but for the Co target.

Product	Type	$T_{1/2}$	1.3 GeV [mb]	2.2 GeV [mb]	3.0 GeV [mb]
^{7}Be	i	53.22 d	4.77 (0.12)	6.71 (0.15)	9.28 (0.22)
^{22}Na	c	2.6018 y	1.44 (0.04)	2.37 (0.06)	2.94 (0.07)
^{24}Na	c	14.997 h	2.16 (0.09)	3.74 (0.13)	4.05 (0.17)
^{28}Mg	c	20.915 h	0.270 (0.007)	0.406 (0.010)	0.485 (0.011)
^{38}S	c	2.84 h	0.0607 (0.0055)	0.0709 (0.0050)	0.0770 (0.0078)
^{41}Ar	c	1.83 h	0.942 (0.027)	0.954 (0.024)	0.917 (0.027)
^{42}K	i	12.355 h	4.76 (0.12)	4.50 (0.11)	4.50 (0.11)
^{43}K	c	22.3 h	1.58 (0.04)	1.39 (0.03)	1.55 (0.03)
^{47}Ca	c	4.536 d	0.0908 (0.0035)	0.0771 (0.0027)	0.0894 (0.0027)
^{43}Sc	c	3.891 h	4.04 (0.16)	3.14 (0.12)	3.53 (0.14)
^{44g}Sc	i	3.97 h	6.90 (0.16)	6.01 (0.13)	6.01 (0.13)
^{44m}Sc	i	58.61 h	7.96 (0.17)	6.15 (0.13)	6.88 (0.14)
^{46}Sc	i	83.79 d	9.24 (0.20)	7.88 (0.17)	8.37 (0.18)
^{47}Sc	c	3.3492 d	3.39 (0.08)	2.99 (0.07)	3.17 (0.07)
^{48}Sc	i	43.67 h	0.703 (0.019)	0.646 (0.016)	0.661 (0.016)
^{48}V	c	15.974 d	13.4 (0.3)	11.5 (0.2)	11.6 (0.2)

Table A.2 – continued from previous page

Product	Type	$T_{1/2}$	1.3 GeV [mb]	2.2 GeV [mb]	3.0 GeV [mb]
^{48}Cr	c	21.56 h	0.393 (0.012)	0.309 (0.009)	0.326 (0.010)
^{51}Cr	c	27.704 d	26.1 (0.6)	21.7 (0.5)	24.0 (0.5)
^{52}Mn	c	5.591 d	8.74 (0.24)	7.97 (0.21)	7.56 (0.20)
^{54}Mn	i	312.2 d	24.4 (0.06)	22.5 (0.05)	24.7 (0.05)
^{56}Mn	c	2.5789 h	5.81 (0.20)	5.97 (0.19)	6.07 (0.21)
^{52}Fe	c	8.275 h	0.134 (0.006)	0.103 (0.04)	0.103 (0.04)
^{55}Co	c	17.53 h	0.939 (0.054)	0.838 (0.048)	0.910 (0.053)
^{56}Co	c	77.236 d	6.52 (0.15)	6.05 (0.13)	7.08 (0.16)
^{57}Co	c	271.74 d	23.9 (0.6)	23.1 (0.6)	26.5 (0.7)
^{58}Co	i	70.86 d	50.9 (1.1)	50.8 (1.1)	57.5 (1.2)
^{57}Ni	c	35.6 h	0.172 (0.007)	0.148 (0.006)	0.159 (0.006)

A.1.3 ^{nat}Ni

Table A.3: Same as Table A.1, but for the Ni target.

Product	Type	$T_{1/2}$	0.4 GeV [mb]	1.3 GeV [mb]	2.2 GeV [mb]	3.0 GeV [mb]
^{7}Be	i	53.22 d	1.27 (0.10)	6.76 (0.27)	10.5 (0.4)	12.6 (0.5)
^{22}Na	c	2.6018 y	0.274 (0.029)	2.12 (0.09)	3.36 (0.14)	3.88 (0.14)
^{24}Na	c	14.997 h	0.166 (0.017)	1.72 (0.12)	3.12 (0.17)	3.06 (0.18)
^{28}Mg	c	20.915 h	—	—	0.236 (0.016)	0.246 (0.016)
^{42}K	i	12.355 h	1.03 (0.09)	2.53 (0.15)	2.59 (0.14)	2.32 (0.14)
^{43}K	c	22.3 h	0.22 (0.02)	0.702 (0.036)	0.678 (0.029)	0.633 (0.026)
^{43}Sc	c	3.891 h	4.18 (0.26)	6.79 (0.39)	6.12 (0.37)	5.35 (0.33)
^{44g}Sc	i	3.97 h	5.39 (0.24)	8.09 (0.34)	7.48 (0.32)	6.62 (0.27)
^{44m}Sc	i	58.61 h	5.60 (0.24)	8.11 (0.32)	7.92 (0.32)	6.73 (0.24)
^{46}Sc	i	83.79 d	3.70 (0.16)	5.68 (0.21)	4.92 (0.19)	4.72 (0.16)
^{47}Sc	c	3.3492 d	1.00 (0.06)	1.44 (0.07)	1.48 (0.07)	1.34 (0.06)
^{48}Sc	i	43.67 h	—	0.187 (0.035)	0.372 (0.078)	0.216 (0.032)
^{48}V	c	15.9735 d	20.3 (0.8)	20.3 (0.8)	17.0 (0.7)	16.2 (0.6)
^{48}Cr	c	21.56 h	1.90 (0.09)	1.61 (0.07)	1.43 (0.07)	1.23 (0.05)
^{51}Cr	c	27.704 d	41.1 (1.6)	32.1 (1.2)	27.8 (1.1)	26.8 (0.9)
^{52}Mn	c	5.591 d	19.1 (0.8)	13.8 (0.6)	12.2 (0.5)	11.9 (0.5)

Table A.3 – continued from previous page

Product	Type	$T_{1/2}$	0.4 GeV [mb]	1.3 GeV [mb]	2.2 GeV [mb]	3.0 GeV [mb]
^{54}Mn	i	312.2 d	16.9	13.5	12.3	12.2
			(0.7)	(0.6)	(0.6)	(0.5)
^{52}Fe	c	8.275 h	2.03	1.19	1.21	1.05
			(0.12)	(0.06)	(0.09)	(0.05)
^{55}Co	c	17.53 h	13.4	8.99	8.37	7.98
			(0.9)	(0.60)	(0.56)	(0.51)
^{56}Co	c	77.236 d	38.3	29.4	27.5	28.5
			(1.6)	(1.2)	(1.1)	(1.0)
^{57}Co	c	271.74 d	67.8	63.0	62.9	62.9
			(2.9)	(2.9)	(2.7)	(2.4)
^{58}Co	i	70.86 d	16.6	18.1	18.3	19.4
			(0.7)	(0.7)	(0.7)	(0.7)
^{56}Ni	c	6.075 d	2.61	1.81	1.67	1.76
			(0.11)	(0.08)	(0.07)	(0.07)
^{57}Ni	c	35.6 h	27.5	21.0	21.8	21.7
			(1.4)	(1.0)	(1.1)	(1.0)

A.1.4 ^{nat}Zr

Table A.4: Same as Table A.1, but for the Zr target.

Product	Type	$T_{1/2}$	0.4 GeV [mb]	1.3 GeV [mb]	2.2 GeV [mb]	3.0 GeV [mb]
^{7}Be	i	53.22 d	0.621 (0.048)	3.95 (0.12)	6.89 (0.20)	9.16 (0.27)
^{22}Na	c	2.6018 y	0.229 (0.040)	0.476 (0.036)	1.06 (0.06)	1.67 (0.07)
^{24}Na	c	14.997 h	0.167 (0.095)	0.686 (0.100)	2.11 (0.12)	2.91 (0.16)
^{28}Mg	c	20.915 h	—	0.502 (0.056)	0.561 (0.064)	0.610 (0.056)
^{42}K	i	12.355 h	—	0.539 (0.130)	1.96 (0.14)	2.53 (0.14)
^{43}K	c	22.3 h	—	0.931 (0.035)	—	1.03 (0.03)
^{44g}Sc	i	3.97 h	—	—	1.25 (0.08)	1.66 (0.10)
^{44m}Sc	i	58.61 h	—	—	2.16 (0.06)	2.62 (0.07)
^{46}Sc	i	83.79 d	0.0341 (0.0071)	1.52 (0.04)	3.39 (0.09)	4.01 (0.10)
^{47}Sc	c	3.3492 d	—	—	1.84 (0.06)	1.99 (0.06)
^{48}Sc	i	43.67 h	—	—	1.00 (0.06)	0.786 (0.028)
^{48}V	c	15.9735 d	0.0394 (0.0034)	1.74 (0.05)	3.58 (0.10)	4.12 (0.10)
^{51}Cr	c	27.704 d	—	4.50 (0.15)	7.86 (0.23)	8.60 (0.22)
^{52}Mn	c	5.591 d	—	1.89 (0.07)	3.20 (0.10)	3.30 (0.10)
^{54}Mn	i	312.2 d	0.145 (0.012)	5.28 (0.16)	7.2 (0.2)	8.17 (0.21)
^{55}Co	c	17.53 h	—	0.243 (0.039)	0.463 (0.034)	0.380 (0.028)

Table A.4 – continued from previous page

Product	Type	$T_{1/2}$	0.4 GeV [mb]	1.3 GeV [mb]	2.2 GeV [mb]	3.0 GeV [mb]
^{56}Co	c	77.236 d	0.0435 (0.0053)	1.92 (0.06)	2.46 (0.07)	2.58 (0.06)
^{57}Co	c	271.74 d	—	6.17 (0.19)	7.68 (0.23)	8.07 (0.22)
^{58}Co	i	70.86 d	0.231 (0.009)	8.43 (0.24)	9.89 (0.27)	10.1 (0.2)
^{57}Ni	c	35.6 h	—	0.188 (0.011)	—	0.195 (0.010)
^{69m}Zn	i	13.756 h	—	1.28 (0.06)	—	1.02 (0.05)
^{66}Ga	c	9.49 h	1.54 (0.21)	8.03 (0.68)	6.56 (0.58)	7.27 (0.79)
^{69}Ge	c	39.05 h	3.00 (0.35)	11.5 (1.3)	10.2 (1.2)	9.19 (1.00)
^{72}As	i	26.0 h	8.29 (0.37)	19.1 (1.0)	15.2 (0.7)	13.4 (0.6)
^{73}As	c	80.3 d	12.5 (0.4)	29.7 (1.0)	19.3 (0.6)	22.0 (0.7)
^{74}As	i	17.77 d	2.84 (0.17)	5.27 (0.31)	5.06 (0.30)	4.78 (0.27)
^{72}Se	c	8.40 d	2.10 (0.09)	5.58 (0.27)	3.66 (0.15)	3.78 (0.15)
^{73}Se	c	7.15 h	7.49 (0.24)	12.8 (0.4)	—	8.99 (0.25)
^{75}Se	c	119.78 d	17.8 (0.5)	26.8 (0.8)	20.4 (0.6)	19.8 (0.5)
^{77}Br	c	57.04 h	20.9 (0.8)	21.6 (0.9)	18.1 (0.7)	16.1 (0.6)
^{76}Kr	c	14.8 h	3.10 (0.34)	3.30 (0.37)	2.53 (0.27)	2.20 (0.24)
^{79}Kr	c	35.04 h	28.8 (1.3)	23.0 (1.1)	19.2 (0.8)	17.2 (0.7)
^{81}Rb	c	4.572 h	46.7 (2.4)	26.8 (1.3)	25.4 (1.3)	20.2 (0.9)
^{82m}Rb	i	6.472 h	20.3 (0.9)	15.1 (0.7)	13.2 (0.6)	11.7 (0.5)

Table A.4 – continued from previous page

Product	Type	$T_{1/2}$	0.4 GeV [mb]	1.3 GeV [mb]	2.2 GeV [mb]	3.0 GeV [mb]
^{83}Rb	c	86.2 d	58.0 (4.2)	38.4 (2.8)	29.6 (2.1)	31.8 (2.3)
^{84}Rb	i	32.82 d	8.45 (0.35)	7.76 (0.32)	6.72 (0.28)	6.82 (0.26)
^{83}Sr	c	32.41 h	42.6 (3.7)	25.7 (2.3)	21.4 (1.9)	20.6 (1.8)
^{85}Sr	c	64.849 d	57.8 (2.9)	38.0 (1.9)	31.4 (1.6)	32.7 (1.6)
^{86}Y	c	14.74 h	48.1 (1.4)	30.3 (0.9)	25.4 (0.9)	24.2 (0.8)
^{87}Y	c	79.8 h	76.9 (2.3)	50.5 (1.6)	44.7 (1.3)	44.6 (1.2)
^{93}Y	c	10.18 h	2.83 (0.65)	3.26 (0.59)	3.05 (0.61)	3.24 (0.62)
^{86}Zr	c	16.5 h	11.7 (0.4)	5.00 (0.17)	4.89 (0.15)	4.21 (0.12)
^{92m}Nb	i	10.15 d	—	—	—	0.204 (0.007)

A.2 Deviation Factors

Table A.5: Deviation factor $\langle F \rangle$ calculated using Eq.(3.14) for each reaction models and JENDL/HE-2007 library. The A_{heavy} are Mn: 49, Co: 52, Ni: 52, and Zr: 85. The bold numerals designate the best code.

		A total	$A < 30$	$30 \leq A < A_{\mathrm{heavy}}$	$A \geq A_{\mathrm{heavy}}$
Mn	INCL4.6/GEM	**1.56**	1.78	1.45	**1.62**
	Bertini/GEM	1.77	1.33	1.82	2.00
	JAM/GEM	1.80	1.57	**1.34**	3.18
	INCL++/ABLA07	1.95	2.40	1.72	2.18
	JENDL/HE-2007	1.59	**1.24**	1.55	2.00
Co	INCL4.6/GEM	1.57	1.86	1.56	1.44
	Bertini/GEM	1.72	1.33	1.81	1.73
	JAM/GEM	1.74	1.67	1.53	2.05
	INCL++/ABLA07	2.04	2.30	1.72	2.36
	JENDL/HE-2007	**1.40**	**1.14**	**1.47**	**1.39**
Ni	INCL4.6/GEM	1.82	2.82	**1.50**	1.68
	Bertini/GEM	2.20	4.51	1.58	1.84
	JAM/GEM	2.11	4.30	1.54	1.75
	INCL++/ABLA07	1.96	2.39	1.69	2.04
	JENDL/HE-2007	**1.60**	**2.17**	1.55	**1.39**
Zr	INCL4.6/GEM	4.54	60.2	2.00	2.23
	Bertini/GEM	4.07	28.9	2.56	**2.05**
	JAM/GEM	6.14	101	2.94	2.23
	INCL++/ABLA07	**2.03**	**3.46**	1.80	2.06
	JENDL/HE-2007	2.25	5.46	**1.79**	2.31